Search for Supersymmetry in Multilepton Events with the ATLAS Detector

Dissertation der Fakultät für Physik

der

Ludwig-Maximilians-Universität München

vorgelegt von

Julien de Graat

geboren in München

München, 02. Mai 2012

Erstgutachterin: Prof. Dr. Dorothee Schaile
Zweitgutachter: Prof. Dr. Wolfgang Dünnweber
Datum der mündlichen Prüfung: 15. Juni 2012

Abstract

A search for Supersymmetry in events with three leptons (electrons or muons) and missing transverse momentum is presented. The observation of a significant excess of events with three leptons in the final state with respect to the prediction of the Standard Model would be a hint of New Physics. A sample with an integrated luminosity of $L = 2.06\,\mathrm{fb}^{-1}$ of proton-proton collision data at a centre-of-mass energy of $\sqrt{s} = 7\,\mathrm{TeV}$ delivered by the LHC and recorded by the ATLAS detector in 2011 is used. Special focus is placed on the composition of the Standard Model background and the measurement of misidentification rates of electrons and muons. The misidentification rates are determined from Monte Carlo simulated samples. The misidentification rates obtained for electrons yield values between $\sim 20\%$ and $\sim 6\%$, depending on the transverse momentum and the pseudorapidity of the electrons, while for muons values between $\sim 42\%$ and $\sim 10\%$, depending on the transverse momentum of the muons, are obtained. Two different selections are investigated, one selection vetoing events with the presence of Z bosons, the other selection requiring the presence of a Z boson. The observations of 32 events with an expectation of 26 ± 5 events due to processes of the Standard Model and 95 events with an expectation of 72 ± 15 events, respectively, are interpreted in a phenomenological Minimal Supersymmetric Standard Model and in simplified supersymmetric models. Limits are placed in the mass parameter space of these models.

Zusammenfassung

In der hier vorgelegten Arbeit wird die Suche nach Supersymmetrie in Ereignissen mit drei Leptonen (Elektronen oder Myonen) und fehlendem Transversalimpuls vorgestellt. Die Beobachtung eines signifikanten Überschusses an Ereignissen mit drei Leptonen im Endzustand gegenüber der Erwartung aufgrund des Standardmodells wäre ein Hinweis auf neue Physik. Untersucht wird ein Datensatz einer integrierten Luminosität $L = 2.06\,\mathrm{fb}^{-1}$, aufgenommen im Jahr 2011 mit dem ATLAS-Detektor am LHC in Proton-Proton-Kollisionen bei einer Schwerpunktsenergie $\sqrt{s} = 7\,\mathrm{TeV}$. Besonderes im Blickpunkt steht dabei die Zusammensetzung des Untergrunds aus Prozessen des Standardmodells und die Messung von Fehlidentifikationsraten von Elektronen und Myonen. Die Fehlidentifikationsraten werden aus Monte Carlo Simulationen der Untergrundprozesse des Standardmodells bestimmt. Für Elektronen erhält man so Werte zwischen $\sim 20\%$ und $\sim 6\%$, abhängig vom Transversalimpuls und der Pseudorapidität der Elektronen, und für Myonen Werte zwischen $\sim 42\%$ und $\sim 10\%$, abhängig vom Transversalimpuls der Myonen. Es werden zwei verschiedene Signalregionen untersucht. In der ersten Region ist die Produktion von Z-Bosonen unterdrückt, während in der zweiten Region das Auftreten eines Z-Bosons verlangt wird. Die Beobachtung von 32 Ereignissen bei einer Erwartung aufgrund des Standard Modells von 26 ± 5 Ereignissen bzw. 95 Ereignissen bei einer Erwartung von 72 ± 15 Ereignissen wird in einem phenomenologischen minimalen supersymmetrischen Standardmodell und in vereinfachten supersymmetrischen Modellen interpretiert. In den Massenparameterräumen dieser Theorien können Ausschlussgrenzen festgelegt werden.

Contents

1 Introduction

Understanding the world around us has always been a driving force in scientific progress for mankind, starting from the ancient times up to today. With many new steps in the direction of a more complete picture, new questions arose, only to be answered and to lead to yet new questions. One of the aspects of the world around us are the fundamental constituents of matter. While some Greek philosophers thought this to be the four elements fire, earth, water and air, we have a much deeper understanding of the building blocks of matter today.

The best description of the elementary particles and their interactions available today is the Standard Model of Particle Physics (SM). It describes the behaviour of the known elementary particles, 6 leptons and 6 quarks, and the forces, except for gravity, acting between these particles through the exchange of gauge bosons. Although the SM has been tested to great precision in the past decades, a couple of questions remain unanswered within its framework. One of these questions is how the massive gauge bosons acquire their masses, since the SM only allows massless exchange particles. The issue can be solved by introducing the Higgs mechanism. But since no Higgs particle, predicted by the mechanism, has been observed yet, this theory has not been confirmed. Moreover, the mass of the Higgs boson depends on contributions from all particles coupling to it with contributions of sizeable amounts. In order for these contributions to cancel out within the SM a high level of fine tuning of the theory is necessary.

This fine tuning problem and a couple of other open questions in the SM can be solved by introducing a new theory that expands the SM, Supersymmetry (SUSY). SUSY is a new symmetry between bosons and fermions capable of answering many of the open questions of the SM and also questions beyond, like the composition of the Dark Matter. The theory predicts many new elementary particles, at least some of which should be detectable at the Large Hadron Collider (LHC) for SUSY to actually solve the fine tuning problem.

A search for SUSY in events with three charged leptons (electrons or muons) and missing transverse momentum in proton-proton collision data delivered by the LHC and taken with the ATLAS detector is presented. Several selection criteria are applied to the data events in order to separate the potential signal from events that are due to processes of the SM. This search channel presents the advantage of having only few SM processes contributing to the background.

This thesis is divided into six chapters. Chapter 2 gives a short overview over the theoretical background of the search and the results of previous searches for SUSY. Some of the problems of the SM are discussed as well as solutions provided by SUSY. The production mechanisms of SUSY particles and their decays are also discussed. In Chapter 3 a brief description of the experimental setup is given, i.e. the LHC accelerator and the ATLAS experiment are introduced. Chapter 4 summarises the general aspects of the analysis, from the data and Monte Carlo simulated samples that are used to the definition of the signal regions. In Chapter 5 details of the composition of the SM background are investigated and the strategy for the prediction of the SM background is presented. Finally, Chapter 6 shows the final results of the analysis as well as an interpretation of the results in the context of two different SUSY models.

2 Theoretical Background

2.1 Standard Model

2.1.1 Fundamental Theory

The Standard Model of Particle Physics (SM) is a well established theory. The short overview given here is based on [1, 2, 3].

The elementary particles and their interactions are described in the framework of a gauge theory based on the gauge group $SU(3)_C \times SU(2)_L \times U(1)_Y$. All matter consists of fermionic particles whose interactions are mediated through bosonic particles. The interactions described within the SM are the strong, the weak and the electromagnetic interactions with the latter two unified in the electroweak theory. The fourth fundamental force, gravity, is not part of the SM.

The force carrier particles are spin 1[1] gauge bosons. There are 8 massless, electrically neutral, coloured gluons (they are the only coloured gauge bosons) as mediators of the strong interaction coupling to coloured particles. The three colours red, green and blue represent the different charges of the strong interaction. The weak interaction is transmitted by three massive bosons, the electrically neutral Z^0 and the two oppositely charged W^+ and W^-. These bosons couple to the weak isospin of particles. Finally, the gauge boson of the electromagnetic interaction is the electrically neutral photon (γ) which couples to the electric charge of particles.

The spin 1/2 fermions are divided into 6 quarks and 6 leptons. Both the quarks and the leptons are grouped into 3 generations. The first generation contains the up and down quark for the quarks and the electron and the electrically neutral electron-neutrino for the leptons. The three generations of quarks and leptons are listed in Table 2.1. While the quarks are subject to all three fundamental forces described in the SM, the leptons, not carrying colour, only interact within the electroweak theory.

Each fermion in the SM also has an anti-particle associated to it. The anti-particles differ from their respective particles in that they have among others opposite electric and colour charge. Notably, the mass and the spin of a particle and its anti-particle are the same.

---

[1] 1 $\hbar$. Natural units are being used throughout this thesis, i.e. $\hbar = 1$ and $c = 1$.

Table 2.1: *The fermions of the SM [4].*

Quarks

Generation	Name	Symbol	Charge [e]	Mass [MeV]
1	up	u	$+\frac{2}{3}$	1.5 to 3.3
	down	d	$-\frac{1}{3}$	3.5 to 6.0
2	charm	c	$+\frac{2}{3}$	104^{+26}_{-34}
	strange	s	$-\frac{1}{3}$	$1.27^{+0.07}_{-0.11} \times 10^3$
3	top	t	$+\frac{2}{3}$	$171.2 \pm 2.1 \times 10^3$
	bottom	b	$-\frac{1}{3}$	$4.20^{+0.17}_{-0.07} \times 10^3$

Leptons

Generation	Name	Symbol	Charge [e]	Mass [MeV]
1	electron	e	-1	0.511
	electron-neutrino	ν_e	0	$< 2.2 \times 10^{-6}$
2	muon	μ	-1	105.7
	muon-neutrino	ν_μ	0	$< 170 \times 10^{-3}$
3	tau	τ	-1	1777.7
	tau-neutrino	ν_τ	0	< 15.5

The theory of the strong interaction is called Quantum Chromodynamics (QCD) and is described by the $SU(3)_C$ gauge group. It describes the interaction of the particles carrying colour charge, i.e. the quarks and the gluons. Since the force carrier particles of the interaction, the gluons, are colour-charged, they can interact with themselves. This leads to two very important phenomena of QCD: *asymptotic freedom* and *confinement*. The coupling constant α_s of the strong interaction is in fact not a constant but depends on the square of the momentum transfer (Q^2). Moving to very high momentum transfers and thus small distances, the coupling decreases and vanishes asymptotically. In the limit $Q^2 \to \infty$ quarks can be regarded as free particles, since the coupling to other coloured objects vanishes. This is called *asymptotic freedom*. On the other hand, moving to large distances, the value of the coupling constant α_s increases strongly and makes it impossible to completely separate bound coloured objects. This is called *confinement*, since the quarks (and gluons) are confined in bound states (like the proton or the neutron). Confinement is responsible for hadronisation, which in turn determines how quarks and gluons produced in particle accelerators are observed in experiments. Quarks as well as gluons are not observed as single free particles, but instead several hadrons close to each other are observed in a particle jet (usually just called 'jet').

The unified theory of the weak and the electromagnetic interaction, the electroweak theory, combines the two interactions into one theory. It describes the various couplings of the gauge bosons of the weak interaction and the photon in the gauge group $SU(2)_L \times U(1)_Y$.

The electroweak theory has been tested to very great precision in several experiments in the past decades and has been found to very accurately describe the experimental findings. But the theory in itself contains only massless gauge bosons (massive gauge bosons would break the gauge principle), whereas the Z^0 and W bosons are known to be massive. This contradiction can be solved by the Higgs mechanism. Through the principle of spontaneous symmetry breaking the gauge bosons obtain a mass while preserving the gauge principle of the electroweak theory. The Higgs mechanism also predicts a new scalar particle, the Higgs boson, which has not been discovered yet. It also offers a way to generate the masses of the quarks and leptons through a Yukawa coupling to the Higgs boson.

2.1.2 Remaining Challenges of the SM

Despite the huge success of the SM in describing the fundamental interactions between particles, a number of questions remain unanswered. The goal of any new theory of elementary particles or any extension of the existing theory should be to answer at least a part of these questions. This section gives a short overview of some of the inconsistencies within the SM.

The Higgs mechanism, providing the electroweak symmetry breaking, has not been confirmed yet. Searches for the Higgs boson performed in accelerator experiments have only been able to constrain the mass of a potential Higgs boson but have not shown significant evidence for the existence of the particle [5, 6].

Furthermore many parameters of the SM are free parameters without any theoretical prediction. Examples of these would be the mass of the Higgs boson as well as the masses of the quarks and leptons, but also the coupling strengths of the electromagnetic, weak and strong forces. These couplings depend on the energy. For the strong and the weak interaction the coupling constants become smaller with increasing energy whereas the electromagnetic coupling becomes larger. Grand Unified Theories (GUTs) describe the three fundamental forces of the SM in one theory. At an energy scale of $M_{\mathrm{GUT}} \sim 10^{16}\,\mathrm{GeV}$ the couplings reach the same strength. This is not exact within the SM as is shown in Figure 2.1. Also, the reason for the very large difference between the GUT scale and the energy scale of the electroweak unification ($M_{\mathrm{W}} \sim 10^{2}\,\mathrm{GeV}$) is unknown and referred to as the hierarchy problem.

The hierarchy problem also affects the Higgs mechanism. Electroweak precision measurements predict a Higgs mass of $m_{\mathrm{H}} = O(100\,\mathrm{GeV})$. But this value gets contributions through loop corrections from all particles coupling to the Higgs boson. These corrections are in the order of magnitude of the validity of the electroweak theory. For these

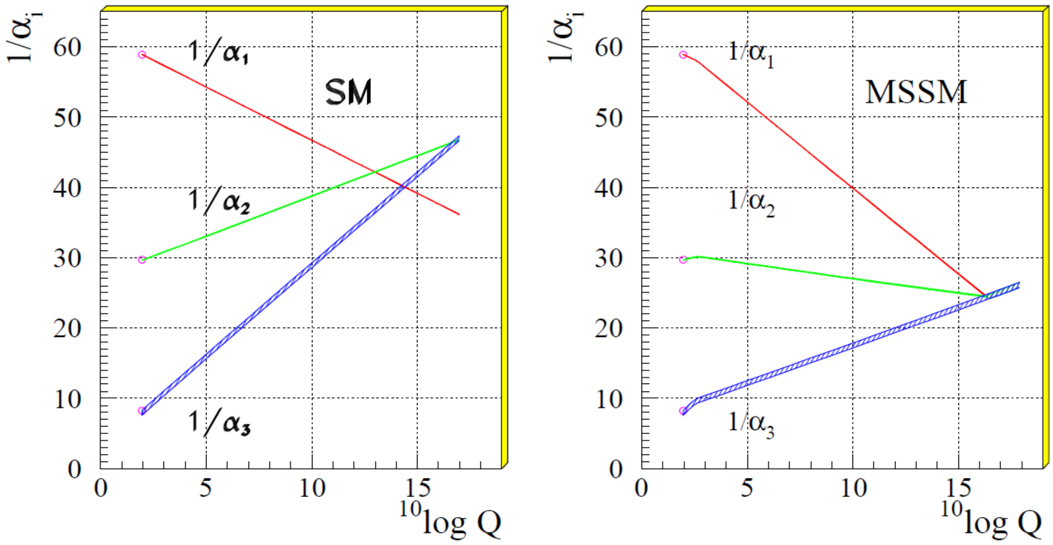

Figure 2.1: *Evolution of the inverse of the coupling constants in the SM (left) and the MSSM (right) [8].*

contributions to cancel out a high level of fine tuning is necessary ('fine tuning problem'). Another phenomenon that cannot be explained in the framework of the SM is the observation of a sizeable amount of cold dark matter in the universe [7]. None of the SM particles has properties that could explain the observed dark matter.

2.2 Supersymmetry

Supersymmetry (SUSY) is a promising theory for an extension of the SM. The successful parts of the SM are easily incorporated into the theory while many of the yet not understood components find an explanation. This description of SUSY is based on [9, 10].
SUSY is a symmetry between bosons and fermions. Each particle in the SM is predicted to possess a supersymmetric partner ('superpartner') with a spin different by 1/2 from that of the SM particle. The superpartners of the fermions are called 'sfermions' and have spin 0, while the superpartners of the (gauge) bosons are called 'gauginos' and have spin 1/2. The superpartners of the Higgs particles (there are more than one Higgs particle in SUSY) are called 'higgsinos' and also have spin 1/2. This naming convention is also applied to the individual particles. The partner of the electron is called 'selectron', the partner of the Z boson is called 'zino', etc.
The SM particles and their superpartners ('sparticles') should not differ in any other way than in their spin. Especially the masses of the sparticles would be identical to that of their

SM counterparts and at least some (e.g. the massless photino or the very light selectron) should have been detected in experiments by now, which is not the case. This implies that SUSY, if it actually exists, is a broken symmetry.

In a supersymmetric extension of the SM the fine tuning problem of the Higgs mechanism is solved. The sparticles also contribute to the Higgs mass through loop corrections, but with the opposite sign compared to their respective SM partners. Therefore the contributions cancel out and solve the fine tuning problem.

As shown in Figure 2.1, SUSY enables the unification of the gauge couplings at an energy scale of 10^{16} GeV. This cannot be achieved within the SM alone.

2.2.1 The MSSM

The Minimal Supersymmetric Standard Model (MSSM) is the simplest supersymmetric extension of the SM. It is minimal with respect to the number of new elementary particles added to those of the SM. Each SM particle is assigned one superpartner, while the Higgs sector contains two chiral supermultiplets, giving masses to the up-type quarks, and the down-type quarks and charged leptons, respectively.

In order to eliminate lepton number and baryon number violating processes, which are in principle allowed within the MSSM and often lead to a decay of the proton with a very short lifetime, a new symmetry, R-parity, is introduced[2]. It is formulated as a multiplicative quantum number and takes the form:

$$R = (-1)^{3(B-L)+2S}, \tag{2.1}$$

where B is the baryon number, L is the lepton number and S is the spin of a particle. One can easily convince oneself that $R = +1$ for all SM particles and $R = -1$ for all sparticles. R-parity conservation implies that sparticles can only be produced in pairs and that they decay into a SM particle and another (lighter) sparticle (or, more generally, any number of SM particles and an odd number of sparticles). This in turn means that the lightest sparticle (LSP) is stable, highlighting another feature of SUSY, which is to provide an explanation for the cold dark matter in the universe as a relic density of stable LSPs.

Table 2.2 lists the mass eigenstates of the particles of the MSSM. The superpartners of the charged and the neutral bosons each mix to form the mass eigenstates called charginos and neutralinos, respectively. The squarks and sleptons, having a spin of 0, are not left or right-handed themselves, but are the superpartners of either left or right-handed SM particles. The Higgs sector comprises two complex doublets with a total of 5 observable particles, while the other degrees of freedom are absorbed in the Higgs mechanism to give the weak gauge bosons their masses.

---

[2] Some SUSY models avoid the proton decay while allowing R-parity violation. These models are not discussed here.

Table 2.2: *The mass eigenstates of the MSSM.*

Particle	Notation	Spin	Sparticle	Notation	Spin
left-handed quark	q_L	$\frac{1}{2}$	‘left-handed’ squark	$\tilde{q}_L$	0
right-handed quark	q_R	$\frac{1}{2}$	‘right-handed’ squark	$\tilde{q}_R$	0
left-handed lepton	l_L	$\frac{1}{2}$	‘left-handed’ slepton	$\tilde{l}_L$	0
right-handed lepton	l_R	$\frac{1}{2}$	‘right-handed’ slepton	$\tilde{l}_R$	0
gluon	g	1	gluino	$\tilde{g}$	$\frac{1}{2}$
W bosons charged Higgs	$W^{\pm}$ $H^{\pm}$	1 0	charginos	$\tilde{\chi}^{\pm}_{1,2}$	$\frac{1}{2}$
Z boson photon neutral Higgs	Z^0 γ H^0, h^0, A^0	1 1 0	neutralinos	$\tilde{\chi}^0_{1,2,3,4}$	$\frac{1}{2}$

As mentioned before, SUSY has to be a broken symmetry. In order to preserve the advantages of the theory while explaining the splitting of the masses of the SM particles and the SUSY particles, a symmetry breaking term is added to the supersymmetric Lagrangian. This is called ‘soft’ SUSY breaking:

$$\mathcal{L} = \mathcal{L}_{SUSY} + \mathcal{L}_{soft}, \tag{2.2}$$

where $\mathcal{L}_{SUSY}$ is the SUSY conserving part of the Lagrangian that describes the particles and couplings of the SM, while $\mathcal{L}_{soft}$ is the SUSY breaking part. $\mathcal{L}_{SUSY}$ contains the three gauge couplings, one Higgs mass parameter and Yukawa couplings of the quarks and leptons and their SUSY partners to the Higgs bosons and the higgsinos. $\mathcal{L}_{soft}$ contains the masses of the gauginos, trilinear scalar couplings, mass terms for the squarks and sleptons and additional Higgs mass parameters.

This soft SUSY breaking introduces 105 new free parameters to the theory. This high number of free parameters makes it difficult to develop viable SUSY models that can be tested in experiments. The parameters themselves are already constrained by observations like the actual mass of the Z boson, the amount of CP-violation or the magnitude of flavour changing neutral currents. In order to make phenomenological analyses possible, a number of phenomenologically reasonable assumptions can be made to reduce the number of free parameters of the MSSM. One such phenomenological model is presented in Section 2.2.4.

2.2.2 Production of SUSY Particles

The most important production mode for sparticles at the LHC is via the strong interaction. Several Feynman diagrams in Figure 2.2 illustrate possible production processes of squarks and gluinos. The direct production of weakly interacting sparticles, i.e. charginos, neutralinos and sleptons, is suppressed compared to the production of strongly coupling sparticles, unless these sparticles are too heavy to be produced. Some examples of this direct production via quark-antiquark interactions are given in Figure 2.3. Figure 2.4 shows the production cross sections at next-to-leading order for various sparticle pairs at the LHC.

The direct production of weakly interacting particles can become dominant when the mass spectrum of the considered model has squarks and gluinos that are too heavy to be produced at the available energies (currently at most 7 TeV at the LHC, see Chapter 3).

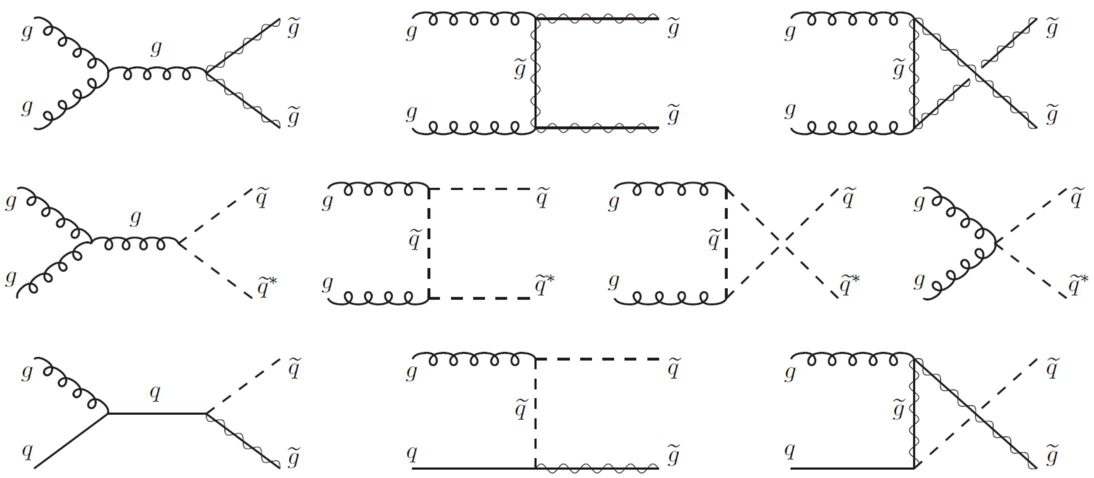

__Figure 2.2:__ Gluino and squark production through gluon-gluon and quark-gluon interaction [9].

2.2.3 Decay of SUSY Particles and Experimental Signatures

For the discovery of SUSY in particle accelerators, it is crucial to understand the possible decay modes of sparticles. This section (and the entire thesis) assumes that the LSP is the lightest neutralino as well as R-parity conservation.

In general, sparticles decay to a lighter sparticle and a SM particle. If there is no kinematically allowed decay (e.g. all squarks are heavier than the gluinos) an appropriate three-body decay occurs. These will not be mentioned for all sparticles in this section.

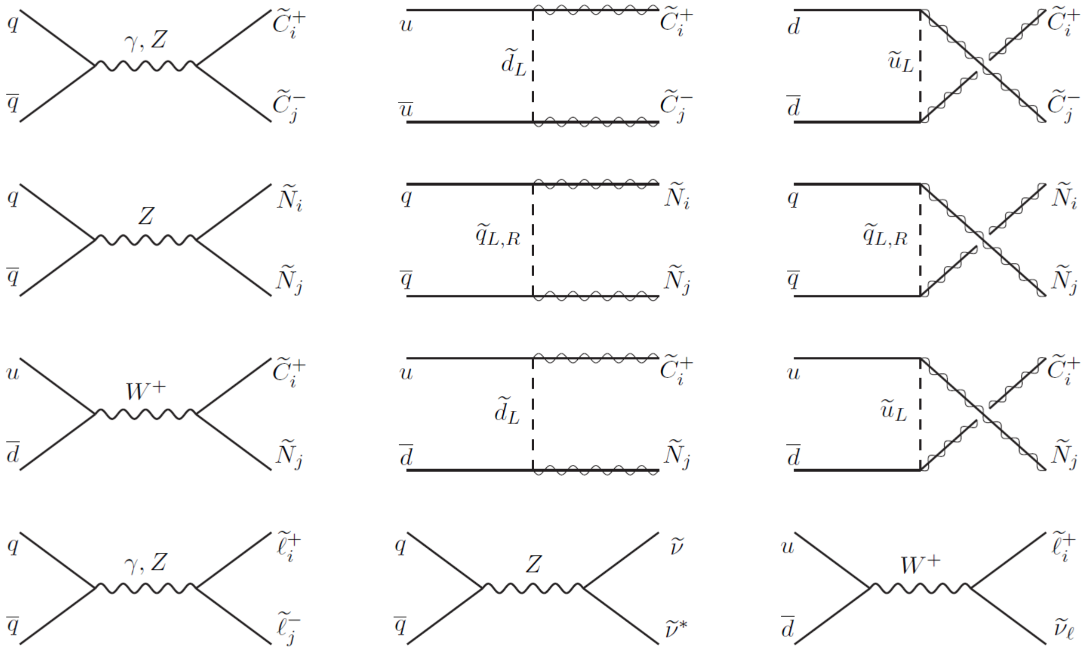

Figure 2.3: *Gaugino and slepton production through quark-antiquark interaction [9].*

Gluinos. The main decay of gluinos is to a quark and a squark. The quark hadronises and forms a jet that can be seen in the detector. The squark decays further.

Squarks. The dominant decay of squarks is into a quark (forming a jet) and a gluino through the strong interaction. Another possible decay for squarks is into a quark and a chargino or a neutralino through the electroweak interaction.

Charginos and Neutralinos. Since charginos and neutralinos are superpositions of the superpartners of the electroweak gauge bosons and the Higgs bosons, they share the couplings of these. Possible two-body decays include decays into squark-quark pairs, slepton-lepton pairs and electroweak gauge bosons and a lighter chargino or neutralino:

- $\tilde{\chi}_i^0 \to Z^0 + \tilde{\chi}_j^0$
- $\tilde{\chi}_i^0 \to W^\pm + \tilde{\chi}_j^\mp$
- $\tilde{\chi}_i^0 \to l + \tilde{l}$
- $\tilde{\chi}_i^0 \to \nu + \tilde{\nu}$
- $\tilde{\chi}_i^\pm \to Z^0 + \tilde{\chi}_j^\pm$
- $\tilde{\chi}_i^\pm \to W^\pm + \tilde{\chi}_j^0$
- $\tilde{\chi}_i^\pm \to l + \tilde{\nu}$
- $\tilde{\chi}_i^\pm \to \nu + \tilde{l}$

The electroweak gauge bosons decay as usual according to their SM couplings, yielding either jets or leptons as signatures in the detector. The directly produced leptons in the decays can be detected as such, while the eventually produced LSP, a neutralino, es-

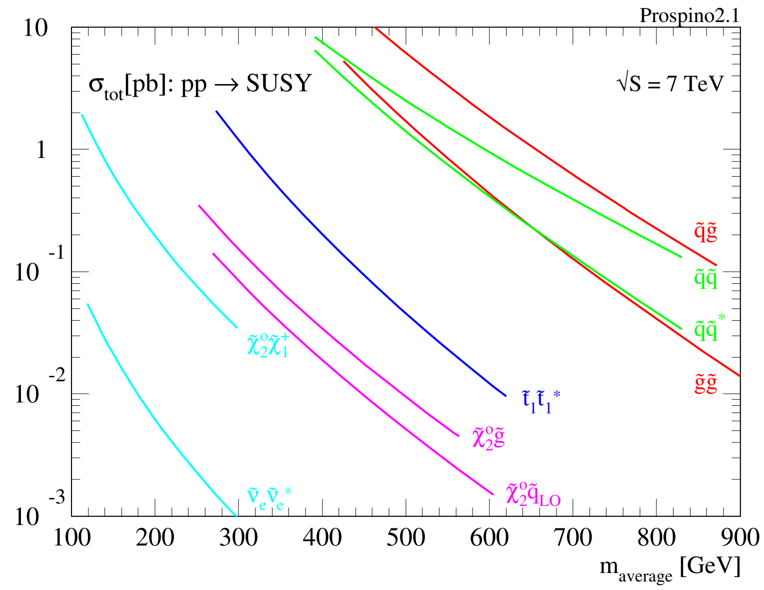

Figure 2.4: *Next-to-leading order production cross sections of sparticles at the LHC [11].*

capes the detector undetected. The only way it is visible in a collision is through the momentum balance, that seems to not be preserved.

Sleptons. Sleptons can decay into a lepton and a chargino or a neutralino. Under the assumption that the LSP is the lightest neutralino, the decay of sleptons into a lepton and the LSP is kinematically allowed.

In summary, most sparticles have several different decay modes. The decay of a sparticle always yields a new sparticle, which then decays further until an LSP is produced. In these decays a long cascade of sparticles can be produced, yielding an experimental signature with possibly several jets, possibly several leptons and missing momentum. The study presented here aims at signatures with three charged leptons and some amount of missing (transverse) momentum.

2.2.4 Phenomenological MSSM

The phenomenological MSSM (pMSSM [12]) is an MSSM where several assumptions are made in order to reduce the huge number of free parameters. These assumptions are:

- SUSY does not introduce a new source of CP-violation;
- No flavour changing neutral currents are introduced at tree level;
- Universality of the first and second generation of sfermions at low energy.

This set of assumptions allows the number of free parameters to be greatly reduced. The masses of the charginos and the neutralinos depend on the gaugino mass parameters M_1 and M_2, the Higgs mass parameter $|\mu|$ and on the ratio of the vacuum expectation values of the two Higgs doublets, $\tan\beta$.
The value $\tan\beta = 6$ is chosen for the interpretation of the results of the present analysis. This choice does not greatly affect the phenomenology discussed in this thesis. The gluinos, squarks and left-handed sleptons are all chosen to be heavy in comparison to the other sparticles in order to avoid their production. The masses of the right-handed sleptons are all assumed be $m_{\tilde{l}_R} = (m_{\tilde{\chi}_2^0} + m_{\tilde{\chi}_1^0})/2$.
With this set of parameters and assumptions, the sparticles that can be produced are gauginos and right-handed sleptons with favoured decay modes according to the electroweak decays outlined in the last section. This ensures a rather high number of leptons in the final state, e.g. three leptons as investigated in this analysis.

2.2.5 Simplified Models

A different approach to phenomenologically accessible SUSY models than the pMSSM are the simplified models. They are made in a way that they contain the minimal particle content necessary to produce SUSY-like events with the final states of interest. The only free parameters are the masses of the relevant sparticles. All sparticles that are not relevant to the final state or the production mechanism of interest are set to an inaccessibly high mass, i.e. several TeV.
For this analysis a model producing multilepton final states is investigated, with wino-like $\tilde{\chi}_1^\pm$ and $\tilde{\chi}_2^0$, bino-like $\tilde{\chi}_1^0$, sneutrinos and sleptons. The mass degenerate $\tilde{\chi}_1^\pm$ and $\tilde{\chi}_2^0$ decay into left-handed sleptons and sneutrinos with a branching fraction of 50% to each, since the masses are set equal: $m_{\tilde{\nu}} = m_{\tilde{l}_L} = (m_{\tilde{\chi}_1^0} + m_{\tilde{\chi}_1^\pm})/2$. The sleptons and sneutrinos then decay further into the lightest neutralino, which is the LSP. This gives rise to final states with several leptons and missing (transverse) momentum.

2.2.6 Constraints on Supersymmetry

Many searches for SUSY have been conducted at previous and present accelerator experiments. These searches have not led to a discovery of SUSY or any of the new particles predicted by the theory. Instead, limits on the cross sections for the production of sparticles and their masses are set in various models.
One SUSY model that is very popular for the setting of limits is the minimal supergravity model (mSUGRA). Through a number of assumptions, including assumptions on the SUSY breaking mechanism, the number of free parameters is reduced from 105 to 5:

- m_0, the scalar mass parameter determining the sfermion masses and the mass squared parameters of the Higgs;
- $m_{\frac{1}{2}}$, the gaugino mass parameter determining the gaugino masses;
- A_0, the trilinear coupling parameter;
- $\tan\beta$, the ratio of the vacuum expectation values of the two Higgs doublets;
- sgnμ, the sign of the Higgs mass parameter μ.

Figure 2.5(a) shows limits in the mSUGRA parameter space set by the experiments at the Tevatron [13] and at LEP [14]. At LEP, an upper bound on the mass of the lighter chargino was set to $m_{\tilde{\chi}_1^\pm} > 103.5\,\mathrm{GeV}$ [14]. Figure 2.5(b) shows a limit set by an ATLAS analysis searching for SUSY in final states with jets and missing transverse momentum [15], that greatly expands the limits previously set. The figure also nicely illustrates the dependence of the gluino and squark masses on the parameters $m_{\frac{1}{2}}$ and m_0, respectively. The limits set by a previous ATLAS analysis in the simplified model scenario also considered in this analysis is shown in Figure 2.6 [16]. Chargino masses up to 200 GeV are excluded for large mass differences to the LSP.

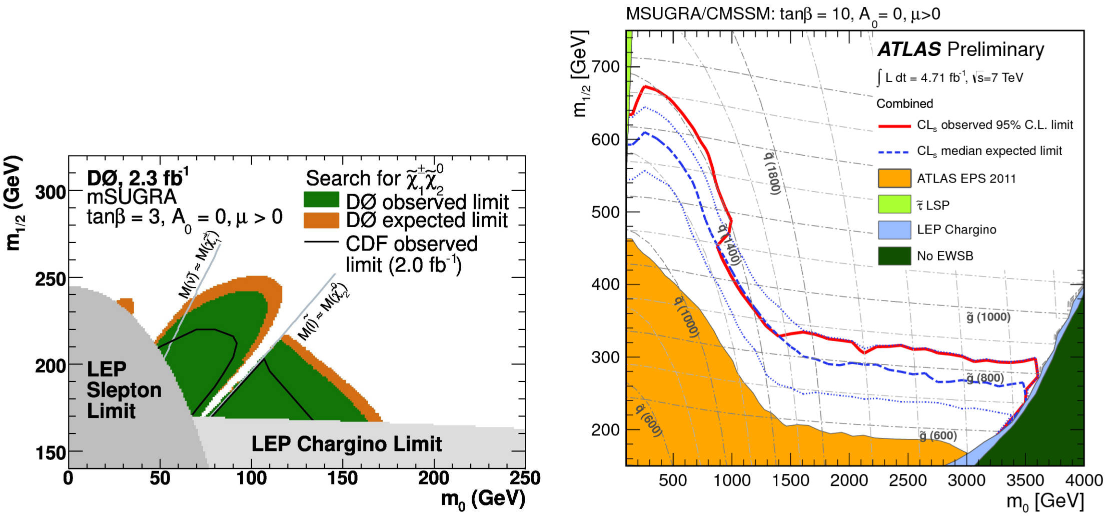

(a) Limits in the mSUGRA plane by the D0 collaboration [13].

(b) ATLAS limit in the mSUGRA plane [15].

Figure 2.5: *Limits in the mSUGRA scenario by LEP and Tevatron experiments (a) and ATLAS (b).*

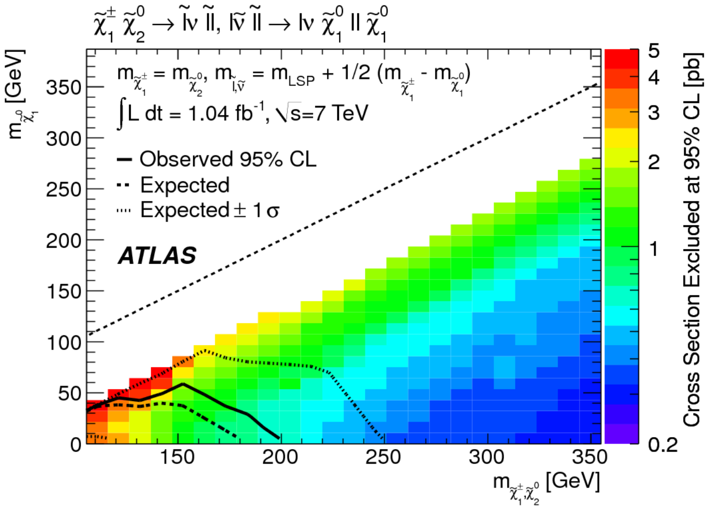

Figure 2.6: *Limit set by an ATLAS analysis in a simplified model scenario [16].*

3 LHC and ATLAS

3.1 The Large Hadron Collider

The Large Hadron Collider (LHC) [17] is a proton-proton collider located at CERN[1] near Geneva in Switzerland (Figure 3.1). It has been in operation since March 2010, colliding protons at a centre-of-mass energy of $\sqrt{s} = 7\,\text{TeV}$. The LHC is installed in the same tunnel with a circumference of about 27 km as the former particle accelerator LEP (Large Electron Positron Collider) which was in operation from 1989 to 2000. At LEP, electrons and positrons were collided at a centre-of-mass energy of up to $\sqrt{s} \approx 209\,\text{GeV}$, limited by synchrotron radiation. However, synchrotron radiation is not a limitation for the acceleration of protons at the LHC because of the relatively high proton mass ($m_p \approx 2000\,m_e$). The design centre-of-mass energy of the LHC is $\sqrt{s} = 14\,\text{TeV}$ with a design instantaneous luminosity of $L = 1 \cdot 10^{34}\,\text{cm}^{-2}\text{s}^{-1}$. In October 2011 the peak instantaneous luminosity reached by the LHC was $L \approx 3.6 \cdot 10^{33}\text{cm}^{-2}\text{s}^{-1}$. Figure 4.1 shows the development of the luminosity in 2011.

In order to reach the final energy of 3.5 TeV per beam in 2011 (4 TeV per beam in 2012) the protons are pre-accelerated before being injected into the oppositely circulating vacuum pipes of the LHC. The superconducting beam bending magnets operating with a magnetic field of $B > 8\,\text{T}$ (for a beam energy of 7 TeV) are cooled with superfluid helium to a temperature below 2 K. The protons are collected in bunches of 10^{11} particles with a spacing of currently 50 ns between the bunches (the design bunch spacing is 25 ns). It has to be noted that this spacing is not continuous around the ring. Instead, the bunches are organised in ‘bunch trains’ of several bunches with a bunch separation of 50 ns. Two bunch trains are then separated by at least one empty bunch. Due to this structure of the bunches each crossing of two bunches with specific locations within the bunch train structure can be assigned a fixed bunch crossing ID (BCID).

An upgrade of the LHC is planned in a long shutdown in 2013. Then, from 2014 on, the LHC is planned to operate at the design characteristics.

One of the main goals of the LHC is the discovery of the Higgs boson and of new physics

---

[1] **C**onseil **E**uropéen pour la **R**echerche **N**ucléaire, which was the original name. Today, the acronym is still in use, although the name was changed to European Organization for Nuclear Research.

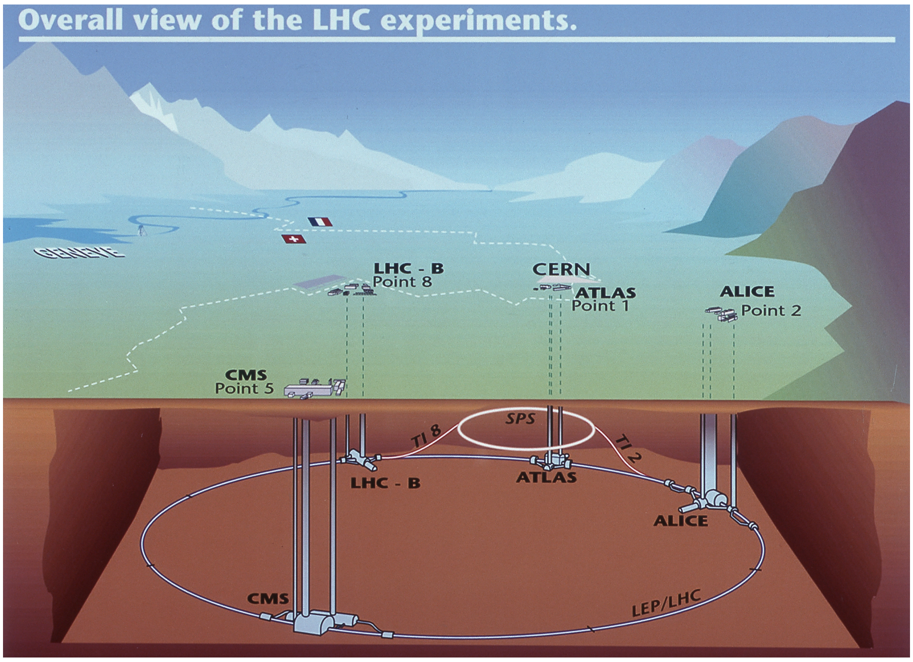

Figure 3.1: *The LHC at CERN [18]. The locations of the four large experiments as well as the pre-accelerator ring SPS (Super Proton Synchrotron) are shown.*

beyond the SM. These and other searches are performed at 4 particle detectors, ATLAS (A Toroidal LHC ApparatuS), CMS (Compact Muon Solenoid), ALICE (A Large Ion Collider Experiment) and LHCb. ATLAS and CMS are large multi-purpose detectors, the ALICE experiment is designed to study the quark gluon plasma in collisions of lead ions (which are performed in addition to the proton-proton collisions) and the LHCb experiment focuses on the physics of B-mesons.

3.2 The ATLAS Experiment

The ATLAS detector [19, 20] (Figure 3.2) with its length of 44 m, diameter of 25 m and a weight of around 7000 t is the largest particle detector at the LHC. The concentric arrangement of its cylindrical subdetectors around the beam axis of the LHC and the perpendicular orientation of the subdetectors in the endcap region allow particle detection in a wide range of space. The three main detector groups in ATLAS, from the innermost to the outermost, are:

- Inner Detector: Measurement of the charge and the momentum of charged particles;

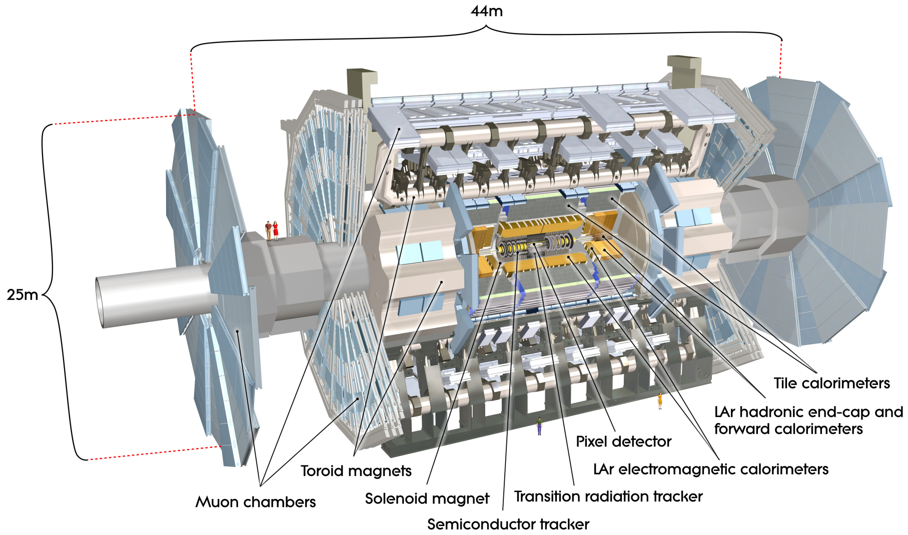

Figure 3.2: *Schematic illustration of the ATLAS detector [18].*

- Calorimeters: Subdivided into an electromagnetic calorimeter and a hadronic calorimeter, this subdetector identifies electrons, photons and hadrons and measures their energy;
- Muon Spectrometer: Measurement of muon charge and momentum.

3.2.1 Coordinate System

The ATLAS experiment uses a right handed coordinate system as shown in Figure 3.3. The origin of the coordinate system is chosen to be at the centre of the detector, i.e. at the interaction point. The z-axis points along the LHC accelerator ring, the x-axis towards the middle of the ring and the y-axis upwards. The azimuthal angle ϕ is defined in the plane perpendicular to the beam axis with $\phi = 0$ corresponding to the positive x-axis. The polar angle θ is defined with respect to the z-axis ($\tan\theta = \frac{r}{z}$ with $r = \sqrt{x^2+y^2}$). Instead of the polar angel θ the pseudorapidity η is more commonly used. It is defined as

$$\eta = -\ln(\tan\frac{\theta}{2}) \tag{3.1}$$

and has the advantage that the difference of two pseudorapidities is invariant under Lorentz boosts along the z-direction.

Two further important values are the transverse momentum p_{T} and the distance in the η-ϕ-plane ΔR. The transverse momentum of a particle is the projection of the momentum

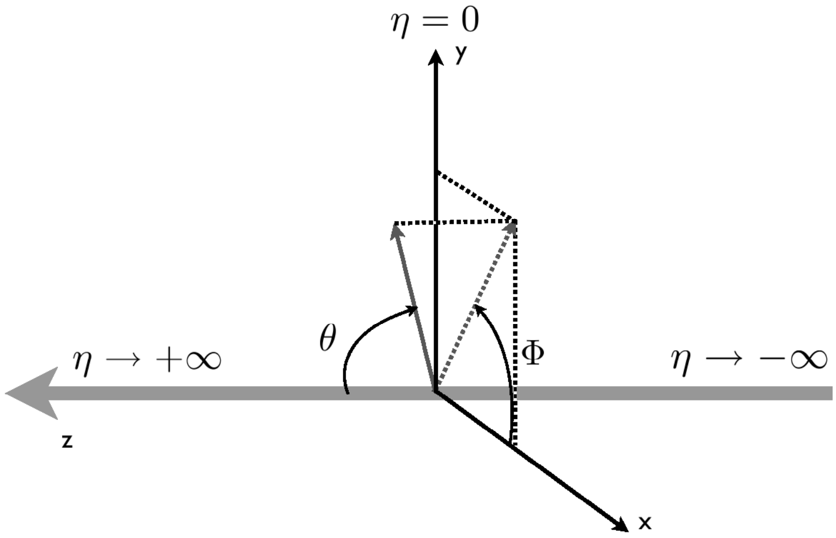

Figure 3.3: *The ATLAS coordinate system [21].*

of the particle onto the plane perpendicular to the beam axis. The distance ΔR between two particles in the η-ϕ-plane is defined as

$$\Delta R = \sqrt{\Delta\eta^2 + \Delta\phi^2} \tag{3.2}$$

3.2.2 Magnet System

Magnetic fields inside the tracking detectors of ATLAS are important for the charge and momentum measurement of charged particles. The trajectories of these particles are bent in the magnetic fields.
The ATLAS magnet system is composed of a central solenoid and a toroid.

- The superconducting **central solenoid** has a length of 5.3 m and a radius of 1.2 m. Surrounding the Inner Detector (Section 3.2.3), it deflects charged particles in the plane perpendicular to the beam axis. The field strength varies between 2 T at the interation point and 0.5 T at the outermost part of the Inner Detector.
- The **toroid magnets** provide the magnetic field for the Muon Spectrometer (Section 3.2.5). With its eight superconducting toroidal air coils in the barrel region and two additional toroids with eight coils each in the two end-cap-regions the toroid magnet system generates a magnetic field with an average field strength of 0.6 T.

3.2.3 Inner Detector

The Inner Detector (Figure 3.4) has a length of 6.2 m and a diameter of 2.1 m and is located closest to the interaction point. In the magnetic field provided by the central solenoid (Section 3.2.2) charged particles are deflected and particle momenta are measured with great precision. The Inner Detector consists of three subdetectors:

- The **pixel detector** is made of 1744 identical pixel sensors. A pixel sensor has 46080 pixels with a nominal pixel size of $50 \times 400\,\mu\text{m}^2$. In the barrel part of the pixel detector the pixel sensors are arranged in three cylindrical layers whereas there are three disks of pixel sensors in the endcap regions. The pixel detector has a resolution of $10\,\mu$m in the Rϕ-plane and $115\,\mu$m in the z-direction [20] and allows the measurement of three points along the track of a particle. Being the subdetector closest to the interaction point it is crucial in the measurement of short lived particles.
- The **semiconductor tracker** (SCT) has eight layers of silicon strip detectors providing up to eight additional points along the track of a particle with a resolution of $16\,\mu$m in the Rϕ-plane and $580\,\mu$m in the z-direction [20]. It contributes to the measurement of particle momenta, impact parameters and vertex positions, covering the pseudorapidity range of $|\eta| < 2.5$.
- The **transition radiation tracker** (TRT) is the outermost subdetector of the Inner Detector. It consists of straw tubes filled with a xenon-based gas mixture and measures on average 36 additional points along a particle track with a resolution of 0.170 mm for tracks with $p_T > 0.5\,\text{GeV}$ [20]. Electrons are separated from pions through the detection of transition radiation.

3.2.4 Calorimeter

The ATLAS calorimeter (Figure 3.5) is made up of two different systems which both measure the energy of particles through absorption. Both parts are sampling detectors with full ϕ-symmetry around the beam axis.

- The **Electromagnetic Calorimeter** (ECAL), located closer to the beam axis, consists of lead-liquid argon detectors with accordion shape absorbers and electrodes and covers the pseudorapidity range $|\eta| < 1.475$ for the barrel region and $1.375 < |\eta| < 3.2$ for the endcap region. The transition region $1.37 < |\eta| < 1.52$ between

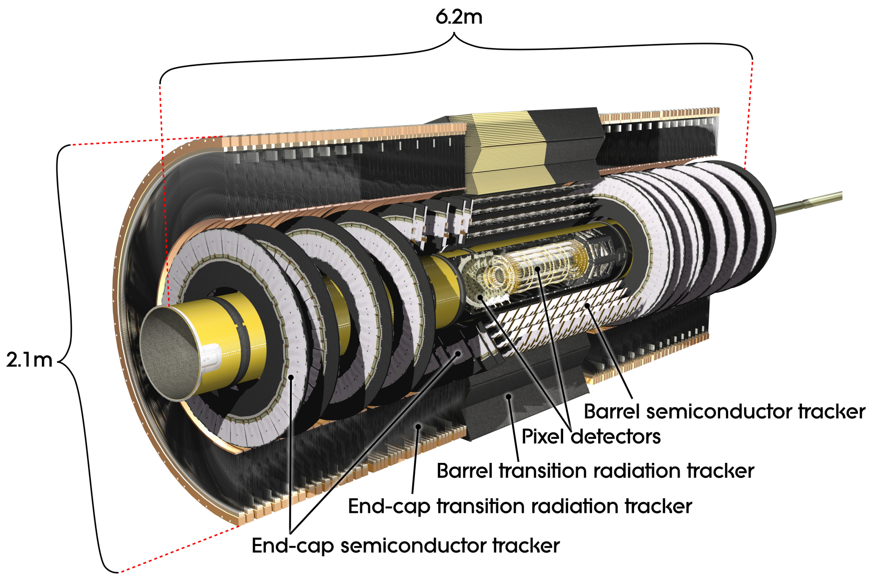

Figure 3.4: *Schematic illustration of the ATLAS Inner Detector [18].*

the barrel and the endcap is referred to as the ‘crack region’. The ECAL has several active layers and measures the energy of electromagnetically interacting particles, mainly electrons and photons. While jets and muons may also deposit energy in this part of the detector they will typically reach the next layer of the detector. After a particle interaction in the lead plates the resulting particle shower is detected in the gaps filled with liquid argon (LAr). The energy resolution of the electromagnetic showers is $\Delta E/E = 10\%/\sqrt{E/\mathrm{GeV}}$ [20].

- The **Hadronic Calorimeter** (HCAL) mainly measures the energy of hadrons. In the region $|\eta| < 1.7$ steel is used as the absorber and scintillator as the active medium, in the region $1.5 < |\eta| < 3.2$ (hadronic end-cap calorimeter, HEC) copper and liquid argon are used, while in the region $3.1 < |\eta| < 4.9$ (forward calorimeter, FCAL) tungsten and again liquid argon were chosen as material. The energy resolution of the HCAL is $\Delta E/E = 50\%/\sqrt{E/\mathrm{GeV}}$ [20].

3.2.5 Muon Spectrometer

The outermost component of the ATLAS detector is the Muon Spectrometer (MS), depicted in Figure 3.6. Since muons are (except for neutrinos which do not interact with the detector) the only particles passing the Inner Detector and the calorimeters without decaying or being absorbed, they can be measured in the outer part of the detector.

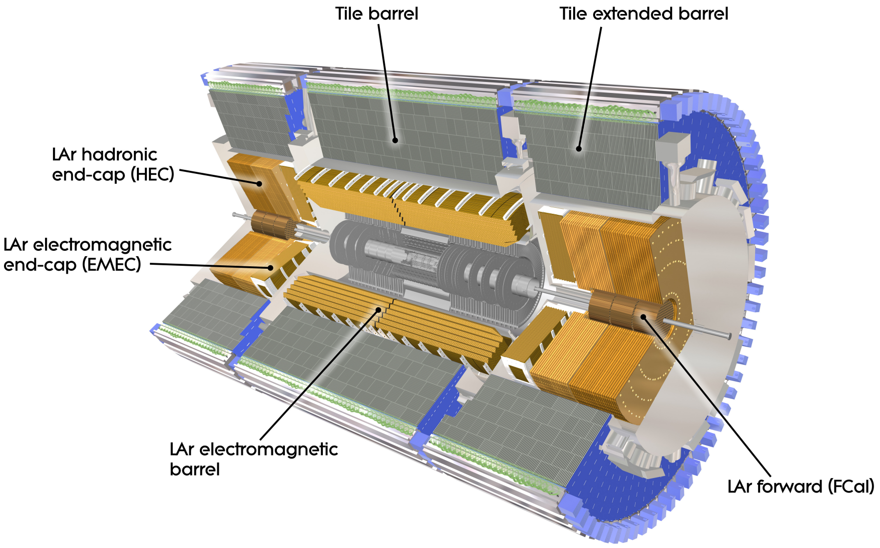

Figure 3.5: *Schematic illustration of the ATLAS calorimeters [18].*

The MS covers the pseudorapidity range $|\eta| < 2.7$ for the measurement of muons and triggers on muons in the range $|\eta| < 2.4$. In the largest part of the pseudorapidity the precision measurement is performed by **Monitored Drift Tube** chambers (MDTs) with an average resolution of $80\,\mu$m per tube and about $35\,\mu$m per chamber [20]. In the higher pseudorapidity region $2.0 < |\eta| < 2.7$ **Cathode-Strip Chambers** (CSCs) are used. CSCs are multiwire proportional chambers with a resolution of $40\,\mu$m in the bending plane and 5 mm in the transverse plane [20].
In the barrel region of the detector ($|\eta| \leq 1.05$) **Resistive Plate Chambers** (RPCs) are used to trigger on muons, whereas in the end-cap region ($1.05 \leq |\eta| \leq 2.4$) **Thin Gap Chambers** (TGCs) are used.

3.2.6 Trigger System

The ATLAS Trigger System (Figure 3.7) is designed to reduce the nominal collision event rate of 40 MHz to a final rate of 200 Hz that is recorded for analysis. In 2011, the recorded event rate exceeded the nominal value and was 400 Hz, thus doubling the number of events ready for analysis. The Trigger System is divided into three levels, L1, L2 and event filter, with each level using the information provided by the previous level and additional criteria to refine the trigger decision.

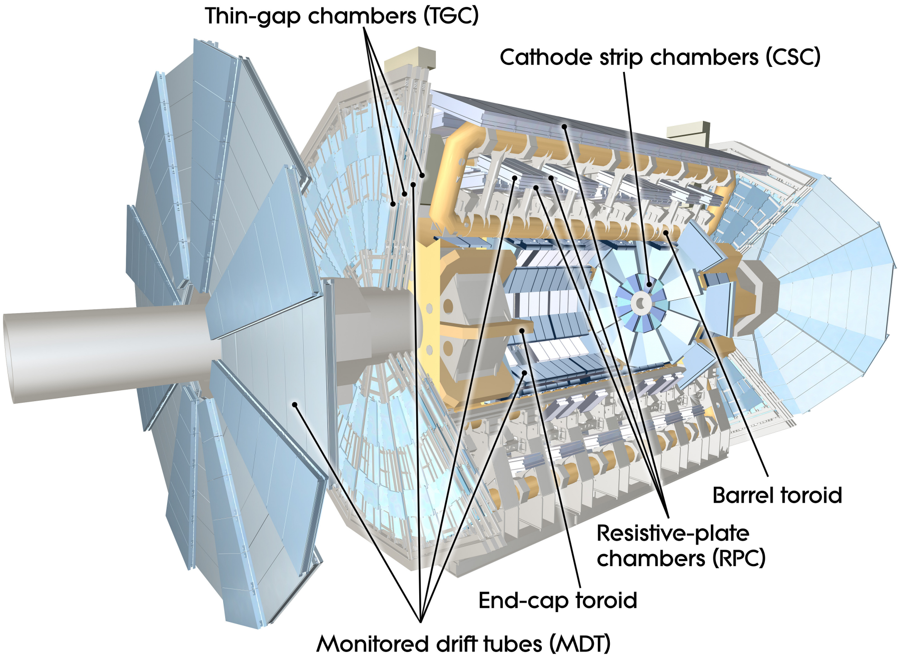

Figure 3.6: *Schematic illustration of the ATLAS Muon Spectrometer [18].*

- The L1 trigger analyses the signals of the calorimeters and the MS to identify Regions-of-Interest (RoIs), i.e. regions of the detector with interesting features. It uses the trigger chambers of the MS and information from all calorimeters at reduced granularity. The event rate is reduced to about 75 kHz in a decision making process taking less than 2.5 μs.

- The L2 trigger uses the RoI information provided by the L1 trigger. Within these RoI, the full detector information is used at full granularity and precision to further reduce the event rate to 3.5 kHz in an average time of 40 ms per event.

- The final selection of events is performed in the event filter which uses offline algorithms to reduce the event rate to around 200 Hz.

3.2.7 Computing Model

The computing infrastructure of ATLAS is organized in four distinct levels, the ‘Tiers’, within the Worldwide LHC Computing Grid (WLCG) [23].

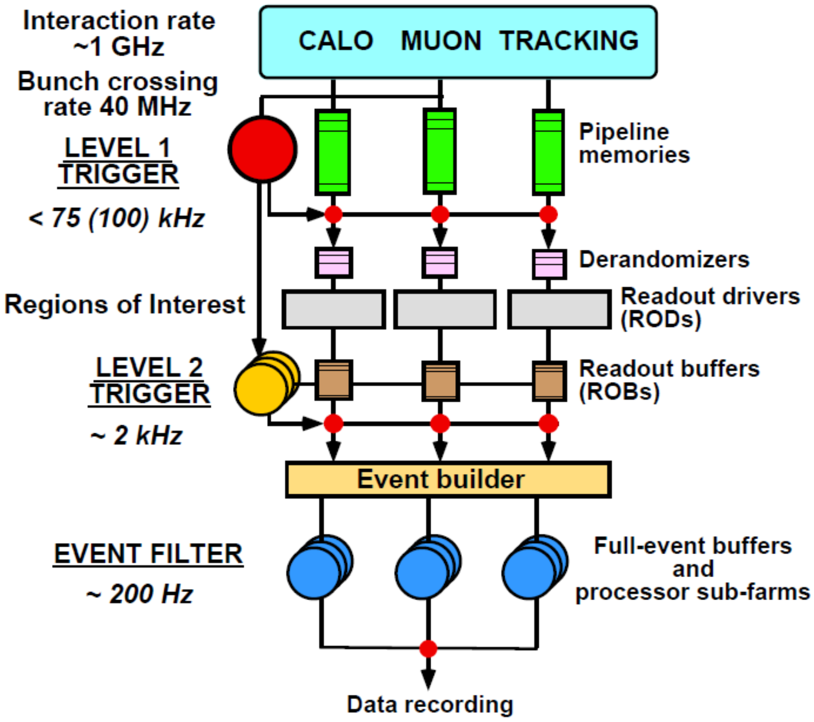

Figure 3.7: *The ATLAS Trigger chain [22].*

- The Tier-0 centre, located at CERN, records the raw data from the detector and runs the first event reconstruction (on a short timescale of 48 hrs) and calibration and alignment on the raw data. The reconstruction output as well as the raw data is distributed to the various Tier-1 centres.

- At the Tier-1 centres the reconstruction algorithm is rerun with better calibration and alignment and more sophisticated algorithms. Each Tier-1 stores and takes care of a fraction of the raw data and keeps the current versions of the data as well as the simulation on disk for analysis purposes. The reconstruction output is also further distributed to the attached Tier-2 centres.

- The main task of the Tier-2 centres is to run analysis and simulation jobs while keeping current versions of the data and the simulation available on disk.

- Tier-3s provide access to the Grid resources and local storage for end-user data and range from small computing clusters to the users' desktop computers.

3.2.8 Monte Carlo Simulation

Both the reconstruction of the data gathered by the ATLAS detector and the Monte Carlo (MC) simulation of SM processes and new physics processes is performed within the ATLAS software framework ATHENA, which is based on the Gaudi framework [24]. The MC event simulation consists of several steps. In the first step, the generation, events are generated by external MC generators. 4-vectors of all particles in the events and their vertices are produced. In the next step, the simulation, this information is used to evaluate the interaction between the generated particles and the detector material. The simulation is based on Geant4 [25]. In the third step, the digitisation, the response of the detector based on the simulated interactions is calculated. The type of information that is available after this step is the same as what can be collected from real data events. The final step in the production of MC simulated samples is the reconstruction. Using sophisticated algorithms for the different types of particles and the response information from the digitisation (or the detector information for real data events), the tracks of the particles are reconstructed.

4 Search for Multilepton SUSY Events

A search for supersymmetry in events with exactly three leptons (only electrons and muons are considered) and missing transverse momentum is presented. In this chapter general aspects of the analysis are discussed, e.g. the data and MC samples used, the selection cuts applied to the objects of interest or the definition of the signal regions.
Several different SM processes can yield events with three leptons and missing transverse momentum and thus contribute to the background. Two different classes of backgrounds are distinguished: the irreducible background, consisting of processes with three prompt and isolated leptons ('real leptons'), where prompt leptons are leptons originating from the decays of Z/γ^* and W bosons or τ leptons, and the reducible background, consisting of processes with less than three prompt and isolated leptons and at least one non-prompt or one non-isolated lepton ('fake lepton'). The most important irreducible background processes are WZ/γ^*, ZZ/γ^* and $t\bar{t}+Z/\gamma^*/W/WW$ (the latter is referred to as $t\bar{t}+V$ in the following). The main reducible backgrounds contributing mostly with one fake lepton are $t\bar{t}$, Wt (single top quark production in association with a W boson), Z/γ^* production in association with jets and WW production, while W production in association with jets, s- and t-channel single top quark and multijet production contribute with two or more fake leptons.

4.1 Data Samples

The analysis presented in this thesis is based on a data sample with an integrated luminosity of $\int L dt = 2.06\,\text{fb}^{-1}$ taken in 2011 with the ATLAS detector. The data was taken from end of March to end of August. Figure 4.1 shows the evolution of the integrated luminosity as well as the peak instantaneous luminosity per fill in 2011.

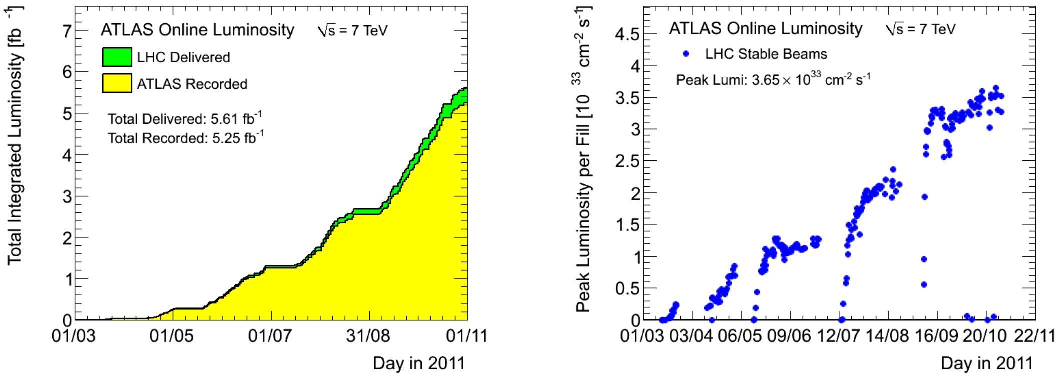

(a) Integrated luminosity (b) Peak instantaneous luminosity

Figure 4.1: *Evolution of the integrated luminosity (a) and the peak instantaneous luminosity per fill (b) in 2011 [26].*

4.2 Monte Carlo Samples

Details of the MC simulated samples for the different processes are given in Table 4.1. The last column gives the cross section of the process and states whether this cross section is calculated to leading order (LO), next-to-leading order (NLO) or next-to-next-to-leading order (NNLO). The k-factor is the factor that is applied to the cross section at LO to scale it to NLO or NNLO.
The main background processes contributing in the signal regions are the diboson production processes WZ and ZZ, both simulated with HERWIG [27], and the $t\bar{t}$ production process, simulated with MC@NLO [28]. The $b\bar{b}$ sample, simulated with PYTHIA [29], does not constitute a background to the analysis but is used in Chapter 5 when determining misidentification rates of leptons. The SUSY signal samples used for the interpretation of the results of the analysis in Chapter 6 were simulated with HERWIG++ [30].

4.3 Trigger Selection

The analysis uses a logical OR of single electron and single muon triggers with trigger thresholds at $E_{\mathrm{T}} > 20\,\mathrm{GeV}$ or $E_{\mathrm{T}} > 22\,\mathrm{GeV}$ for electrons, depending on the instantaneous luminosity, and a trigger threshold of $p_{\mathrm{T}} > 18\,\mathrm{GeV}$ for muons. At least one signal lepton (defined in Section 4.5) with transverse momentum in the efficiency plateau region of the appropriate trigger is requested. For the electron triggers this plateau region is reached at $E_{\mathrm{T}} > 25\,\mathrm{GeV}$, while for the muon triggers the plateau region is reached at $p_{\mathrm{T}} > 20\,\mathrm{GeV}$.
In the analysis data and MC are treated differently with respect to the trigger. While for

Table 4.1: *Overview of the different MC simulated samples. Details of the samples are given in the Appendix A.1. σ denotes the cross section, while the k-factor is the factor applied to scale the cross section from leading order to next-to-leading order or next-to-next-to-leading order.*

Process	Generator	$\sigma \times$ k-factor [pb]
ZZ	HERWIG [27]	6.21 (NLO)
WZ		19.1 (NLO)
W^+W^-		43.8 (NLO)
$W^\pm W^\pm$	MADGRAPH [31]	0.22 (LO)
$V\gamma$		165.2 (LO)
$t\bar{t}+V$		0.50 (NLO)
$t\bar{t}$	MC@NLO [28]	89.36 (NNLO)
Single Top		37.34 (NNLO)
Z + jets	ALPGEN [32]	3272.2 (NNLO)
W + jets		32592.3 (NNLO)
Drell-Yan		11970.6 (NNLO)
$b\bar{b}$	PYTHIA [29]	7056 (LO)
SUSY	HERWIG++ [30]	various

the data the triggers are used as described above, the trigger simulation is not used for the MC simulated samples. Instead, the efficiency of the triggers is determined from data and parameterised in several variables. These trigger efficiencies are expressed as event weights that are applied to the MC events.

4.4 Event Quality Selection

For an event to be selected for further analysis it has to satisfy a number of quality criteria.

- In general, the ATLAS detector has to be fully operational for events to be considered for the analysis.
- In order to suppress events potentially containing jets caused by instrumental effects, events are rejected whenever such a jet candidate is found. The definition of such jets is described in Section 4.5. This selection is only performed on data.
- The leading primary vertex of each event is required to have more than four tracks associated to it.

- Noise bursts in the calorimeter can lead to wrong measurements of various objects (e.g. jets or missing transverse momentum). Therefore data events with noise bursts in the LAr calorimeter are rejected.
- Cosmic muons can be detected by the ATLAS detector. Since these muons are not part of the relevant signature and can also lead to mismeasurements, events containing cosmic muons are rejected. They are identified after overlap removal (Section 4.6) as muons having a longitudinal impact parameter $|z_0| > 1\,\mathrm{mm}$ or a transverse impact parameter $|d_0| > 0.2\,\mathrm{mm}$, both measured with respect to the primary vertex.
- Events with potentially mismeasured muons are rejected.

4.5 Object Definitions

This section summarises the characteristics of electrons, muons, jets and missing transverse momentum as they are used in the analysis.

Electrons.

- Transverse energy[1] $E_\mathrm{T} > 10\,\mathrm{GeV}$ (15 GeV in the ‘crack region’ $1.37 < |\eta^{cl}| < 1.52$). In MC the energy is smeared in order to reproduce the energy resolution observed in data.
- Pseudorapidity $|\eta^{cl}| < 2.47$. η^{cl} is the pseudorapidity of the calorimeter cluster associated with the electron as opposed to η^{tr} which denotes the pseudorapidity of the ID track associated with the electron.
- Electrons are requested to be reconstructed at least with the ‘medium’ selection, which includes information about the shower shape in the EM calorimeter, energy leakage into the hadronic calorimeters, track quality requirements and track-cluster matching [33, 34].
- Electrons are rejected if they are detected in regions of the electromagnetic calorimeter where the signal cannot be read due to dead optical transmitters or calorimeter problems.

At this stage electrons are required to have a spatial separation from other electrons, jets and muons as described in Section 4.6. Electrons also passing this overlap removal are defined as ‘baseline’ electrons. ‘Signal’ electrons need to satisfy additional criteria:

---

[1] For electrons, E_T and p_T are used synonymously.

- Track based isolation $p_{\mathrm{T}}cone20/p_{\mathrm{T}} < 0.1$, where $p_{\mathrm{T}}cone20$ is the total transverse momentum of all tracks with transverse momentum $p_{\mathrm{T}} > 1\,\mathrm{GeV}$ in a cone $\Delta R \leq 0.2$ around the electron.
- 'Tight' requirement according to [34] (tighter cuts than for 'medium' electrons are applied in the reconstruction).

Muons.

- Muons are reconstructed by the STACO (STAtistical COmbination) algorithm. The analysis uses muons that have a muon spectrometer track matching an inner detector track (combined muons) and muons that are identified through an ID seed (segment tagged muons) [35].
- Transverse momentum $p_{\mathrm{T}} > 10\,\mathrm{GeV}$. In MC the transverse momentum is smeared in order to reproduce the resolution observed in data [36].
- Pseudorapidity $|\eta| < 2.4$. This corresponds to the pseudorapidity range of the muon triggers.
- Quality requirements are imposed on the track of the muon (e.g. number of hits in the different parts of the ID).

Muons passing these selection criteria and having the required spatial separation from electrons, jets and other muons according to Section 4.6 are defined as 'baseline' muons. 'Signal' muons additionally need to pass the isolation cut $p_{\mathrm{T}}cone20 < 1.8\,\mathrm{GeV}$.

Jets.

- Jets are reconstructed by the anti-k_{T} jet algorithm [37] with a distance parameter $\Delta R = 0.4$. The calorimeters measure the energy at the electromagnetic (EM) scale, which systematically underestimates the energy deposits of hadrons. This is corrected by scaling the measured electromagnetic scale momenta with a jet-energy scale correction as a function of $p_{\mathrm{T,jet}}^{\mathrm{EM}}$ and $|\eta_{\mathrm{jet}}|$. This is optimised on MC simulated samples [38].
- Transverse momentum $p_{\mathrm{T}} > 20\,\mathrm{GeV}$.
- Pseudorapidity $|\eta| < 2.8$.

Jets fulfilling these criteria are then checked for their spatial separation from electrons and muons as laid out in Section 4.6.

Events containing jets that are likely to be due to instrumental background or background due to cosmic muons are rejected [39].

Jets with a pseudorapidity $|\eta| < 2.5$ are further classified as b-jet candidates or light jets using a b-tagging algorithm ('IP3D+JetFitter' in [40]). The average b-tagging efficiency of the operating point used in the analysis is $\sim 60\%$, while the mistag rate of light flavour jets is smaller than 1% [40].

Missing transverse momentum.
Noise suppressed topological clusters calibrated to the relevant scale [41, 42] and the muons passing the muon selection cuts are used to calculate the missing transverse momentum $\not{E}_{\mathrm{T}}$ (or $E_{\mathrm{T}}^{\mathrm{miss}}$).

$$\not{E}_{\mathrm{x,y}} = E^{e}_{\mathrm{x,y}} + E^{jets}_{\mathrm{x,y}} + E^{cl}_{\mathrm{x,y}} + E^{\mu}_{\mathrm{x,y}} \tag{4.1}$$

$$\not{E}_{\mathrm{T}} = \sqrt{\not{E}_{\mathrm{x}}{}^{2} + \not{E}_{\mathrm{y}}{}^{2}} \tag{4.2}$$

where the electron term $E^{e}_{(\mathrm{x,y})}$ is calculated using electrons passing the medium selection having $E_{\mathrm{T}} > 10\,\mathrm{GeV}$; the jet term $E^{jets}_{(\mathrm{x,y})}$ is calculated with properly calibrated jets with $p_{\mathrm{T}} > 20\,\mathrm{GeV}$; the cell out term $E^{cl}_{(\mathrm{x,y})}$ covers all remaining topological clusters not associated with electrons or jets at EM scale; the muon term $E^{\mu}_{(\mathrm{x,y})}$ is calculated using all baseline muons. Each of these terms is calculated separately for the barrel, the endcap and the forward region of the ATLAS detector.

4.6 Overlap Removal

'Overlap removal' summarises two aspects of the object selection that are similar in their implementation but are performed for different reasons.

One of the aspects is the removal of objects that are overlapping due to a double counting of objects by the reconstruction algorithms. In this case only one of the two objects is an actual object while the other is an artefact of the reconstruction mechanism. This concerns electrons and jets, that are both reconstructed as jets by the jet algorithms. Therefore, any jet that is found to be closer than $\Delta R(\mathrm{e},\mathrm{jet}) < 0.2$ to an electron after applying the object selection criteria is discarded. It can also happen that an electron is erroneously reconstructed twice. In order to reject the second electron, whenever two electrons are found within $\Delta R(\mathrm{e}_1,\mathrm{e}_2) < 0.1$, the electron with the lower energy is discarded.

The other aspect is the spatial separation of two objects. Leptons can arise from the semileptonic decay of b or c quarks inside a jet. These leptons should in general be rejected by the isolation requirements described in Section 4.5 but a sizeable contribution of leptons inside jets passing the isolation requirements can be seen. Electrons and muons are thus required to be separated from jets by more than $\Delta R(\mathrm{lep},\mathrm{jet}) = 0.4$. Muons and electrons are also seen to overlap in the detector when a muon emits bremsstrahlung and the resulting photon is misidentified as an electron. Both objects are rejected in this case if they overlap within $\Delta R(\mu, \mathrm{e}) < 0.1$ as both are likely to be badly reconstructed.

4.7 MC Event Weights

The MC events have to be reweighted to account for differences observed with respect to the data.

Lepton Identification Efficiency The electron and muon reconstruction efficiency seen in data and MC is different. Therefore, for each electron and muon, an $E_{\mathrm{T}}/p_{\mathrm{T}}$- and η-dependent scale factor needs to be applied to each MC event to correct for these differences.

The ***b*-tagging efficiency** and mis-tag rate of light flavour jets is also observed to be different between data and MC. Each selected jet with $|\eta| < 2.5$ is thus assigned a p_{T}- and η-dependent scale factor that is used to correct the MC event weight. The true particle information of the MC simulation is used to determine the flavour of the jets in MC [40].

Pileup The term pileup can be separated into two effects, in-time pileup and out-of-time pileup. In-time pileup is caused by multiple proton-proton interactions in the same bunch crossing as several hard interactions can occur in one crossing of the beams. This type of pileup was dominant in the early stages of data taking (2010) and the number of reconstructed vertices in an event was used as a measure of the in-time pileup. Out-of-time pileup denotes the detector activity caused by earlier bunch crossings. This pileup became increasingly relevant in the 2011 data taking as the bunch separation was reduced to 50 ns. This type of pileup is not well described by the number of reconstructed vertices but the average number of pileup interactions $<\mu>$ is used instead. $<\mu>$ is a measure of the expected average number of proton-proton collisions per event and is directly correlated to the instantaneous luminosity. The MC simulated samples described in Section 4.2 were planned to describe the data to be taken in 2011 but had to be generated before the data taking. At that time the actual pileup conditions in the data were unknown. Therefore the simulation of the pileup conditions was chosen to cover a range as wide as possible. This is parameterised in $<\mu>$. Unfortunately the distribution of $<\mu>$ in MC is much broader than in data as shown in Figure 4.2. Therefore an event weight needs to be applied to each MC event, in a way that after reweighting all events in a MC simulated sample the distributions of $<\mu>$ in MC and in data are the same. This is referred to as 'pileup reweighting'.

Two different measures of μ are used in data:

- The first method uses the $<\mu>|_{\mathrm{LB,BCID}}$ value averaged over all bunch crossing IDs (BCIDs) in the luminosity block (LB). This method is better suited to take

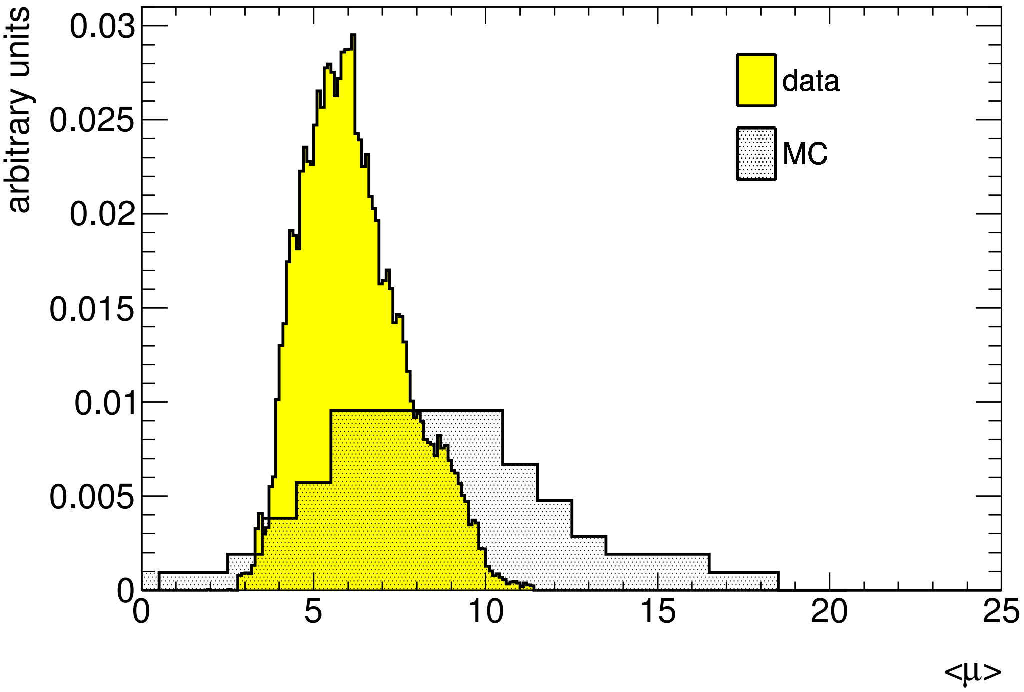

Figure 4.2: *Distributions of* $<\mu>$ *in data and MC before pileup reweighting for an integrated luminosity* $\int Ldt = 2.06\,fb^{-1}$ *normalised to unity.*

into account out-of-time pileup. It is used as the nominal method for the pileup reweighting.

- The second method uses the $<\mu>|_{\mathrm{LB(BCID)}}$ value per BCID averaged across the LBs in a run. This better describes the in-time pileup and is used to determine the systematic effects introduced by the procedure.

4.8 Preselection

In order to suppress Drell-Yan processes and decays of low-mass particles (e.g. Υ and J/Ψ), same flavour opposite sign (SFOS) baseline lepton pairs with an invariant mass $m_{\mathrm{ll}} < 20\,\mathrm{GeV}$ are discarded from the events. This selection is performed after all quality and trigger requirements. Events satisfying all selections outlined in this chapter are said to pass the preselection if they also contain at least three signal leptons (unless otherwise specified ‘leptons’ from here on are always meant to be ‘signal leptons’). This selection region is also referred to as the ‘baseline signal region’.

4.9 Signal and Control Regions

The main signature investigated in this analysis is the pair production of neutralinos and charginos. Especially the next-to-lightest neutralino can decay to the lightest neutralino either directly with an on-shell or off-shell Z boson (depending on the mass difference of the neutralinos) or via a slepton. In both cases a SFOS lepton pair is produced. Therefore, after the preselection, signal events are required to contain exactly three leptons and at least one SFOS lepton pair. In order to be sensitive to both decay modes, two orthogonal signal regions with exactly three leptons are defined:

- Z-depleted signal region (SR1)
  - at least one SFOS lepton pair;
  - $\not{E}_{\mathrm{T}} > 50\,\mathrm{GeV}$;
  - Z veto (reject events with a SFOS lepton pair with an invariant mass within $10\,\mathrm{GeV}$ of the Z boson mass, $m_Z = 91.2\,\mathrm{GeV}$ is used);
  - b-jet veto (reject events containing at least one b-tagged jet).
- Z-enriched signal region (SR2)
  - Z boson requirement (at least one SFOS lepton pair with an invariant mass within $10\,\mathrm{GeV}$ of the Z boson mass);
  - $\not{E}_{\mathrm{T}} > 50\,\mathrm{GeV}$.

The cut on the missing transverse momentum is motivated by the presence of a stable LSP at the end of each SUSY decay chain, typically resulting in a sizeable amount of missing transverse momentum. The b-jet veto applied to SR1 helps to contain the background from the $t\bar{t}$ process by reducing it by 50%. Table 4.2 summarises the events from MC simulated samples passing the different cuts for the SM background processes relevant to the analysis and one SUSY reference point from the simplified model scenario.

In addition to the signal regions three control regions are defined. The first two control regions are used to validate the final background estimate and are dominated by two different SM processes:

- $Z+$jets dominated control region (VR1)
  - pass preselection;
  - exactly three signal leptons;
  - $30\,\mathrm{GeV} < \not{E}_{\mathrm{T}} < 50\,\mathrm{GeV}$.

- $t\bar{t}$ dominated control region (VR2)
  - pass preselection;
  - exactly three signal leptons;
  - no SFOS lepton pair;
  - $\not{E}_{\mathrm{T}} > 50\,\mathrm{GeV}$.

The third control region, denoted CR1, is used to study a discrepancy between the observed data and the MC simulation presented in Section 5.2. The requirements in this control region are:

- pass preselection;
- at least three signal leptons (events with more than 3 leptons are negligible as shown in Figure A.1 in the appendix);
- $\not{E}_{\mathrm{T}} < 50\,\mathrm{GeV}$.

Table 4.2: *Numbers of events for SM processes and one SUSY reference point at different stages of the event selection. The quoted uncertainties are statistical only. The irreducible background processes are* $t\bar{t}+V$, WZ, *and* ZZ, *while all other are reducible background processes. All numbers are normalised to* $\int Ldt = 2.06\,fb^{-1}$. *'SUSY ref. point' refers to one SUSY point in the simplified model scenario with parameters* $m_{\tilde{\chi}_1^\pm}, m_{\tilde{\chi}_2^0}, m_{\tilde{l}_L}, m_{\tilde{\chi}_1^0} = 150, 150, 100, 50\,\mathrm{GeV}$.

			SR1			SR2	
Selection	exactly 3 l	SFOS	$\not{E}_{\mathrm{T}} > 50\,\mathrm{GeV}$	Z veto	b-jet veto	With Z	$\not{E}_{\mathrm{T}} > 50\,\mathrm{GeV}$
SUSY ref. point	294±8	293±8	180±6	124±5	122±5	101±5	55.4±3.5
$t\bar{t}$	48.3±1.6	34.2±1.3	22.6±1.1	19.3±1.0	9.4±0.7	5.5±0.5	3.3±0.4
Single t	3.9±0.7	3.6±0.6	2.2±0.4	1.9±0.4	1.5±0.4	0.26±0.15	0.26±0.15
$t\bar{t}+V$	7.37±0.22	6.45±0.20	4.41±0.17	1.69±0.11	0.38±0.05	4.22±0.16	2.72±0.13
ZZ	33.3±1.0	32.9±1.0	4.12±0.33	0.75±0.15	0.70±0.15	27.3±0.9	3.37±0.30
WZ	192±5	190±5	69.2±2.9	10.7±1.2	10.6±1.2	159±4.4	58.4±2.7
WW	0.24±0.08	0.22±0.08	0.11±0.05	0.09±0.05	0.09±0.05	0.043±0.030	0.021±0.021
$V\gamma$	50±7	50±7	0±1.3	0±1.3	0±1.3	15±4	0±1.3
Z + jets	364±14	363±14	2.3±0.9	1.0±0.7	1.0±0.7	248±11	1.2±0.6
W + jets	2.5±2.5	2.5±2.5	0±1.4	0±1.4	0±1.4	0±1.4	0±1.4
DY	7.2±3.2	7.2±3.2	0±0.16	0±0.09	0±0.09	0±0.09	0±0.09
Σ red. bkg.	426±15	411±15	27.2±2.1	22.3±1.9	12.0±1.8	254±11	4.8±1.6
Σ irred. bkg.	283±9	279±9	77.7±10.2	13.1±1.8	11.7±1.8	206±6	64.5±3.0
Σ SM	709±17	690±17	105±4	35.5±2.6	23.7±2.5	459±12	69.3±3.4

5 Standard Model Background

5.1 Classification of the Background

Two different types of SM background processes are distinguished and treated differently in the analysis.

The first type of background processes are the irreducible background processes. These processes contain three prompt and isolated ('real') leptons from the decays of W bosons and Z bosons (and photons). For the modelling of these background processes the prediction of the MC simulation is used. The dominant background contributions estimated in this way are the WZ/γ^{*}, ZZ/γ^{*} and $t\bar{t}+V$ processes.

The second type of background processes are the reducible background processes. The common characteristic of these processes is the presence of at least one 'fake' lepton. The term 'fake lepton' comprises two different categories of objects. The first are non-prompt leptons, mainly leptons from the semileptonic decay of b quarks, but also electrons from photon conversions. The second are jets that are misidentified as leptons. The background processes containing fake leptons are predicted using the data-driven matrix method (as described in Sections 5.3 and 5.4). The dominant contributions estimated in this way are $t\bar{t}$ production, single top quark production, WW diboson production, Z/γ^{*} and W production in association with jets.

In order to further motivate the classification of the different processes, the composition of the background with respect to the origin of the leptons is studied on MC simulated samples. The true particle information from the MC simulation (referred to as 'truth level' or 'truth information') is used to perform the study. The reconstructed leptons found in the events are matched to corresponding leptons at truth level, that are classified according to their origin in the MC decay chain. Five different categories are distinguished in this analysis:

- **Prompt** or **real leptons** originate from the decay of W bosons, Z bosons or τ leptons, and any lepton not in this category is considered to be a fake lepton;
- **Heavy flavour leptons** originate from the semileptonic decay of b and c quarks, including bound states containing these particles (e.g. J/Ψ);

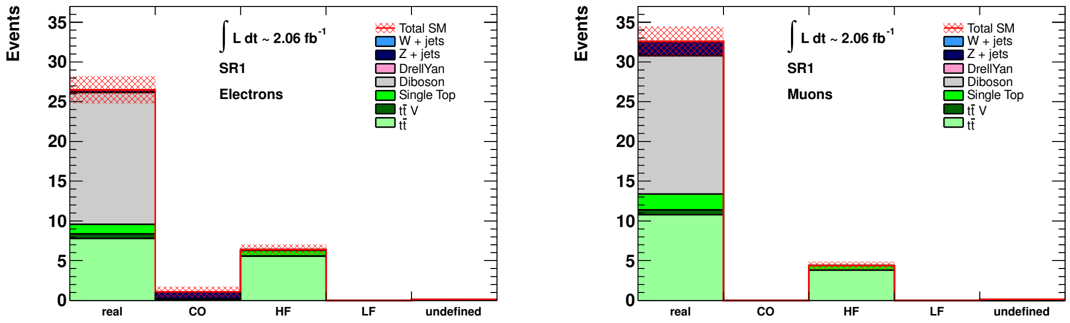

(a) SR1: Electrons (b) SR1: Muons

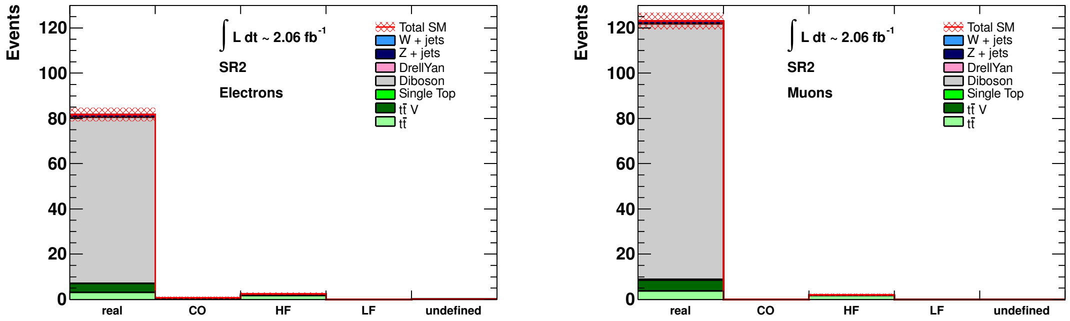

(c) SR2: Electrons (d) SR2: Muons

Figure 5.1: *Sources of leptons after all cuts in the two signal regions. The red line represents the sum of all SM background processes. The hatched red area around the red line represents the uncertainty. All uncertainties are statistical only.*

- **Conversion leptons** are leptons originating from a photon that is not produced in the fundamental process (e.g. bremsstrahlung);
- **Light flavour leptons** are leptons originating from jets that are not already comprised in the heavy flavour definition;
- **Undefined leptons** are reconstructed leptons that could not be matched to a truth level particle, thus not being classified into any of the previous categories.

Figure 5.1 illustrates the sources of the leptons graphically for SR1 and SR2, while Tables 5.1 and 5.2 summarise the results in numbers. Both confirm that the dominant source of reducible background is $t\bar{t}$ production in both signal regions, while the diboson processes are the main contribution to the irreducible background, especially in SR2, where

Table 5.1: *Dominant sources of electrons and muons in SR1 categorised in real, heavy flavour, light flavour and photon conversion candidates (electrons only). The percentages are shown over the total background. The quoted uncertainties are statistical. If no events pass the selection, the statistical uncertainty is set equal to 1.1 event scaled by the sample luminosity. HF denotes leptons from heavy flavour decays, LF leptons from light flavour decays and CO electrons from photon conversions.*

Process	Electrons in %				
	prompt	HF	LF	CO	undefined
Z + jets	1 ± 1	0.4 ± 0.4	0 ± 0.3	3 ± 2	0.1 ± 0.1
Diboson	49 ± 3	0 ± 0.1	0 ± 0.1	0.2 ± 0.1	0 ± 0.1
$t\bar{t}$	23 ± 2	16 ± 2	0 ± 0.1	0.4 ± 0.2	0.2 ± 0.1
Single Top	4 ± 1	2 ± 1	0 ± 0.1	0 ± 0.1	0 ± 0.1
$t\bar{t}\,V$	1.7 ± 0.2	0.1 ± 0.1	0 ± 0.1	0 ± 0.1	0 ± 0.1
SM total	78 ± 2	19 ± 2	0 ± 0.4	3 ± 2	0.3 ± 0.2

Process	Muons in %			
	prompt	HF	LF	undefined
Z + jets	5 ± 2	0 ± 0.3	0 ± 0.3	0 ± 0.3
Diboson	47 ± 3	0 ± 0.1	0 ± 0.1	0 ± 0.1
$t\bar{t}$	29 ± 2	10 ± 1	0 ± 0.1	0 ± 0.1
Single Top	5 ± 1	2 ± 1	0 ± 0.1	0.3 ± 0.3
$t\bar{t}\,V$	1.6 ± 0.2	0 ± 0.1	0 ± 0.1	0 ± 0.1
SM total	88 ± 1	12 ± 1	0 ± 0.4	0.3 ± 0.3

the expected background is largely dominated by these processes. It also becomes apparent that fake leptons from light flavour decays are negligible compared to the other sources. Leptons that cannot be matched to a truth level particle are a negligible contribution as well. This information is used later when determining fake rates (Section 5.6).

5.2 Motivation of Data-Driven Background Estimation

In this section a study of an observed discrepancy between the MC simulation and the data is presented. The study is performed in the control region CR1 defined in Section 4.9. Figure 5.2 shows various distributions in CR1. A discrepancy between the MC prediction and the observed data can be seen in the region with missing transverse momentum $\not{E}_{\mathrm{T}} < 20\,\mathrm{GeV}$, while events with one or more jets do not seem to be affected by the ex-

Table 5.2: *Dominant sources of electrons and muons in SR2 categorised in real, heavy flavour, light flavour and photon conversion candidates (electrons only). The percentages are shown over the total background. The quoted uncertainties are statistical. If no events pass the selection, the statistical uncertainty is set equal to 1.1 event scaled by the sample luminosity. HF denotes leptons from heavy flavour decays, LF leptons from light flavour decays and CO electrons from photon conversions.*

Process	Electrons in %				
	prompt	HF	LF	CO	undefined
Z + jets	2 ± 1	0.7 ± 0.4	0 ± 0.1	0.5 ± 0.5	0 ± 0.1
Diboson	86 ± 1	0 ± 0.1	0 ± 0.1	0.3 ± 0.2	0 ± 0.1
$t\bar{t}$	4 ± 1	1.9 ± 0.4	0 ± 0.1	0 ± 0.1	0.1 ± 0.1
Single Top	0.1 ± 0.1	0.2 ± 0.1	0 ± 0.1	0 ± 0.1	0 ± 0.1
$t\bar{t}V$	4.6 ± 0.2	0 ± 0.1	0 ± 0.1	0 ± 0.1	0 ± 0.1
SM total	96 ± 1	3 ± 1	0 ± 0.2	0.9 ± 0.5	0.1 ± 0.2

Process	Muons in %			
	prompt	HF	LF	undefined
Z + jets	1.0 ± 0.4	0.2 ± 0.2	0 ± 0.1	0 ± 0.1
Diboson	90 ± 1	0 ± 0.1	0 ± 0.1	0 ± 0.1
$t\bar{t}$	3.0 ± 0.3	1.3 ± 0.2	0 ± 0.1	0 ± 0.1
Single Top	0.3 ± 0.2	0.1 ± 0.1	0 ± 0.1	0 ± 0.1
$t\bar{t}V$	3.8 ± 0.2	0 ± 0.1	0 ± 0.1	0 ± 0.1
SM total	98.4 ± 0.3	1.6 ± 0.3	0 ± 0.2	0 ± 0.2

cess. The MC prediction for the transverse momentum of the leading jet is in very good agreement with the observed data. Figure 5.2(d) shows that the discrepancy is only seen in events with at least one lepton with $p_{\mathrm{T}} < 20\,\mathrm{GeV}$. In order to further investigate the source of the discrepancy between the MC prediction and the observed data, the events are separated according to their lepton flavour content. Figure 5.3 shows the transverse momentum of the leading lepton for each event in the dominant flavour channels (the channels with leptons of the same sign are shown in the appendix in Figure A.2, and can be seen to have far fewer events than the channels with leptons of opposite sign). The control region is largely dominated by the Z + jets process, where a SFOS lepton pair is expected. The three muon channel clearly shows the largest discrepancy between the data and the simulation and the channel with an SFOS electron pair and a muon also shows an excess. The three electron channel shows reasonable agreement within the statistical uncertainty while the channel with an SFOS muon pair and an electron shows only a slight excess. To summarise, the excess is most prominent in the channels with an SFOS lepton pair and an additional muon. Therefore the properties of the muons in the control region CR1 are further investigated.

Figure 5.4 shows the effect of increasing the transverse momentum threshold for all muons in steps of 2 GeV from 10 GeV to 20 GeV. This is clearly not desirable as the signal that is investigated can have a soft lepton spectrum, especially for the third leading lepton. But the distributions illustrate that the excess is related to muons with a low transverse momentum $p_{\mathrm{T}} < 20\,\mathrm{GeV}$ and in general the muon with the lowest transverse momentum in the event. Thus, several properties of these muons are investigated in the three muon channel.

Figures 5.5 and 5.6 display distributions of different parameters of the muons. The pseudorapidity distribution (Figure 5.5(a)) shows that the excess is not located in a specific detector region but is spread over the full range. Figure 5.5(b) shows that the excess muons are well isolated ($p_{\mathrm{T}}cone20 = 0$ meaning that there is no additional track with a transverse momentum larger than 1 GeV around the muon). Figures 5.5(c) and 5.5(d) illustrate that the discrepancy is not related to a problem with the reconstruction of the muons but rather indicate that the excess muons are well reconstructed. Since combined muons (defined in Section 4.5) are reconstructed in the ID and the MS, they are supposedly better reconstructed than segment tagged muons, but the excess is mainly seen in combined muons. Similarly, a large difference in the measured transverse momentum between the ID and the MS would hint at a bad reconstruction, but the excess of events is found for muons with only a small ($< 1\,\mathrm{GeV}$) difference in transverse momenta. An excess due to cosmic muons is also considered and abandoned based on Figures 5.6(a), 5.6(b) and 5.6(c). The excess of events is concentrated at absolute values of both the transverse and the longitudinal impact parameters d_0 and z_0 around 0, which indicates muons originating from the primary vertex of the event. In addition, the sum of the pseudorapidities of oppositely charged muons is expected to peak at around 0 for cosmic muons, which clearly is not the case for the muons discussed here. Finally, Figure 5.6(d) shows the transverse momentum of the jet closest to the muon with a spatial separation $\Delta R < 0.4$ (with $p_{\mathrm{T}}^{\mathrm{jet}} = 0$ when no jet is found). The cut discussed in Section 4.6, where muons are required to be separated from jets with $\Delta R > 0.4$, only uses jets with a transverse momentum $p_{\mathrm{T}} > 20\,\mathrm{GeV}$. The jets investigated here thus have a transverse momentum $p_{\mathrm{T}} < 20\,\mathrm{GeV}$. A jet transverse momentum of 0 indicates the absence of a jet close to the muon, which is the case for most of the muons. This result points to well reconstructed muons again.

In summary, the simulation is seen to be missing well reconstructed muons at low transverse momenta. In order to not heavily rely on the MC simulation in the signal regions, a data-driven background estimation method is investigated.

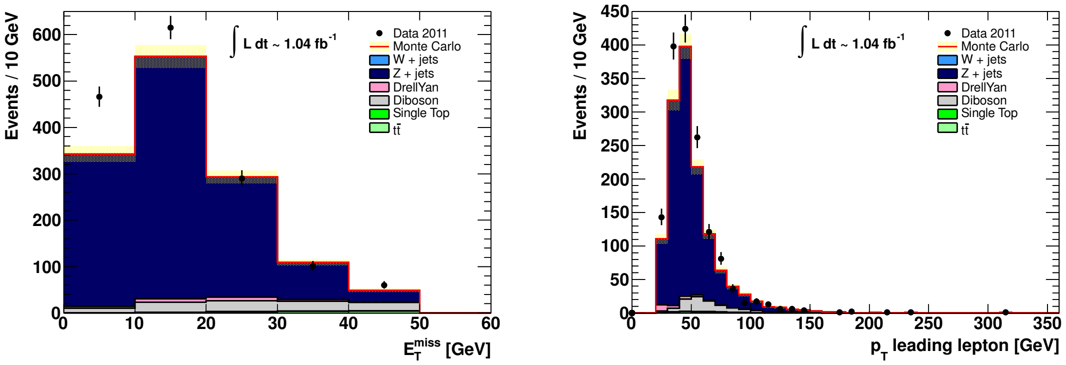

(a) Missing transverse momentum (b) Leading lepton p_{T}

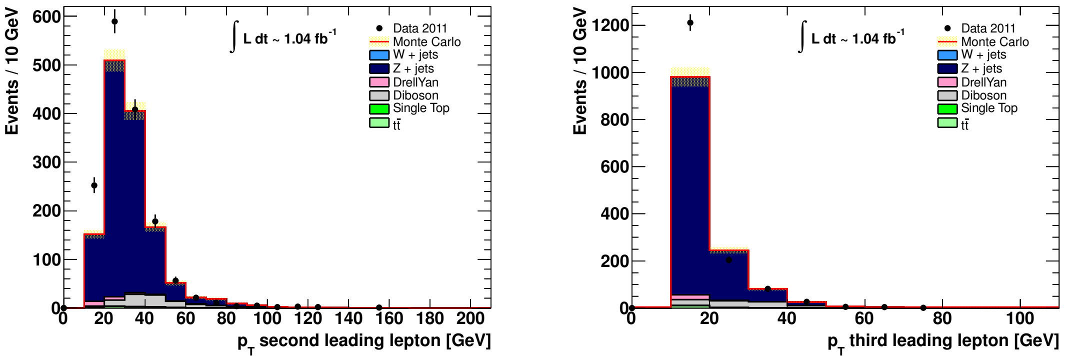

(c) Second leading lepton p_{T} (d) Third leading lepton p_{T}

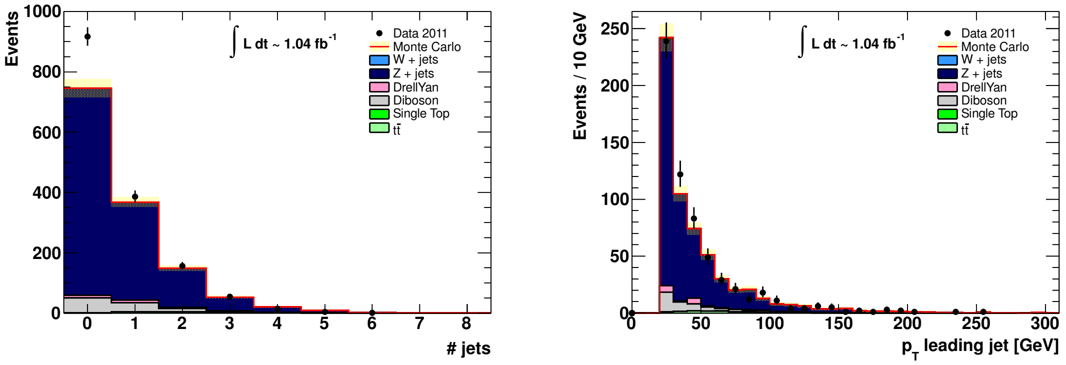

(e) Number of jets (f) Leading jet p_{T}

Figure 5.2: *Various distributions in the control region CR1. The red line represents the sum of all SM background processes. The yellow area around the red line represents the uncertainty. All uncertainties are statistical only.*

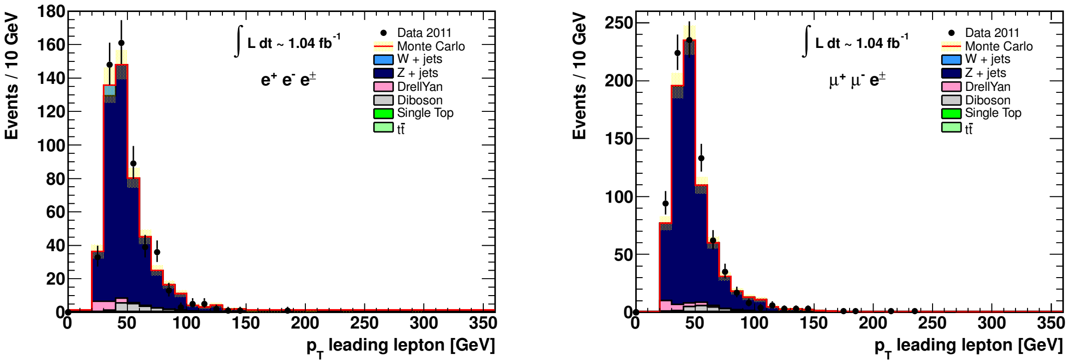

(a) $e^+e^-e^\pm$ (b) $\mu^+\mu^-e^\pm$

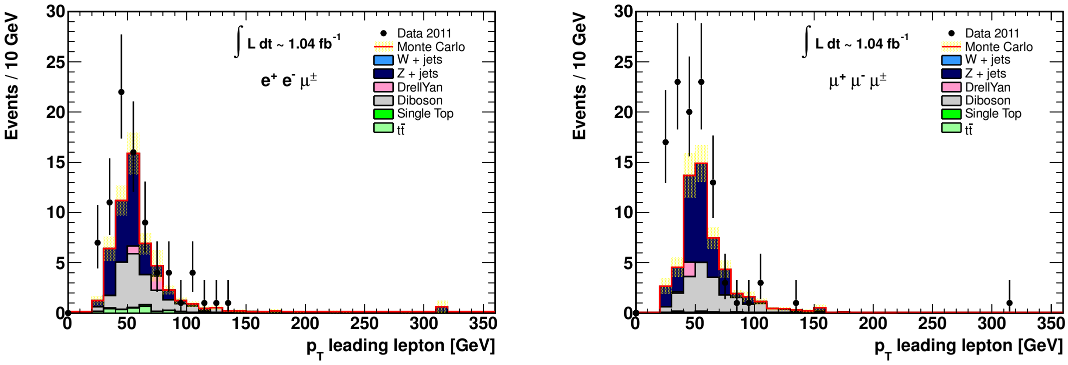

(c) $e^+e^-\mu^\pm$ (d) $\mu^+\mu^-\mu^\pm$

Figure 5.3: *Transverse momentum of the leading lepton in different channels in the control region CR1. The red line represents the sum of all SM background processes. The yellow area around the red line represents the uncertainty. All uncertainties are statistical only.*

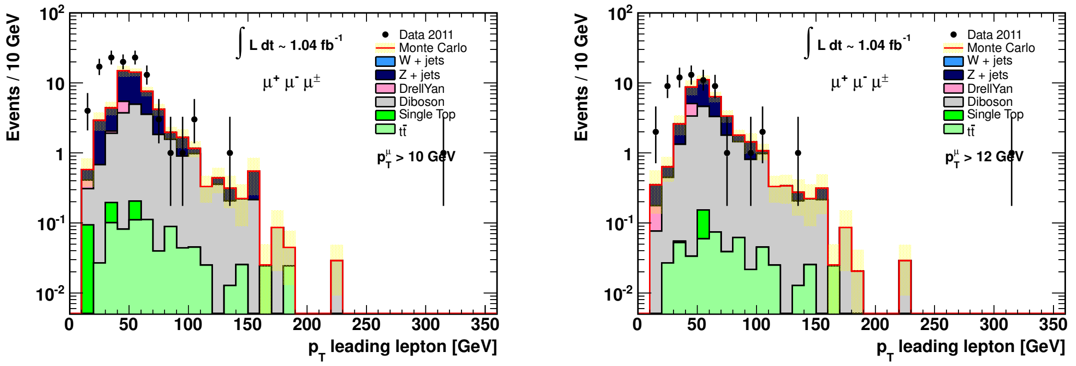

(a) $p_{\mathrm{T}}^{\mu} > 10\,\mathrm{GeV}$ (b) $p_{\mathrm{T}}^{\mu} > 12\,\mathrm{GeV}$

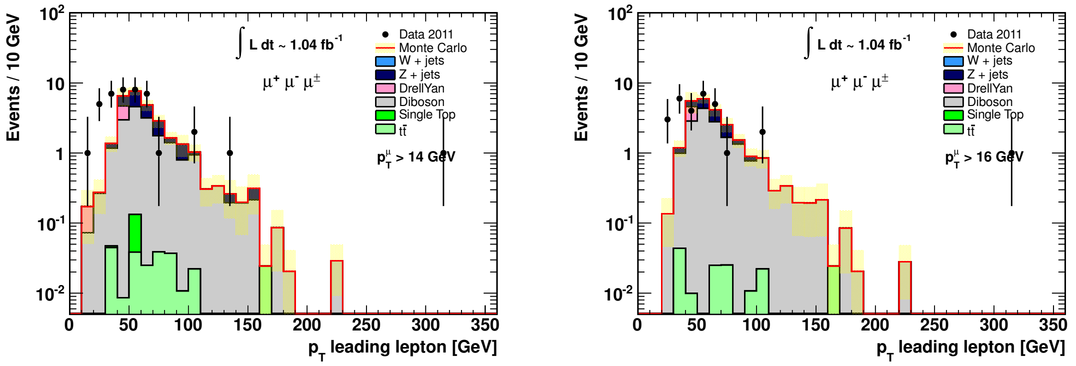

(c) $p_{\mathrm{T}}^{\mu} > 14\,\mathrm{GeV}$ (d) $p_{\mathrm{T}}^{\mu} > 16\,\mathrm{GeV}$

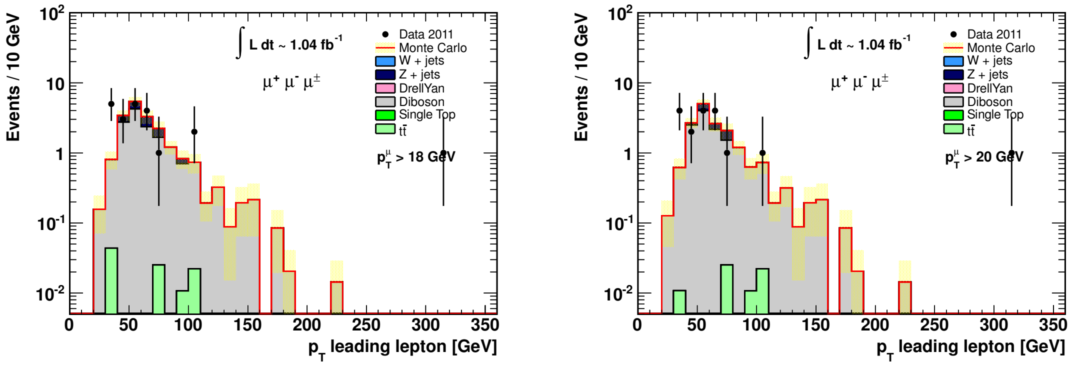

(e) $p_{\mathrm{T}}^{\mu} > 18\,\mathrm{GeV}$ (f) $p_{\mathrm{T}}^{\mu} > 20\,\mathrm{GeV}$

Figure 5.4: *Transverse momentum of the leading lepton for different transverse momentum thresholds of muons in $\mu^+\mu^-\mu^\pm$ events in the control region CR1. The red line represents the sum of all SM background processes. The yellow area around the red line represents the uncertainty. All uncertainties are statistical only.*

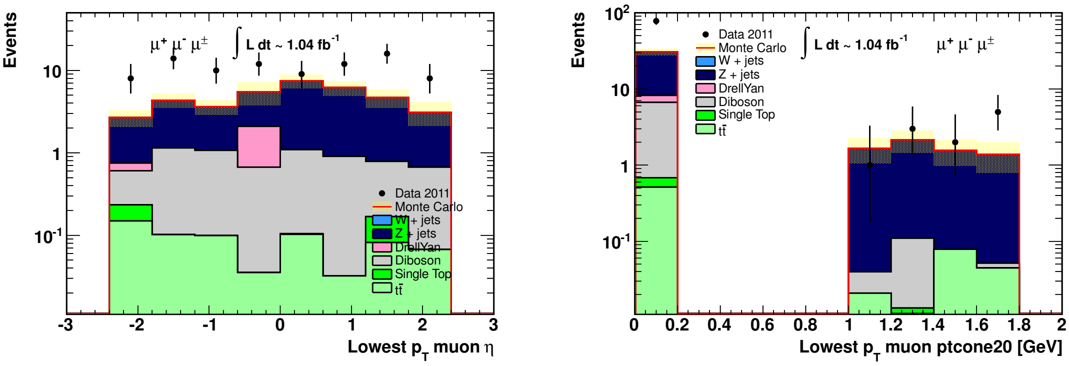

(a) Pseudorapidity η

(b) $p_{\mathrm{T}}cone20$

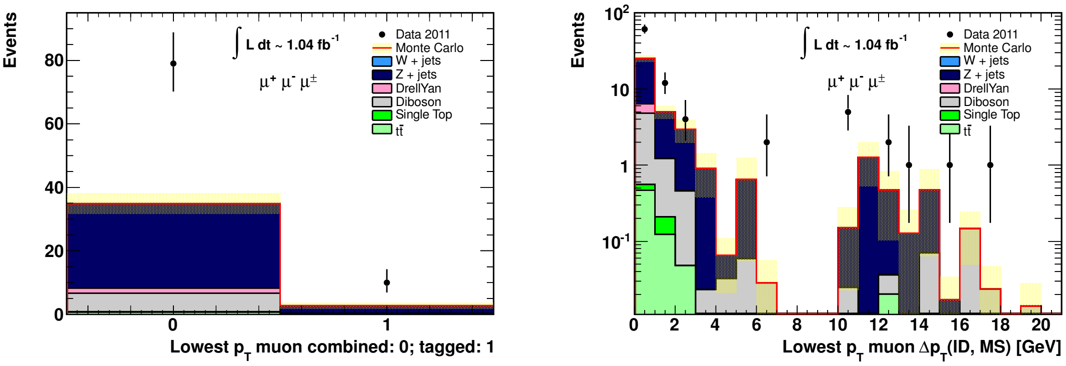

(c) Combined or segment tagged muons

(d) $|p_{\mathrm{T}}^{ID} - p_{\mathrm{T}}^{MS}|$

Figure 5.5: *Various distributions for the muon with the lowest transverse momentum in* $\mu^{+}\mu^{-}\mu^{\pm}$ *events in the control region CR1. The red line represents the sum of all SM background processes. The yellow area around the red line represents the uncertainty. All uncertainties are statistical only.*

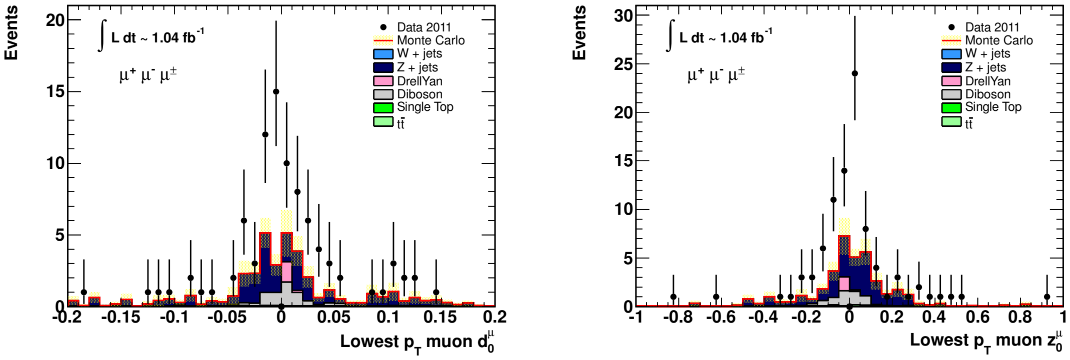

(a) Transverse impact parameter d_0

(b) Longitudinal impact parameter z_0

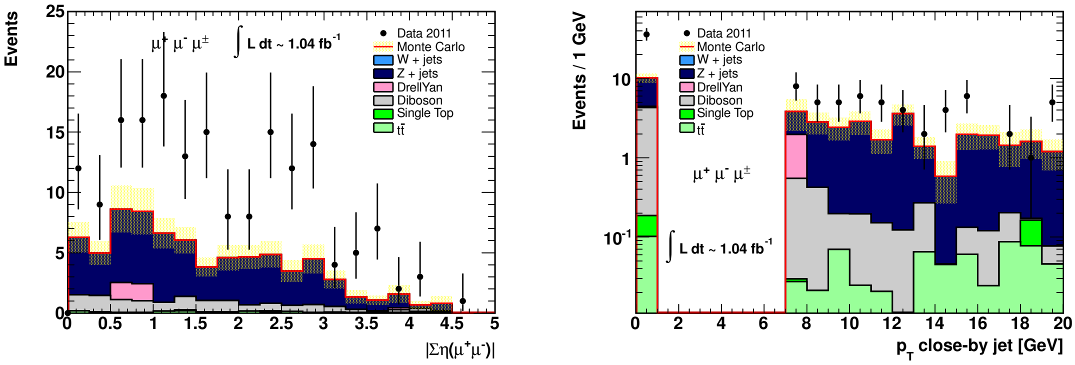

(c) Absolute sum of pseudorapidities η of oppositely charged muon pairs

(d) p_T of close-by jet

Figure 5.6: *Various distributions for the muon with the lowest transverse momentum in $\mu^+\mu^-\mu^\pm$ events in the control region CR1. The red line represents the sum of all SM background processes. The yellow area around the red line represents the uncertainty. All uncertainties are statistical only.*

5.3 Matrix Method

The matrix method [43] is a data-driven background estimation method, applied to events with one or more leptons. The basic assumption of the method is that real and fake leptons can be distinguished by their characteristics. Two sets of identification criteria for the leptons are defined, one loose set (L) and one tight set (T). The number of events with leptons satisfying the loose or the tight identification criteria, N_L and N_T, can be measured in data. The idea is then to express the number of events with loose and tight leptons as a function of the number of events with real and fake leptons. For events with one lepton this leads to:

$$N_T = \varepsilon \times N_R + f \times N_F, \tag{5.1}$$

$$N_{L'} = (1-\varepsilon) \times N_R + (1-f) \times N_F, \tag{5.2}$$

where ε is the probability of a loose real lepton to pass the tight requirement ('efficiency'), f is the probability of a loose fake lepton to pass the tight requirement ('fake rate'), the index L' refers to events with a loose but not tight lepton and the indices R and F denote real or fake leptons. Since this is a system of two equations with two unknowns (N_R and N_F) it can be written as a matrix (hence the name of the method):

$$\begin{pmatrix} N_T \\ N_{L'} \end{pmatrix} = \begin{pmatrix} \varepsilon & f \\ (1-\varepsilon) & (1-f) \end{pmatrix} \cdot \begin{pmatrix} N_R \\ N_F \end{pmatrix}. \tag{5.3}$$

The efficiency ε and the fake rate f need to be determined independently and are typically measured from data in appropriate control regions dominated by real or fake leptons, respectively. Once these values and N_L and N_T are known the matrix can be inverted and the expected number of events with a real or a fake lepton at the loose selection level obtained. The number of events with a fake lepton passing the tight selection criteria is then simply calculated as:

$$N_T^{fake} = f \times N_F. \tag{5.4}$$

Following the results of the previous Section 5.2, a matrix method like the one described above is used to estimate the number of events with two real leptons and an additional fake muon. The tight identification criteria used here correspond to signal leptons while the loose criteria correspond to baseline leptons (as defined in Section 4.5). The method is applied to events with two oppositely charged muons and an additional muon, defined as the 'signal region' for this test. It is assumed that this region contains mostly events with two real muons of opposite charge and a third fake muon. As indicated above, the fake rate needs to be determined in an appropriate control region. This control region is chosen to be the region with two oppositely charged electrons and an additional muon.

Table 5.3: *Muon fake rate obtained from a QCD enriched control region in three bins of transverse momentum [44].*

$10-20\,\mathrm{GeV}$	$20-30\,\mathrm{GeV}$	$>30\,\mathrm{GeV}$
0.65	0.37	0.25

In this way the muons used to determine the fake rate can be assumed to have similar kinematic properties as the fake muons in the 'signal region' and the measured fake rate is applicable to the 'signal region'. The fake rate is calculated according to:

$$f = \frac{N_T - b_T}{N_L - b_L}, \tag{5.5}$$

where N_T and N_L are the number of events measured from data with leptons with tight and loose identification criteria and b_T and b_L are the number of background events in the control region, i.e. the events without fake leptons but with three real leptons. The number of background events is determined from MC simulated samples and the contributing processes are assumed to be WZ and ZZ diboson production in the present case. These backgrounds need to be subtracted when calculating the fake rate and have to be added to the estimate of the matrix method.

Measuring a single non-binned fake rate results in $f = 0.517 \pm 0.003$ (statistical uncertainty). Figure 5.7 shows the resulting estimate for the distribution of the transverse momentum of the muons in the 'signal region' with three muons. For transverse momenta $p_\mathrm{T} > 30\,\mathrm{GeV}$ the prediction is in very good agreement with the observed data, but especially at low transverse momenta $p_\mathrm{T} < 20\,\mathrm{GeV}$ the difference between the prediction and the data is huge.

A different set of fake rates (listed in Table 5.3), binned in transverse momentum and measured from a QCD enriched control region, is then applied, now not only to the 'signal region' with three muons, but also to the former control region with two oppositely charged electrons and a muon. This is illustrated in Figure 5.8. It can be seen that the estimate for the three muon 'signal region' is now in good agreement for low transverse momenta, whereas the data is hugely overestimated in the region with electrons, meaning that the fake rates are not compatible between the two regions. Since the analysis does not differentiate between final states with different lepton flavour content, this ansatz is not pursued any further.

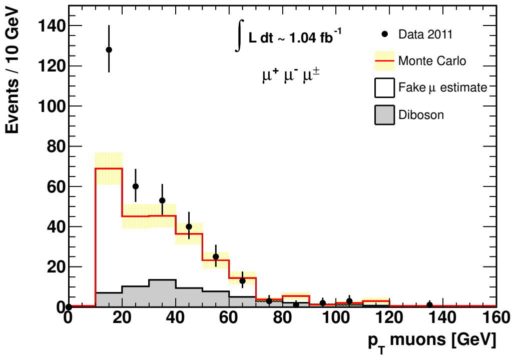

Figure 5.7: *Transverse momentum of the muons in the matrix method test region. The red line represents the sum of the irreducible SM background processes and the estimate from the matrix method. The yellow area around the red line represents the uncertainty. All uncertainties are statistical only.*

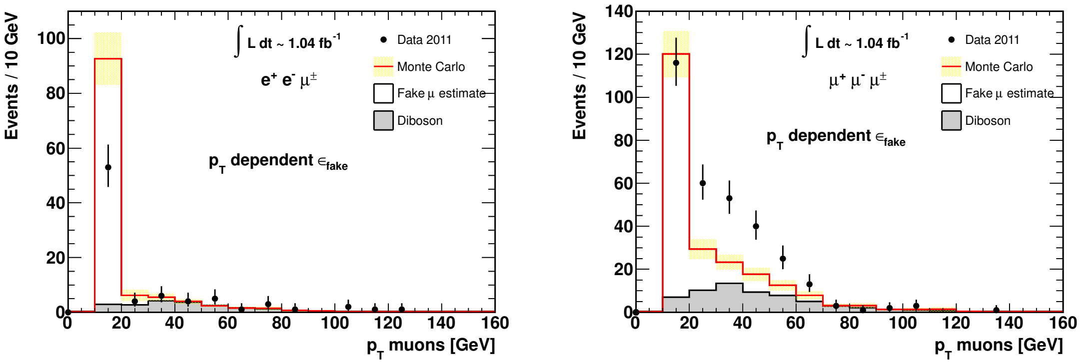

(a) $e^+e^-\mu^\pm$ (b) $\mu^+\mu^-\mu^\pm$

Figure 5.8: *Transverse momentum of the muons in two different regions when applying a* p_T*-dependent fake rate obtained from a QCD-enriched control region. The red line represents the sum of the irreducible SM background processes and the estimate from the matrix method. The yellow area around the red line represents the uncertainty. All uncertainties are statistical only.*

5.4 Final Matrix Method Implementation

For the final prediction of the SM background in the two signal regions, a matrix method describing events with one or two fake leptons (electrons as well as muons) is used. The matrix for events with two fake leptons is a 4 × 4 matrix:

$$\begin{pmatrix} N_{TT} \\ N_{TL'} \\ N_{L'T} \\ N_{L'L'} \end{pmatrix} = \begin{pmatrix} \varepsilon_1\varepsilon_2 & \varepsilon_1 f_2 & f_1\varepsilon_2 & f_1 f_2 \\ \varepsilon_1(1-\varepsilon_2) & \varepsilon_1(1-f_2) & f_1(1-\varepsilon_2) & f_1(1-f_2) \\ (1-\varepsilon_1)\varepsilon_2 & (1-\varepsilon_1)f_2 & (1-f_1)\varepsilon_2 & (1-f_1)f_2 \\ (1-\varepsilon_1)(1-\varepsilon_2) & (1-\varepsilon_1)(1-f_2) & (1-f_1)(1-\varepsilon_2) & (1-f_1)(1-f_2) \end{pmatrix} \cdot \begin{pmatrix} N_{RR} \\ N_{RF} \\ N_{FR} \\ N_{FF} \end{pmatrix}, \qquad (5.6)$$

with all parameters defined as before. Events passing the tight (T) selection contain three signal leptons, whereas for events passing the loose (L) selection the leading lepton is required to be a signal lepton and the two subleading leptons are required to be baseline leptons. The matrix method is only applied to the two subleading leptons. The leading lepton is not used in the matrix and is assumed to be a real lepton. This assumption is studied in detail in MC simulated samples of the various background processes that may contribute to the background in the signal regions.

Figure 5.9 shows the sources of all leptons in SR1 at the loose selection level, broken down into first, second or third leading lepton and separated into flavours. The numbers for the leading lepton are also summarised in Table 5.4. Both the table and the figures show that the assumption that the leading lepton in each event is a real lepton is correct for more than 99% of the events.

Since the SM background in SR2 mostly comprises irreducible background with three real leptons and only a small component of reducible background that is described by the matrix method, in the following only results and studies for SR1 will be shown. It is still important to note that the results and the reasonings hold for both signal regions.

Table 5.4: *Percentage of real leptons for the leading lepton at loose selection level in SR1. The quoted uncertainties are statistical.*

Process	Real tight leading leptons in %
W + jets	100 ± 9
Z + jets	98.55 ± 1.46
DrellYan	100 ± 6
Diboson	99.95 ± 0.05
$t\bar{t}$	99.25 ± 0.26
Single Top	99.90 ± 0.10
$t\bar{t}V$	99.96 ± 0.03
SM total	99.39 ± 0.24

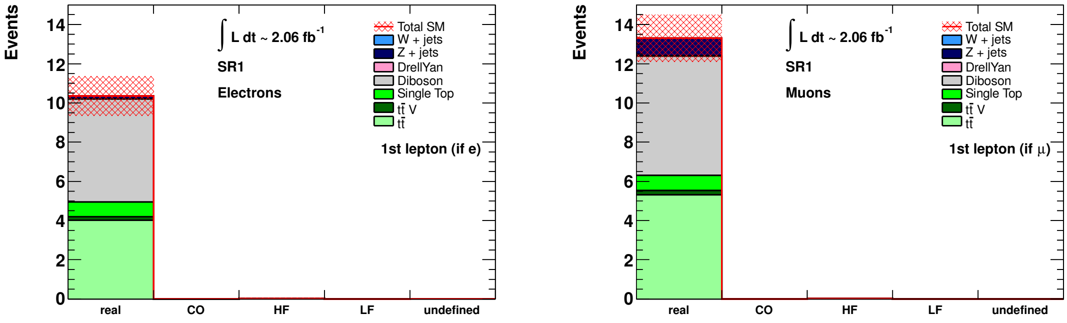

(a) Leading lepton (electron)

(b) Leading lepton (muon)

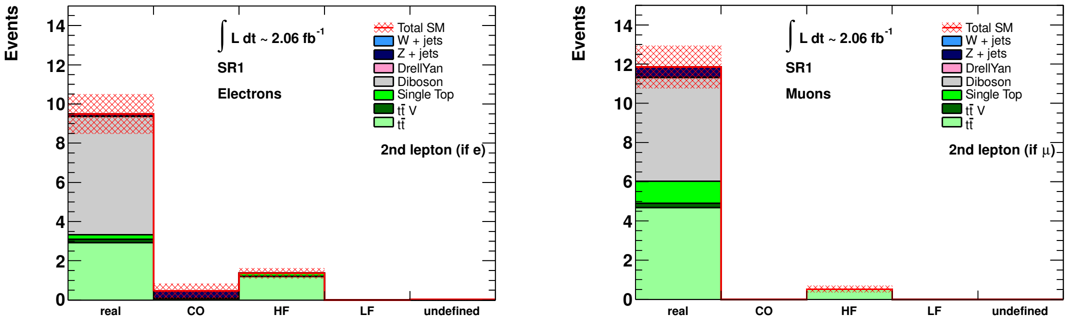

(c) Second leading lepton (electron)

(d) Second leading lepton (muon)

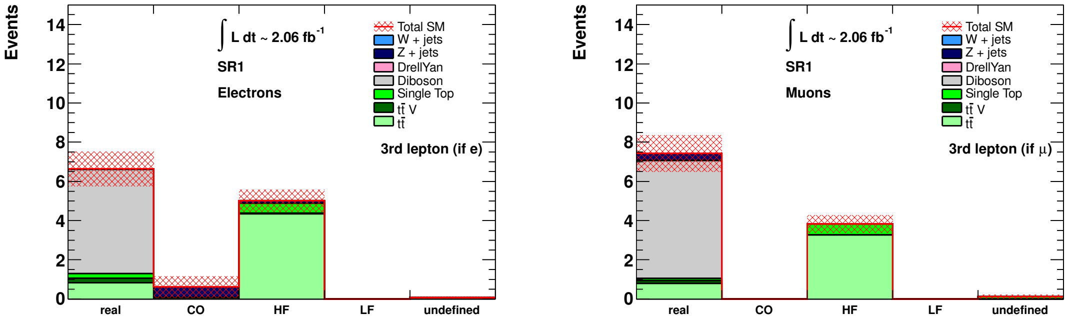

(e) Third leading lepton (electron)

(f) Third leading lepton (muon)

Figure 5.9: *Sources of leptons after all cuts in SR1 broken down into leading, second leading and third leading electron or muon. The red line represents the sum of all SM background processes. The hatched red area around the red line represents the uncertainty. All uncertainties are statistical only.*

5.5 Real Lepton Efficiencies

One important aspect of the matrix method is the measurement of the efficiency of loose real leptons to also pass the tight selection. It is measured in data in $Z \to l^+l^-$ events using a tag-and-probe method. By selecting dilepton events with an invariant mass of the dilepton system within 5 GeV of the nominal mass of the Z boson ($m_Z = 91.2\,\text{GeV}$ is used) a very pure sample of real leptons is selected.

The events selected for the tag-and-probe method are required to pass the same preselection as the signal events except for the three lepton requirement (Section 4.8). Then exactly two SFOS baseline leptons are required. One of the two leptons (the 'tag' lepton) is required to satisfy the signal lepton criteria and to be matched to the trigger. The probability of the second lepton ('probe' lepton) to fulfill the signal lepton requirement is measured by counting of events and represents the efficiency:

$$\varepsilon = \frac{N_{probe}^{signal}}{N_{probe}^{total}}. \tag{5.7}$$

If both leptons in an event satisfy the tag lepton requirements, the roles of the leptons are also inversed. This way any bias due to systematically choosing one lepton as the tag over the other (e.g. the lepton with higher transverse momentum) is avoided. The efficiency is measured for electrons and muons independently and parameterised as a function of the transverse momentum of the leptons. The results are shown in Figure 5.10.

5.6 Fake Rates

Another important aspect of the matrix method is the determination of the fake rates. Typically, fake rates are determined in data in appropriate control regions enriched with the type of fake objects that need to be studied. It has to be ensured that the kinematic properties of the studied objects in the control region are similar to those in the regions where the fake rate will be applied. This is a major challenge for the present analysis, where several different background processes contribute to the same category of fake objects. As an example, heavy flavour leptons (as defined in Section 5.1) are dominantly produced in $t\bar{t}$ events but are also found in Z + jets events (Table 5.1). Another important point is that, at least for the electrons, two distinct types of fakes can be distinguished in the MC simulated SM background: heavy flavour electrons and conversion electrons (as defined in Section 5.1). The former are certainly dominant, but the latter should nevertheless not be neglected. There is no reason to assume that the fake rates for these two different types of fake electrons are the same.

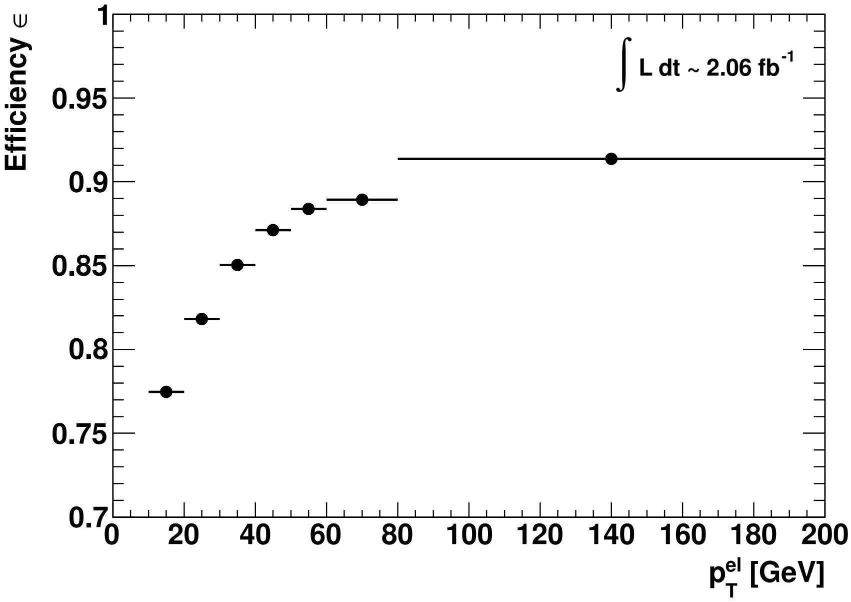

(a) Electrons

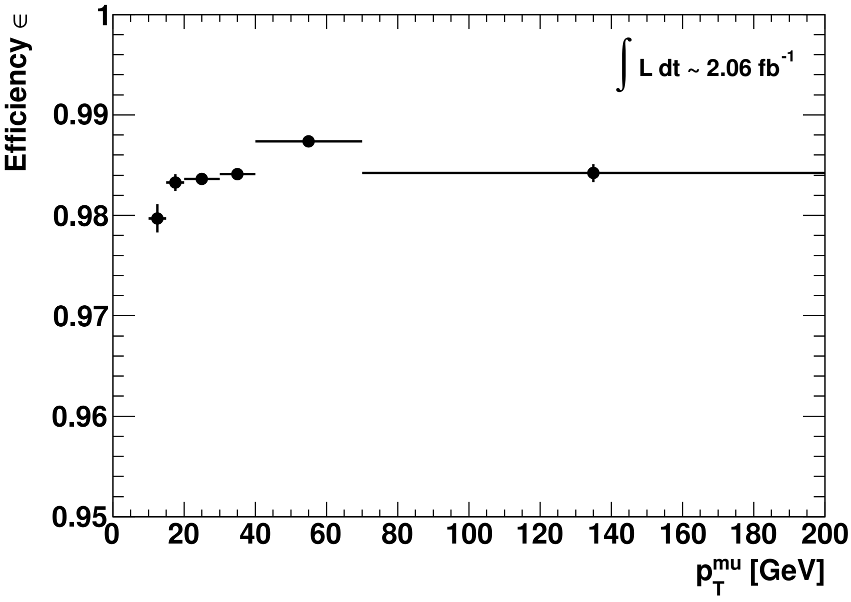

(b) Muons

Figure 5.10: *Real lepton identification efficiency for electrons (a) and muons (b) as a function of the transverse momentum.*

5.6.1 Motivation of MC-Driven Determination of Fake Rates

In order to determine a fake rate of heavy flavour leptons, a sample of dijet events with jets originating from b quarks seems optimal, as it will likely contain only very few background events (i.e. events where the leptons have a different source). In order to test the kinematic properties of the fake leptons in this sample, a study on corresponding MC samples is performed. Figure 5.11(a) shows the distribution of the transverse momentum of heavy flavour muons in three different types of SM processes. Clearly, the transverse momentum spectrum of heavy flavour muons extends to higher transverse momenta in $t\bar{t}$ events compared to $b\bar{b}$ and Z + jets events and the shape of the distributions is different. For the $b\bar{b}$ process the fake muons tend to have a smaller transverse momentum than for the $t\bar{t}$ process. It is therefore not clear whether a fake rate extracted from $b\bar{b}$ events is suitable for the $t\bar{t}$ dominated signal regions. As shown in Figure 5.11(b) the different shapes of the transverse momentum distributions translate into a different dependence of the fake rates on the transverse momentum of the muons. In general, the fake rate of muons in

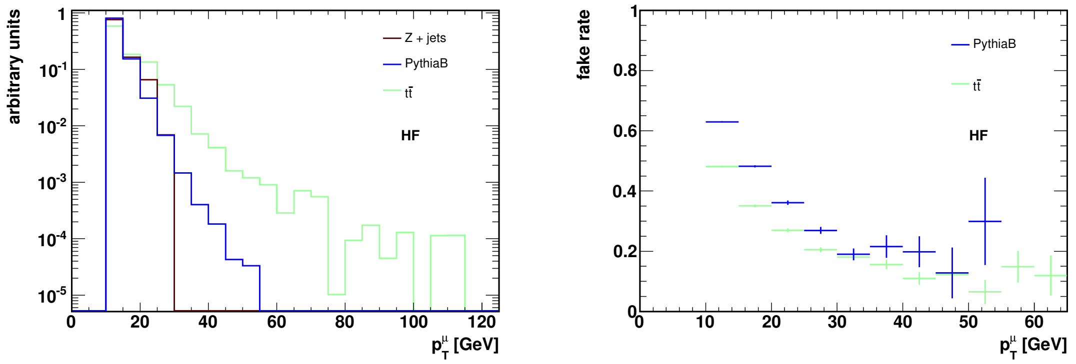

(a) Transverse momentum of heavy flavour muons (b) Fake rate of heavy flavour muons vs. p_{T}^{μ}

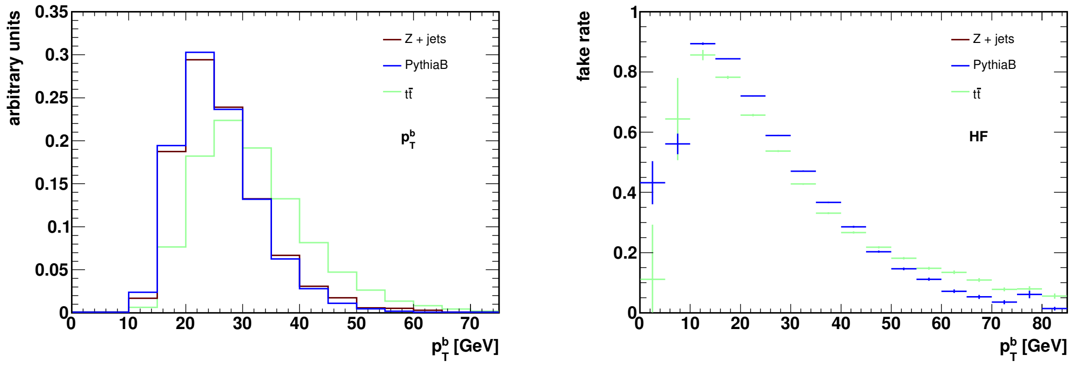

(c) Transverse momentum of b quarks (d) Fake rate of heavy flavour muons vs. p_{T}^{b}

Figure 5.11: *Transverse momentum and fake rate of heavy flavour muons.*

the $b\bar{b}$ MC samples is higher than for $t\bar{t}$ for a given value of the transverse momentum. This can be understood when looking at the distribution of the transverse momentum of the corresponding b quarks in Figure 5.11(c). The b quarks giving rise to a fake muon in the $t\bar{t}$ process tend to have a higher transverse momentum than those in the $b\bar{b}$ process. Figure 5.11(d) shows the fake rate of muons plotted against the transverse momentum of the associated b quarks instead of the transverse momentum of the muons. In this case the difference between the fake rates for the $t\bar{t}$ and the $b\bar{b}$ process are much smaller.

In conclusion, the fake rate of the muons is not universal across different processes when evaluated in dependence of the transverse momentum of the muon. When treated in dependence of the transverse momentum of the associated b quark, the fake rate becomes much more similar between the different processes. Of course, this information is not accessible in data but only in MC simulated samples. For this reason the fake rates for the present analysis are not determined from data. A method relying on MC simulated samples and applying a correction factor between data and MC is explored in the following sections.

5.6.2 Determination of Fake Rates

As mentioned in the last section, the fake rates for the present analysis are determined from MC simulated samples. To this end the classification detailed in Section 5.1 is used to distinguish fake types. This way, two problems with fake rates determined from data outlined in Section 5.6 can be avoided. The first issue was discussed in the last section and concerns the non-universality of fake rates of heavy flavour leptons across different processes. The second issue is related to the different types of fakes, i.e. heavy flavour leptons and conversion leptons. There is no reason to assume their fake rates to be equal, but in data (e.g. when applying the matrix method) there is also no way to determine the source of a lepton and thus distinguish between real leptons or fake leptons of any kind. Likewise, for any individual event in data, it is impossible to determine the type of process involved. But the fake rate was seen to be process-dependent, at least for heavy flavour muons. These two dependencies can be taken into account when calculating the fake rates from MC simulated samples.

A weighted average of the individual fake rates per process and per fake type is calculated for electrons and muons independently and also for each signal or control region separately. The weight is calculated using the SM prediction of MC simulated samples for each process and fake type:

$$f_{\mathrm{R}} = \sum_{i,j} (sf^{i} \times w_{\mathrm{R}}^{ij} \times f^{ij}), \tag{5.8}$$

where the sum over i is a sum over the involved fake types (heavy flavour, HF, or conversion, CO), the sum over j is a sum over the participating processes (e.g. $t\bar{t}$ or $Z+\text{jets}$), sf^{i}

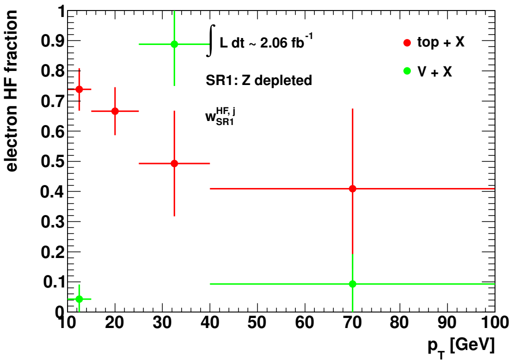

Figure 5.12: *Fraction of heavy flavour electrons* $w_{\mathrm{SR1}}^{HF,j}$ *for two different types of processes in SR1.*

denotes a scale factor to correct the MC-based fake rate for differences seen with respect to data, f^{ij} is the fake rate per fake type i and per process j and finally w_{R}^{ij} is the SM weight, while the index $\mathrm{R} = \mathrm{SR1}, \mathrm{SR2}, \mathrm{CR}$ denotes the signal or control region to which the fake rate is to be applied. A parameterisation in transverse momentum or pseudorapidity is implied for each of the terms whenever appropriate.

The sum over i is only applied to electrons as the MC simulated samples used for the analysis do not contain muons from photon conversion processes. This contribution is found to be small in comparison to the other background processes in a dedicated study. For the electrons two different types of fakes are considered in the sum, heavy flavour fakes and conversion fakes. Heavy flavour leptons comprise all categories of leptons that are not real leptons and not conversion leptons according to the definitions in Section 5.1, i.e. light flavour leptons and undefined leptons, which are mostly negligible in the signal regions according to Tables 5.1 and 5.2, are included in this category.

For the sum over the processes j two different types are distinguished. All processes containing a top quark are combined, i.e. $t\bar{t}$, single top quark production and $t\bar{t}+V$ (where V stands for any of the electroweak vector bosons), and referred to as ‘top + X’ in the figures, while ‘V + X’ refers to all other processes containing at least one electroweak vector boson, i.e. $Z+$jets, $W+$jets and Diboson production.

w_{R}^{ij} is the fraction of objects of type i in the process j in the region R. It has to be calculated for each region individually since the fraction of fake types and the fraction of each process may be different in each region. It is evaluated from MC simulated samples as the ratio of fake leptons of type i in the process j over the total number of fakes in all processes. Figure 5.12 shows the fraction of heavy flavour electrons for the two different types of processes in SR1. The lower fraction of heavy flavour leptons at higher transverse momenta seen for the top + X processes is expected since those leptons are mainly expected at low transverse momenta where they constitute the dominant contribution to the fake leptons in top + X processes. The fraction of conversion electrons per process is simply calculated as $w_{\mathrm{R}}^{CO,j} = 1 - w_{\mathrm{R}}^{HF,j}$.

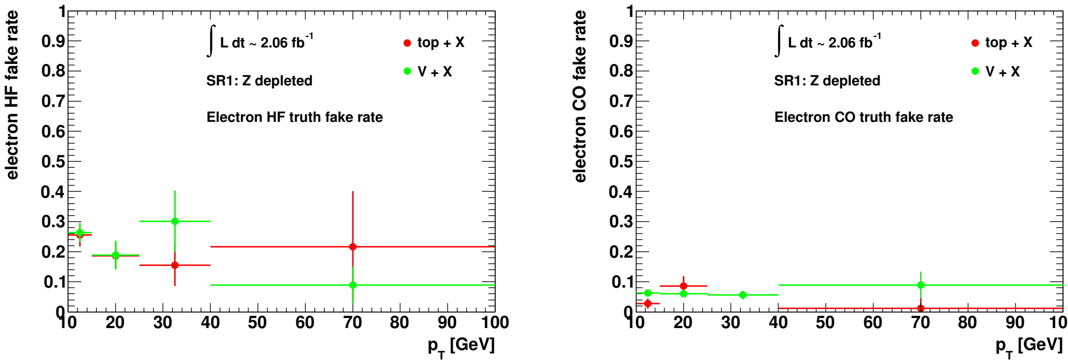

(a) Heavy flavour electron fake rate

(b) Conversion electron fake rate

Figure 5.13: *Fake rates f^{ij} of heavy flavour electrons $f^{HF,j}$ and conversion electrons $f^{CO,j}$.*

The scale factor sf^i is assumed to depend only on the type of fake i and not on the process j or the region R. It is measured in appropriate control regions dominated by the respective type of fake objects and found to be consistent with 1 within the statistical uncertainty.

The fake rates f^{ij} are determined per fake type i and per process j as the ratio of the number of leptons satisfying the signal lepton criteria over the number of leptons satisfying the baseline lepton criteria. The events selected for the fake rate determination must pass the preselection (as defined in Section 4.8) except for the lepton isolation requirements. In order to determine fake rates compatible with the matrix method, events where the leading lepton is a signal lepton are selected and the fake rates are determined using the two subleading leptons. By not applying further requirements on the events (e.g. the cut on the missing transverse momentum applied to the signal regions), the statistical uncertainty on the fake rates f^{ij} can be reduced. The cuts on the SFOS lepton pairs and on the b jets only slightly affect the fake rates, while the dependence on the missing transverse momentum is taken into account as a systematic uncertainty.

Figure 5.13 shows the fake rates f^{ij} of electrons obtained from the MC simulated samples. The two fake rates from heavy flavour electrons and conversion electrons are clearly different for both processes and differences are also seen between the top + X and the V + X processes within one type of fake. In summary, the fake rate of conversion electrons is below 10% in the full range of transverse momentum with a mostly flat distribution, while the maximum of the fake rate of heavy flavour electrons is around 30%, overall decreasing with higher transverse momentum.

Figure 5.14 shows the fake rate $f^{HF,j}$ of muons. Again, as expected, for both processes the fake rate is decreasing with higher transverse momenta of the muons. The difference in the fake rates between the two processes expected after the study presented in the last section is confirmed.

The final fake rates f_R determined with this method are displayed in Figures 5.15 and 5.16. Figure 5.15(a) shows three fake rates for electrons parameterised in transverse momentum: the final weighted average (black points), but also the fake rates for the top + X and the V + X processes alone for illustrative purposes. Figure 5.15(b) shows the weighted average fake rate of electrons in three different ranges of the pseudorapidity. One can see that the fake rate depends on the pseudorapidity and therefore the electron fake rate is also parameterised in this variable in the way displayed here. Finally, Figure 5.16 shows the final fake rate of muons. The results for SR2 are shown in the appendix in Figures A.3 and A.4.

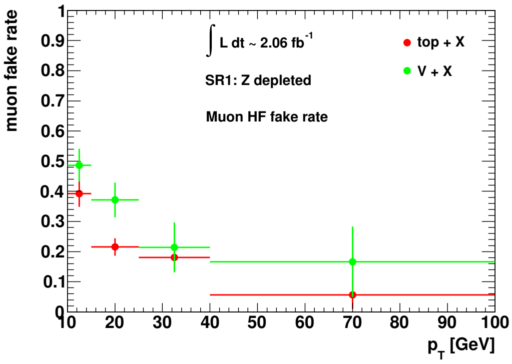

Figure 5.14: *Fake rate $f^{HF,j}$ of heavy flavour muons.*

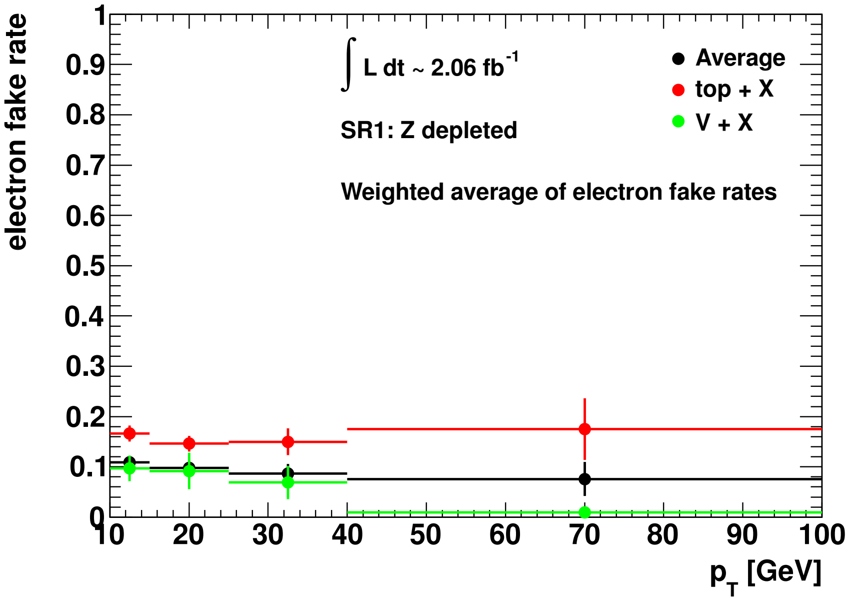

(a) Final electron fake rate

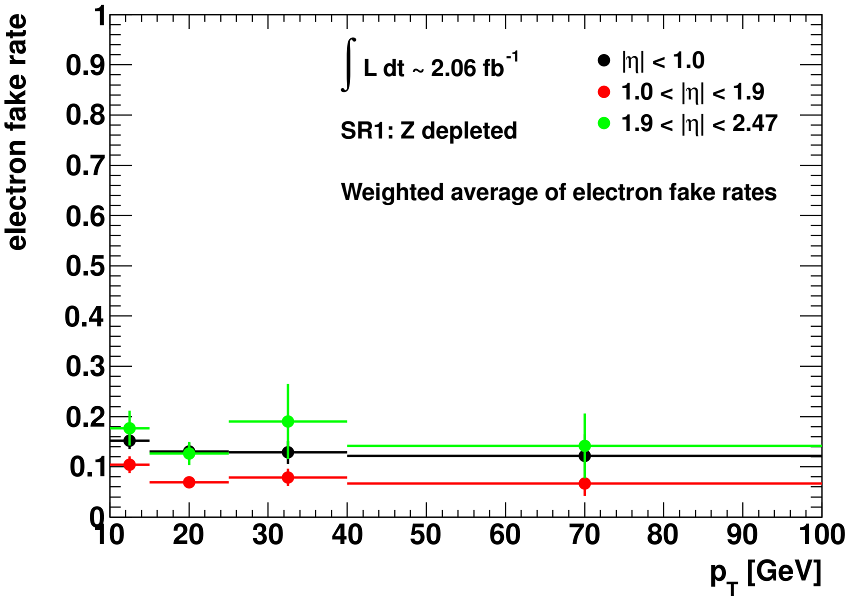

(b) Final electron fake rate in three bins of pseudorapidity

Figure 5.15: *Final fake rates of electrons in SR1. Both the final average and individual fake rates for the two processes are shown in (a).*

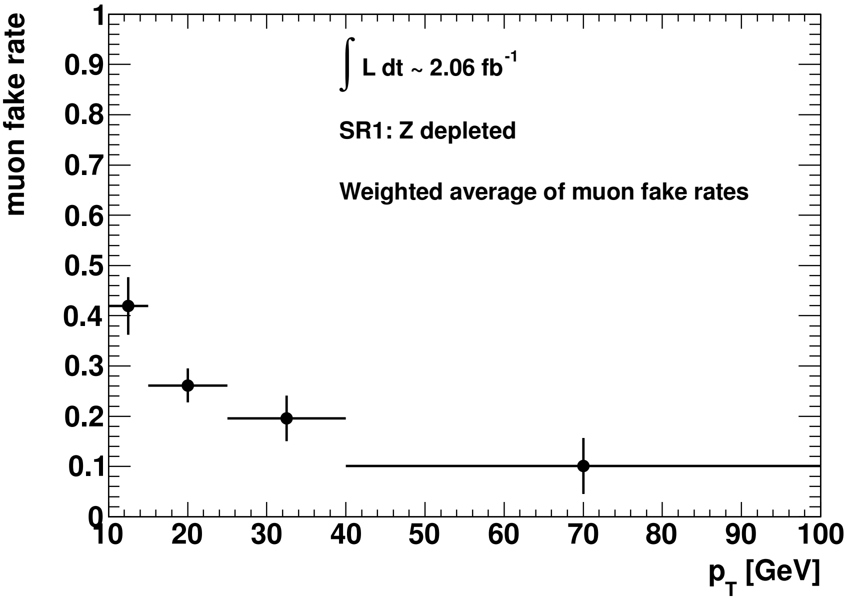

Figure 5.16: *Final fake rates of muons in SR1.*

5.7 Systematic Uncertainty on the Lepton Isolation

The mechanism for the determination of the reducible SM background, i.e. the matrix method described in Sections 5.3 and 5.4, deployed in this analysis relies heavily on the isolation properties of the leptons. Therefore a study of the systematic uncertainty related to the lepton isolation is performed on a data sample of $\int L dt = 1.04\,\text{fb}^{-1}$ of integrated luminosity taken in 2011 with the ATLAS detector.

The electron isolation requirements studied here are the spatial separation of electrons and jets in a cone of $\Delta R(\text{e},\text{jet}) < 0.4$ as well as the relative track isolation $p_{\text{T}}cone20/p_{\text{T}} < 0.1$. The efficiency of the isolation requirements are determined from data using a tag-and-probe method on $Z \to e^+e^-$ events as already described in Section 5.5. The uncertainty is calculated by comparing the efficiency measured in data with the efficiency obtained from a $Z \to e^+e^-$ MC simulated sample, using the same sample as for the rest of the analysis. In this implementation of the tag-and-probe method the electrons are baseline electrons, where the requirement of a spatial separation with jets is dropped and also studied. As before, tag electrons are required to be signal electrons matched to the appropriate trigger. The probability of the second electron (‘probe’ electron) to fulfill the signal electron requirement is measured by counting of events and represents the efficiency:

$$\varepsilon_{Iso} = \frac{N_{probe}^{signal}}{N_{probe}^{total}}. \tag{5.9}$$

The efficiency determined in ten bins of the pseudorapidity is shown in Figure 5.17(a). The agreement between data and the simulation is very good except for the ‘crack regions’ ($1.37 < |\eta| < 1.52$) where the simulation overestimates the efficiency compared to the data. Figure 5.17(b) shows the efficiency as a function of the number of jets. Supersymmetric events can contain a high number of jets as was discussed in the theoretical introduction in Section 2.2. Therefore it is important to ensure that the isolation works well also for high jet multiplicities. This is also studied by comparing the distributions of the spatial separation of electrons and the closest jet ($\Delta R(\text{e},\text{jet})$) and by comparing the distributions of the relative track isolation ($p_{\text{T}}cone20/p_{\text{T}}$) of different processes in MC simulated samples. The results for $Z \to e^+e^-$ events are compared to $t\bar{t}$ events and an official ATLAS SUSY benchmark point SU4[1] in Figures 5.18 and 5.19. The distributions of $\Delta R(\text{e},\text{jet})$ depend on the number of jets, but for a given number of jets very similar results are seen for the three processes, meaning that the spatial isolation of electrons does not depend on the process but rather on the overall event topology. The distribution of the relative track isolation $p_{\text{T}}cone20/p_{\text{T}}$ of $t\bar{t}$ events generally extends to higher values than the distribution for $Z \to e^+e^-$ events, but the effect is only seen at the level of $< 1\%$. With

---

[1] SU4 is a point in the mSUGRA parameter plane with parameters $m_0 = 200\,\text{GeV}$, $m_{\frac{1}{2}} = 160\,\text{GeV}$, $A_0 = -400\,\text{GeV}$, $\tan\beta = 10$ and $\mu > 0$. It has already been excluded by ATLAS and is shown here only for illustrative purposes.

increasing jet multiplicity the two distributions become more and more similar, meaning that while this distribution depends on the process, it does so only to an extent that is negligible.
Finally, the systematic uncertainty $\frac{\Delta\varepsilon}{\varepsilon}$ on the isolation requirement is obtained by calculating the relative difference between the efficiency measured in data and the efficiency obtained from MC simulated samples. The result obtained from the tag-and-probe method is smaller than 1% in the full range of pseudorapidity except for the crack region, where the uncertainty on the efficiency is $\sim 1\%$.
For the muons, the spatial separation from jets in a cone of $\Delta R(\mathrm{e},\mathrm{jet}) < 0.4$ as well as the absolute track isolation $p_{\mathrm{T}}cone20/p_{\mathrm{T}} < 1.8\,\mathrm{GeV}$ are studied using the same method as for the electrons. Figure 5.20 shows the efficiency as a function of the pseudorapidity (Figure 5.20(a)) and as a function of the number of jets in the event (Figure 5.20(b)). With higher jet multiplicity the efficiency drops rather sharply, but the agreement between the prediction by the MC simulated sample and the data is still very good. The systematic uncertainty on the isolation requirement of muons obtained with this method is smaller than 1% in the full range of pseudorapidity.

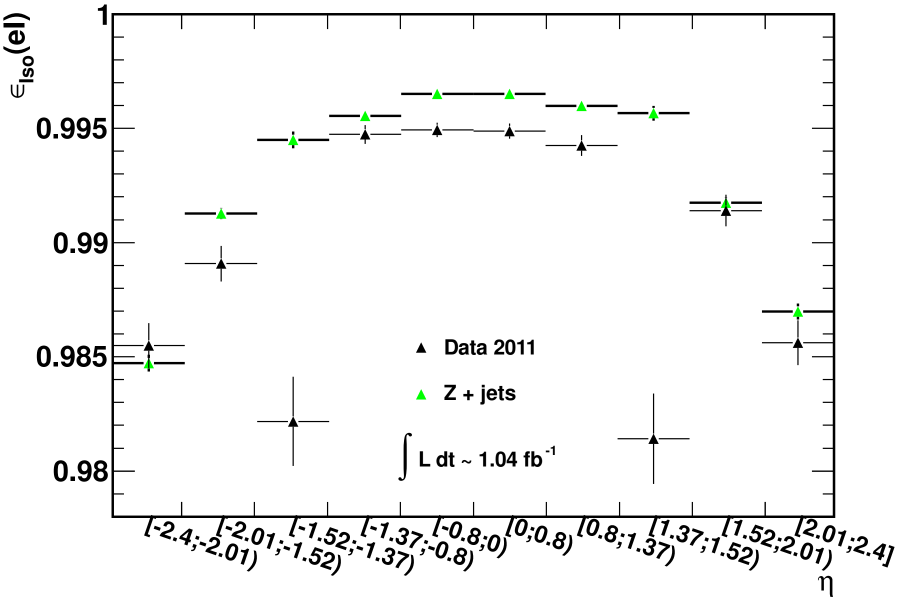

(a) Efficiency as a function of the pseudorapidity of the electrons.

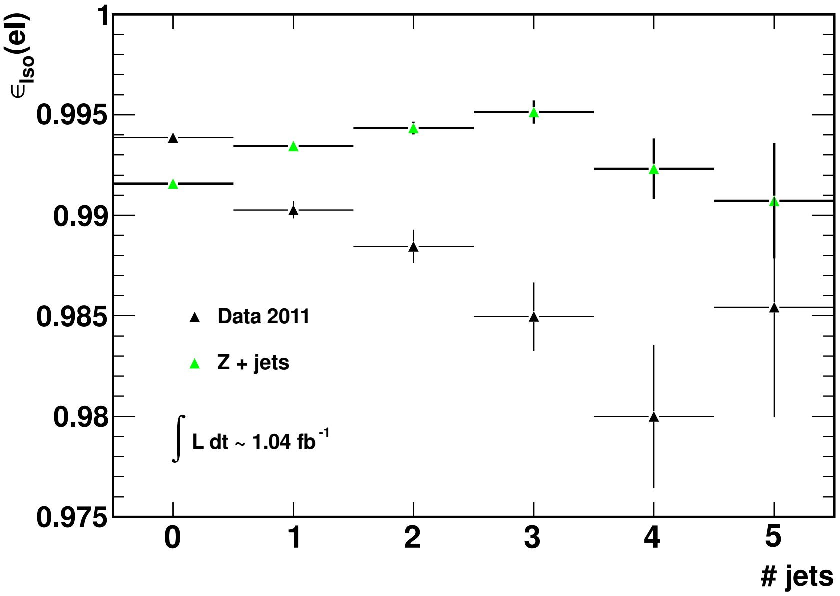

(b) Efficiency as a function of the number of jets.

Figure 5.17: *Efficiency of the isolation requirements of electrons in data and in Z + jets MC simulated samples.*

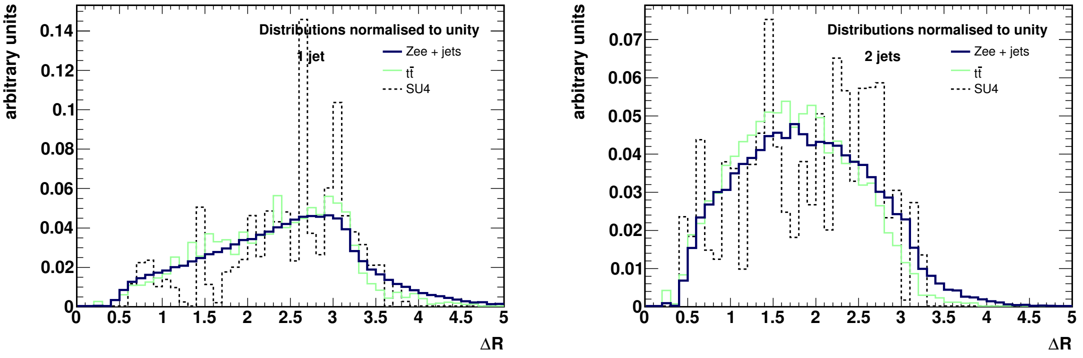

(a) $\Delta R(\mathrm{e},\mathrm{jet})$ in events with one jet.

(b) $\Delta R(\mathrm{e},\mathrm{jet})$ in events with two jets.

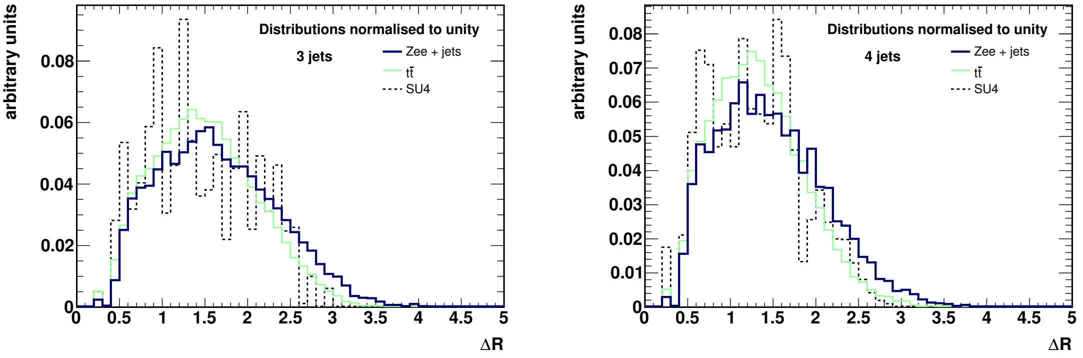

(c) $\Delta R(\mathrm{e},\mathrm{jet})$ in events with three jets.

(d) $\Delta R(\mathrm{e},\mathrm{jet})$ in events with four jets.

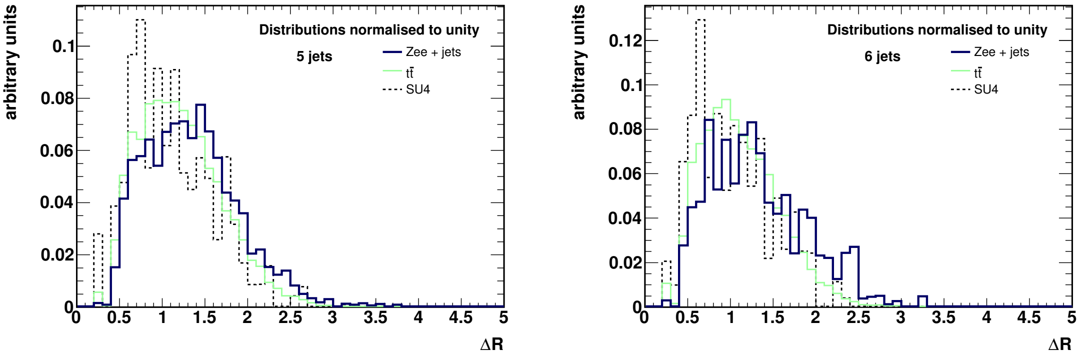

(e) $\Delta R(\mathrm{e},\mathrm{jet})$ in events with five jets.

(f) $\Delta R(\mathrm{e},\mathrm{jet})$ in events with six jets.

Figure 5.18: *Spatial separation* $\Delta R(\mathrm{e},\mathrm{jet})$ *between electrons and jets in three different MC simulated samples.*

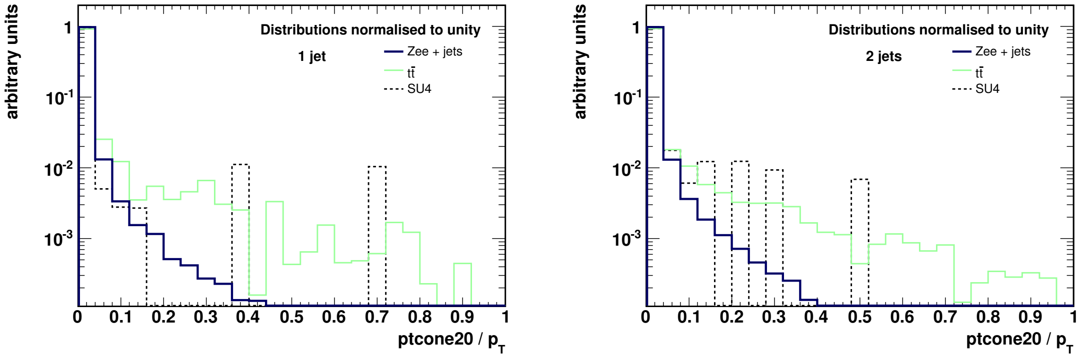

(a) $\Delta R(\mathrm{e},\mathrm{jet})$ in events with one jet.

(b) $\Delta R(\mathrm{e},\mathrm{jet})$ in events with two jets.

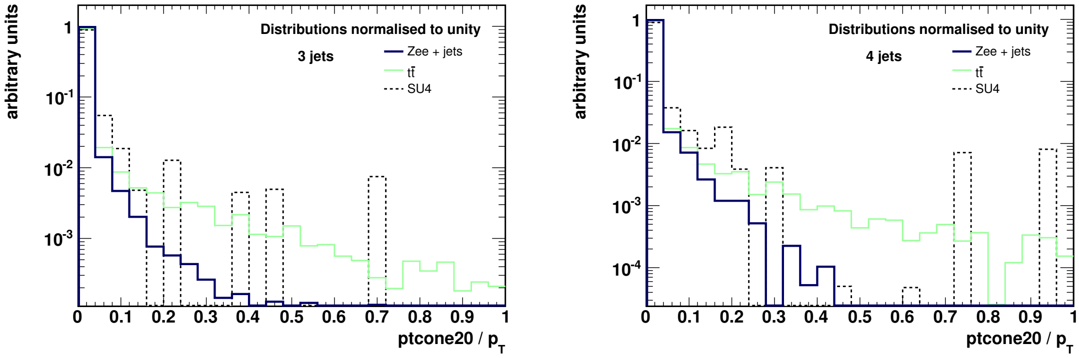

(c) $\Delta R(\mathrm{e},\mathrm{jet})$ in events with three jets.

(d) $\Delta R(\mathrm{e},\mathrm{jet})$ in events with four jets.

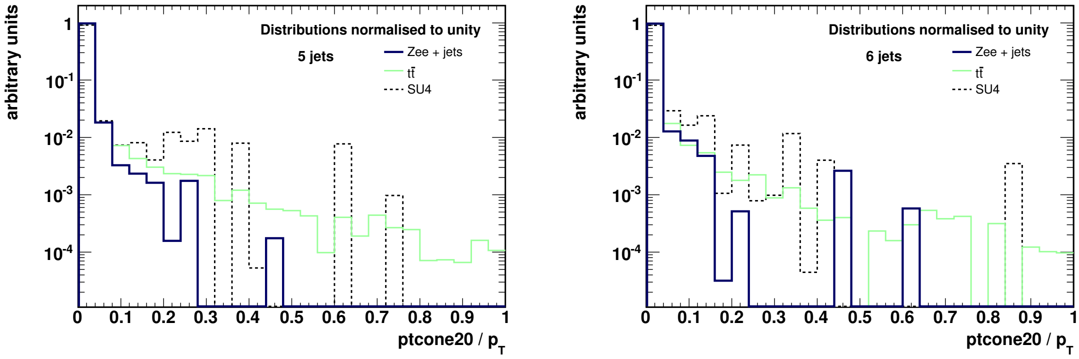

(e) $\Delta R(\mathrm{e},\mathrm{jet})$ in events with five jets.

(f) $\Delta R(\mathrm{e},\mathrm{jet})$ in events with six jets.

Figure 5.19: *Relative track isolation* $p_{\mathrm{T}}\mathit{cone}20/p_{\mathrm{T}}$ *of electrons in three different MC simulated samples.*

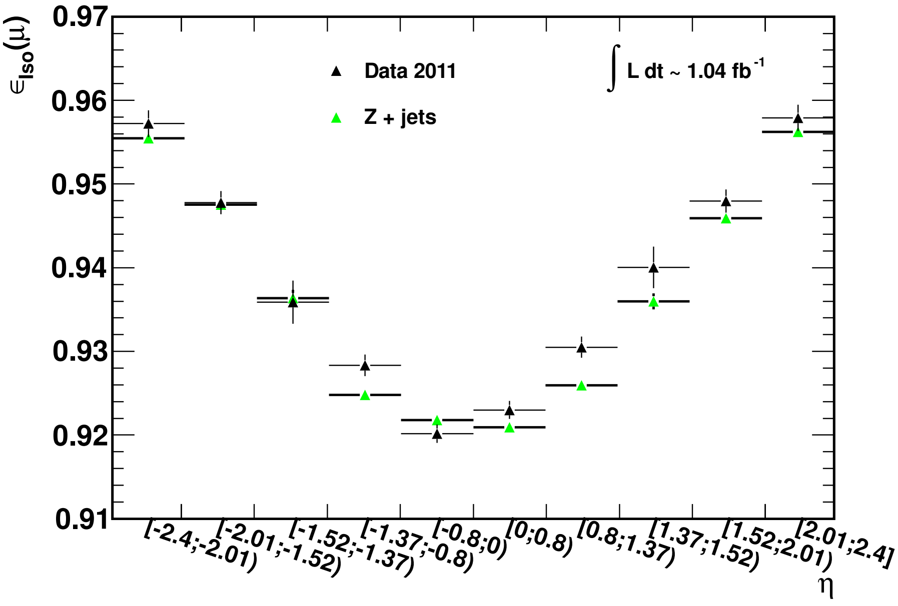

(a) Efficiency as a function of the pseudorapidity of the muons.

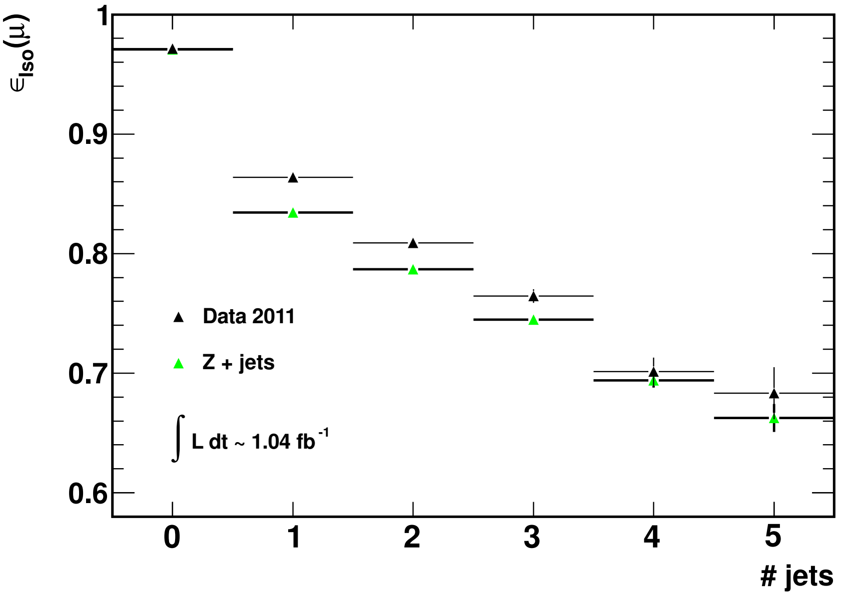

(b) Efficiency as a function of the number of jets.

Figure 5.20: *Efficiency of the isolation requirements of muons in data and in Z + jets MC simulated samples.*

6 Final Analysis Results

This chapter summarises the final results of the analysis, bringing together the work of this thesis and other aspects not discussed here. A summary of the analysis can be found in [45].

In the following, distributions of data and the SM prediction are shown. Some of the distributions include predictions for a SUSY reference point. This reference point is taken from the simplified model scenario and has the following parameters:

- $m_{\tilde{\chi}_1^\pm} = m_{\tilde{\chi}_2^0} = 150\,\text{GeV}$;
- $m_{\tilde{l}_L} = 100\,\text{GeV}$;
- $m_{\tilde{\chi}_1^0} = 50\,\text{GeV}$.

6.1 Final Data and MC Comparison

The event yields for the two signal regions SR1 and SR2 and the two control regions VR1 and VR2 (as defined in Section 4.9) are presented in Table 6.1. The numbers presented for the ZZ, WZ and $t\bar{t}+V$ backgrounds are taken from MC simulated samples, while the numbers for the reducible background are obtained with the matrix method described in Section 5.4 (and a small additional component due to virtual photons converting into muons [45]). The total background is the sum of these two contributions. The numbers quoted for the data are the observed numbers of events in the appropriate regions. The quoted uncertainties include statistical and systematic uncertainties.

The agreement between the SM prediction and the observed data in the control regions VR1 and VR2 is very good and is used to validate the background estimation approach used in the analysis. The observations in the signal regions are used to derive upper limits on the cross section of SUSY processes in the context of the pMSSM and the simplified model scenario introduced in Sections 2.2.4 and 2.2.5 and are discussed in Section 6.3.

Figure 6.1 shows the distributions of the missing transverse momentum in the two signal regions, while for the signal region SR1 Figures 6.2, 6.3 and 6.4 show the distributions of the transverse momenta of the three leptons and Figure 6.5 shows the distribution of the invariant mass of the SFOS lepton pair with an invariant mass closest to the nominal mass of the Z boson. The grey error band in the figures displayed around the red line representing the sum of all SM backgrounds comprises the statistical and systematic uncertainties, while the uncertainty shown for the data points is statistical only. All distributions show reasonable agreement between the data and the SM prediction. The distributions of the lepton transverse momenta for the signal region SR2 are included in the appendix (A.2) and also show reasonable agreement between the data and the SM prediction.

Table 6.1: *Expected number of events from SM processes and observed number of events in data in control regions VR1 and VR2 and in the two signal regions SR1 and SR2. The quoted uncertainties include statistical and systematic uncertainties [45].*

Selection	VR1	VR2	SR1	SR2
ZZ	6.7±1.8	0.03±0.04	0.7±0.2	3.4±0.9
WZ	61±15	0.4±0.2	11±3	58±14
$t\bar{t}+V$	1.4±0.6	0.7±0.6	0.4±0.3	2.7±2.1
Reducible Background	56±35	14±9	14±4	7.5±3.9
Total Background	125±38	15±9	26±5	72±15
Data	122	12	32	95

6.2 Systematic Uncertainties

The systematic uncertainty on the reducible component of the background is the dominant source of systematic uncertainty in SR1 with a value of 17%. The main contribution to this uncertainty is in the weighted average of fake rates. The effects considered are the dependence on the cross section, the renormalisation/factorisation scale and the PDF[1] (10-30%), the dependence on the missing transverse momentum (0.4-17%) and the uncertainty on the scale factors sf^i (10-50%). The systematic uncertainty on the irreducible background prediction is composed of a theoretical uncertainty on the MC simulation (20-25%), an uncertainty due to the limited number of MC simulated events (10%) and the uncertainties on jet energy scale and resolution, lepton energy scale and resolution, lepton identification efficiency, b-tagging efficiency and event quality selection (0.2-5%).

---

[1] Parton Distribution Function

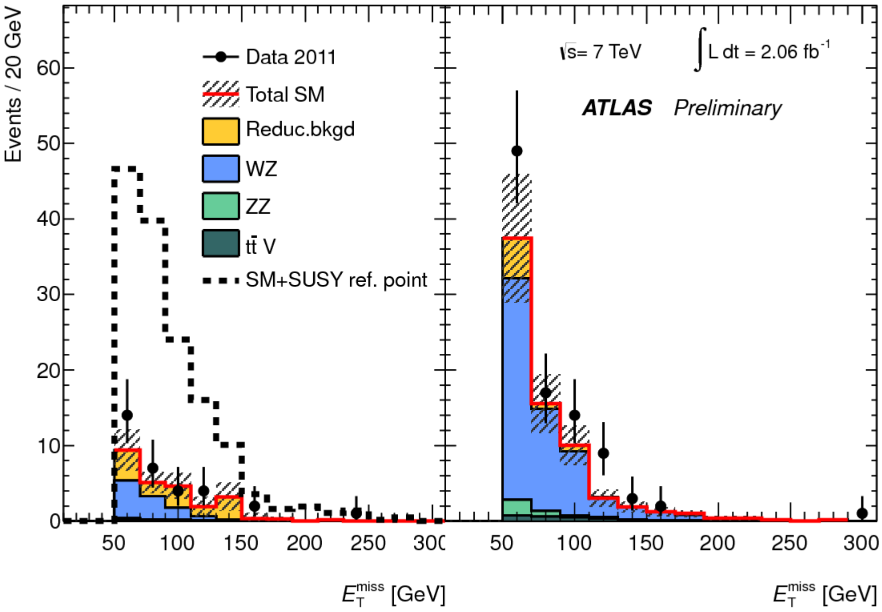

Figure 6.1: *Distribution of the missing transverse momentum* E_T^{miss} *in the signal regions SR1 (left) and SR2 (right) for the data and the SM prediction [45].*

Finally, an uncertainty of 3.7% [46] on the integrated luminosity is also taken into account.

The systematic uncertainties for SR2 are similar to those in SR1, except for a smaller uncertainty due to the limited number of MC simulated events (4%).

Regarding the systematic uncertainty on the MC simulated SUSY signal samples total uncertainties in the range 10-15% are obtained. These include the same experimental sources considered for the irreducible background processes as well as theoretical systematic uncertainties on the cross sections.

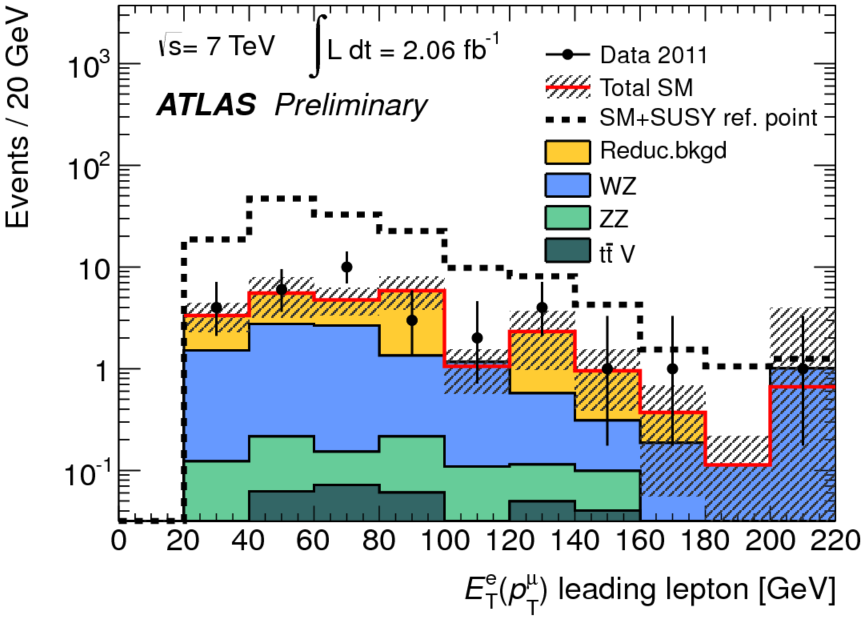

Figure 6.2: *Distribution of the transverse momentum of the leading lepton in signal region SR1 for the data and the SM prediction [45].*

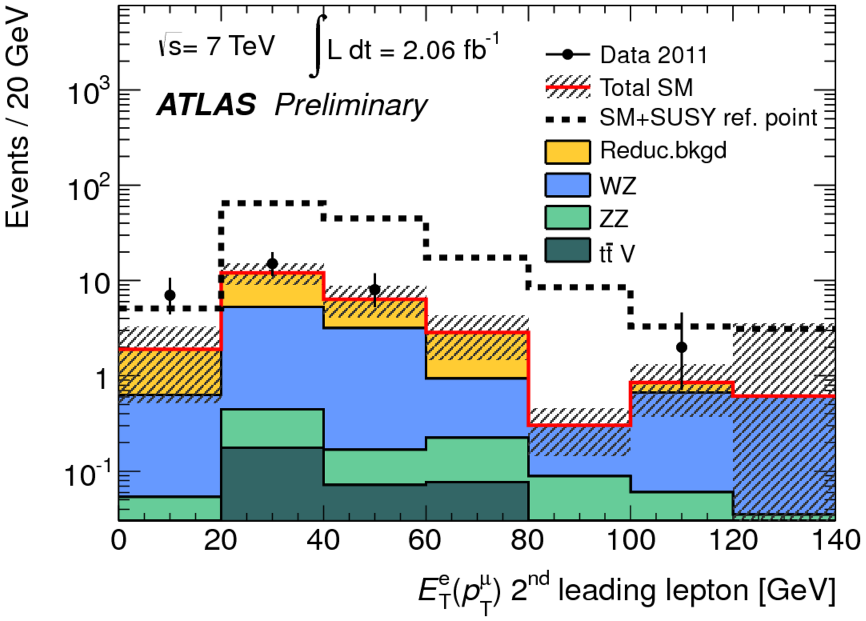

Figure 6.3: *Distribution of the transverse momentum of the second leading lepton in signal region SR1 for the data and the SM prediction [45].*

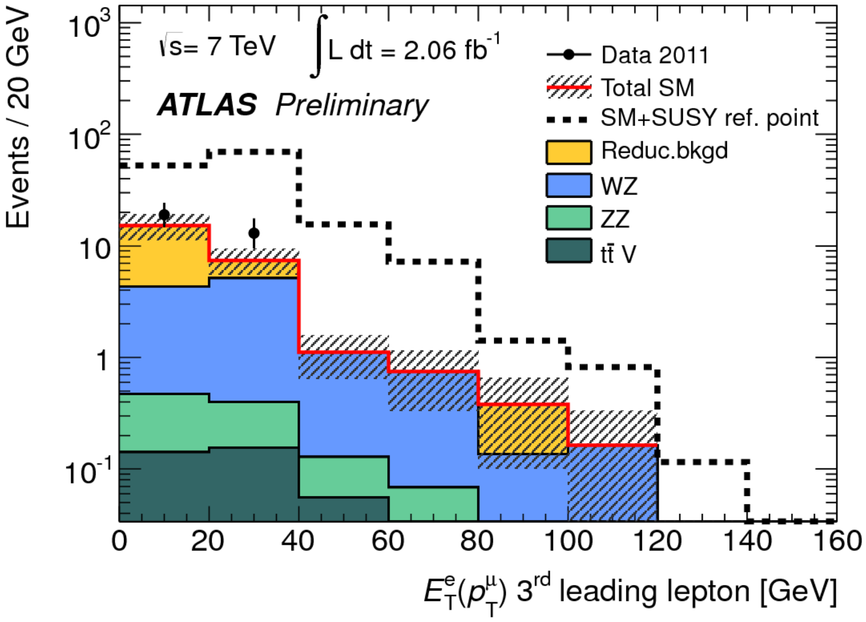

Figure 6.4: *Distribution of the transverse momentum of the third leading lepton in signal region SR1 for the data and the SM prediction [45].*

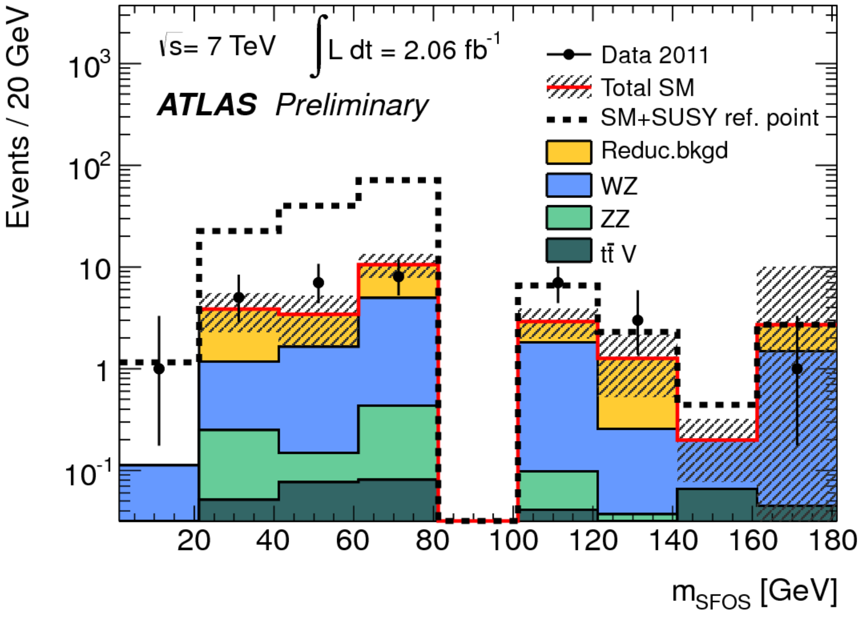

Figure 6.5: *Distribution of the invariant mass of the SFOS lepton pair with an invariant mass closest to the nominal Z boson mass in signal region SR1 for the data and the SM prediction [45].*

6.3 Interpretation of the Results

The results presented in Table 6.1 are interpreted in the context of the pMSSM and the simplified model scenario described in Sections 2.2.4 and 2.2.5, respectively.

No significant excess of events is found in the data compared to the SM expectation. The observed number of events in the two signal regions is analysed using the frequentist approach. The probability that the SM background fluctuates to the observed number of events or higher is calculated to 19% (SR1) and 10% (SR2), respectively. This allows to place an upper limit on the visible production cross section[2] of SUSY processes producing events with three leptons at 10.0 fb (SR1) and 26.1 fb (SR2) at 95% confidence level using the modified frequentist CL_s prescription [47]. This is slightly above the expected limits at 7.3 fb and 16.7 fb.

The limit from SR1 is interpreted in the pMSSM with the gaugino mass parameter M_1 set to $M_1 = 100\,\mathrm{GeV}$ and in the simplified model scenario. The results are depicted in Figure 6.6.

For the pMSSM (Figure 6.6(a)) the red line indicates the contour of the region excluded at 95% confidence level by the present analysis, which is also highlighted in blue. The orange area corresponds to the exclusion limit set by the LEP experiments on the mass of the lightest chargino, $m_{\tilde{\chi}_1^\pm} > 103.5\,\mathrm{GeV}$ [14]. The two different types of grey lines are the curves of constant mass of the lightest neutralino (steeper slope) and the lightest chargino, respectively. For $M_1 = 100\,\mathrm{GeV}$, values of $\mu < 150\,\mathrm{GeV}$ are excluded as well as values of $160\,\mathrm{GeV} < M_2 < 230\,\mathrm{GeV}$.

In the simplified model scenario, Figure 6.6(b) shows two different exclusion limits. As for the pMSSM the red line indicates the contour of the region excluded at 95% confidence level by the present analysis. As indicated in the figure and discussed in Section 2.2.5, the lightest chargino and the next-to-lightest neutralino are mass degenerate, while the lightest neutralino is the LSP. For chargino masses up to 250 GeV LSP masses up to 170 GeV are excluded, while for large mass differences between the lightest chargino and the LSP chargino masses up to 300 GeV are excluded at 95% confidence level. The second limit shown in this figure is illustrated in the colour code. For each point in the parameter space the upper limit on the production cross section that can be excluded at 95% confidence level is shown.

The mass limits set in the simplified model cannot be directly translated into limits in the pMSSM. This is due to setting the masses of the sleptons and the sneutrinos to the same value. In the pMSSM the mass of the sneutrino is smaller than the mass of the left-handed sleptons, and thus the branching fractions for the decays into the two sparticles are not the same.

---

[2] The visible production cross section means the product of the cross section times the branching ratio times the acceptance.

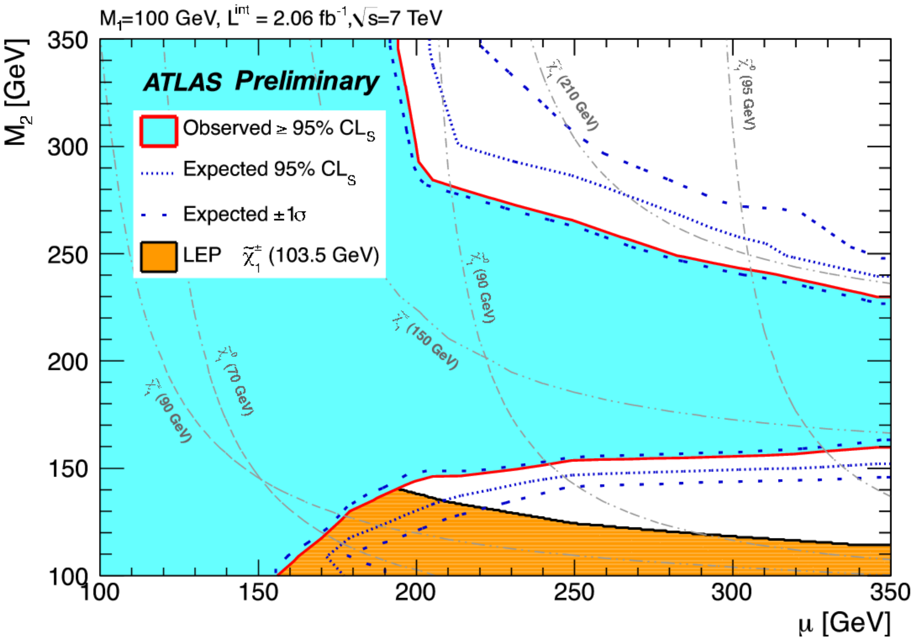

(a) Limit in the pMSSM.

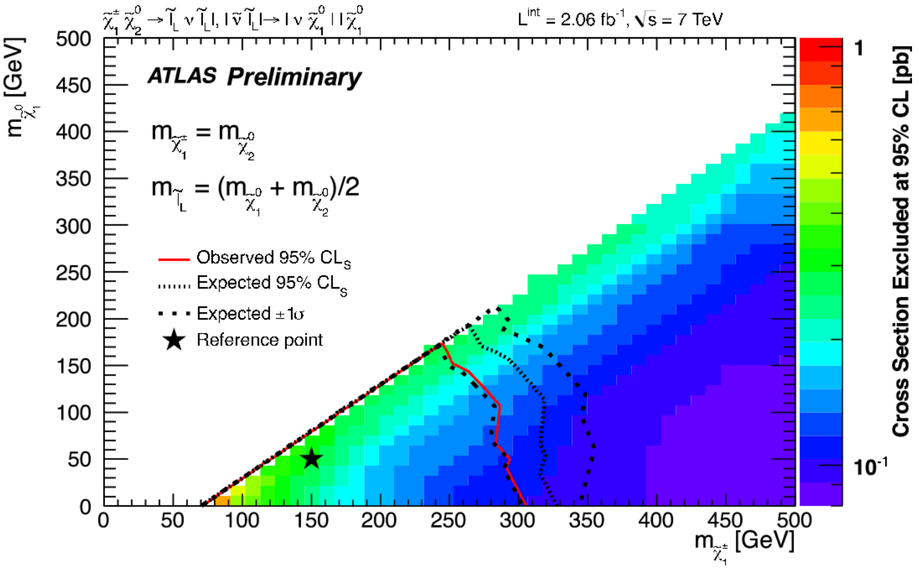

(b) Limits in the simplified model scenario.

Figure 6.6: *Observed and expected 95% confidence level limit contours for chargino and neutralino production in the pMSSM (a) and the simplified model scenario (b). For the simplified model scenario the upper limit on the production cross section at 95% confidence level is also shown. The discreteness of the simulation of the signal grids is taken into account via interpolation. [45].*

7 Summary and Conclusions

A search for Supersymmetry in events with three leptons (electrons or muons) and missing transverse momentum with the ATLAS detector at the LHC in a data sample with an integrated luminosity $\int L dt = 2.06\,\mathrm{fb}^{-1}$ is presented. The null result obtained in two distinct signal regions is interpreted in the context of a phenomenological Minimal Supersymmetric Standard Model (pMSSM) and a simplified supersymmetric model.
The events selected from data for the analysis are required to be taken with the ATLAS detector fully operational. At least one well reconstructed lepton in the efficiency plateau region in transverse momentum of the corresponding single lepton trigger is required to be close to a trigger object having fired the trigger. Leptons are considered for the analysis, if they fulfill a set of quality criteria, fall into the pseudorapidity range $|\eta| < 2.47$ (electrons) or $|\eta| < 2.4$ (muons) and have a transverse momentum $p_{\mathrm{T}} > 10\,\mathrm{GeV}$. The leptons are also required to be isolated through track-based isolation criteria and through a spatial separation from jets. In order to suppress the decays of low-mass particles (e.g. J/Ψ), lepton pairs of same flavour and opposite charge sign (SFOS) with an invariant mass $m_{\mathrm{ll}} < 20\,\mathrm{GeV}$ are discarded from the events. Events are then required to contain exactly three leptons, among these at least one SFOS pair. Two signal regions are defined. In the first signal region SR1 a missing transverse momentum $\not{E}_{\mathrm{T}} > 50\,\mathrm{GeV}$ is required, the invariant mass of any SFOS lepton pair must not be within $10\,\mathrm{GeV}$ of the nominal mass of the Z boson ($m_Z = 91.2\,\mathrm{GeV}$ is used) and events containing jets tagged as originating from a b quark are rejected. This signal region is also denoted Z-depleted region, as signatures with Z bosons are suppressed. The second signal region SR2 is defined by the requirement of a Z boson (i.e. at least one SFOS lepton pair with an invariant mass within $10\,\mathrm{GeV}$ of the nominal Z boson mass) and a cut on the missing transverse momentum $\not{E}_{\mathrm{T}} > 50\,\mathrm{GeV}$ and is denoted Z-enriched signal region.
Applying the selection cuts to a variety of Monte Carlo (MC) simulated samples, the dominant contributions to the Standard Model (SM) background in the signal regions are identified. In SR1 these are the $t\bar{t}$ and the WZ diboson production processes, with about equal amounts. In SR2 the WZ diboson production process largely dominates the SM background.
The SM background processes contributing to the signal regions are classified into two distinct categories. The first category, the irreducible background processes, comprises

all SM processes that lead to final states with three prompt and isolated ('real') leptons. For the description of these background processes the analysis relies on the respective MC simulated samples. The second category, the reducible background processes, encompasses all SM processes, where at least one of the leptons is a 'fake' lepton, with a fake lepton being either a non-prompt lepton, e.g. from the semileptonic decay of a b quark, or an object misidentified as a lepton. These background processes are described by the semi data-driven matrix method. This method relies on the different characteristics of real and fake leptons with respect to two different sets of isolation criteria and on the assumption that the numbers of leptons with tighter or looser isolation depend linearly on the number of real and fake leptons. The coefficients of the linear expressions are the efficiency of loose real leptons to fulfill the tighter requirements and the probability of loose fake leptons to fulfill the tighter requirements ('fake rate').

A study of the sources of the leptons on MC simulated samples using the available information from the generation and simulation of the events, reveals that the main source of fake leptons is semileptonic decays of b or c quarks for electrons and muons, while for electrons converted photons are also a non-negligible source. The majority of leptons are nevertheless real leptons in both signal regions.

The measurement of fake rates for the present implementation of the matrix method from data presents major challenges. A study on MC simulated samples shows that the kinematic properties of fake muons from the semileptonic decay of a b quark are different for $t\bar{t}$ events, Z production in association with jets and $b\bar{b}$ events. Looking at the fake rate as a property of the original b quark the fake rates become similar. It is thus inferred that the fake rates of muons are not universal across processes and cannot be determined from data.

The fake rates for the present implementation of the matrix method are therefore determined from MC simulated samples, calculating fake rates for each process separately and then weighting the different fake rates according to the contribution of the specific process to the signal or control region of interest. For any further details on the calculation the reader is referred to Section 5.6.2. The final fake rate for electrons in SR1 gives values between $\sim 20\%$ and $\sim 6\%$ depending on the transverse momentum and the pseudorapidity. The fake rate of muons is only parameterised in the transverse momentum and results in values between $\sim 42\%$ and $\sim 10\%$ in SR1.

Since the matrix method and the fake rates rely heavily on the isolation properties of the leptons, the systematic uncertainty associated with these is studied in detail. Using $Z \to e^+e^-$ and $Z \to \mu^+\mu^-$ events for electrons and muons, respectively, and also ensuring to consider event topologies containing a high hadronic activity, that can be present in certain SUSY scenarios, a negligible systematic uncertainty of $\sim 1\%$ is measured.

Applying all selection criteria, an observation of 32 events with a SM expectation of 26 ± 5 events in SR1 and 95 events with a SM expectation of 72 ± 15 events in SR2 is made. In SR1, the contribution to the SM prediction from reducible backgrounds is 14 ± 4 events, while in SR2 this contribution is 7.5 ± 3.5 events. These observations are interpreted in the pMSSM and in a simplified model scenario. The probability that the background fluctuates to the observed number of events or higher is calculated to 19% (SR1) and 10% (SR2), respectively. This allows to place an upper limit on the visible production cross section of SUSY processes at 10.0 fb (SR1) and 26.1 fb (SR2) at 95% confidence level. In the pMSSM scenario exclusion limits on the parameters of the theory are set. In the context of the simplified model chargino masses up to 300 GeV are excluded at 95% confidence level for large mass differences to the lightest supersymmetric particle. It has to be noted that due to the assumptions of the simplified model this limit on the chargino mass cannot be directly transferred to other SUSY models.

A Appendix

A.1 Details of the MC Simulation

Table A.1: *Overview of the diboson MC simulated samples.* σ *denotes the cross section, while the k-factor is the factor applied to scale the cross section from leading order to next-to-leading order (where applicable). For the processes simulated with HERWIG [27] the cross section is calculated to next-to-leading order, while for the MADGRAPH [31] processes the cross section is calculated to leading order. The integrated luminosities given correspond to the total statistics of the samples.*

Diboson processes			
Process	Generator	$\sigma \times$ k-factor [pb]	integrated luminosity [fb^{-1}]
ZZ	HERWIG	6.21	190.4
WZ		19.1	42.4
W^+W^-		43.8	146.6
$W^\pm W^\pm$	MADGRAPH	0.22	433.0
$W^+\gamma\,(e\nu)$		27.97	1.8
$W^+\gamma\,(\mu\nu)$		27.94	1.8
$W^+\gamma\,(\tau\nu)$		25.42	11.0
$W^-\gamma\,(e\nu)$		18.59	2.7
$W^-\gamma\,(\mu\nu)$		18.59	2.7
$W^-\gamma\,(\tau\nu)$		16.86	17.1
$Z\gamma\,(ee)$		10.02	1.8
$Z\gamma\,(\mu\mu)$		10.02	1.8
$Z\gamma\,(\tau\tau)$		9.76	11.0

Table A.2: *Overview of the top quark + vector boson MC simulated samples. σ denotes the cross section, while the k-factor is the factor applied to scale the cross section from leading order to next-to-leading order. The integrated luminosities given correspond to the total statistics of the samples.*

Top + boson processes			
Process	Generator	$\sigma\times$ k-factor [pb]	integrated luminosity [fb^{-1}]
$t\bar{t}W$	MADGRAPH	0.156	617.7
$t\bar{t}W$ + jet		0.104	920.7
$t\bar{t}Z$		0.13	804.1
$t\bar{t}Z$ + jet		0.104	941.6
$t\bar{t}WW$		0.0013	61524.9

Table A.3: *Overview of the $t\bar{t}$ and single top quark MC simulated samples. σ denotes the cross section, while the k-factor is the factor applied to scale the cross section from leading order to next-to-next-to-leading order. The integrated luminosities given correspond to the total statistics of the samples.*

$t\bar{t}$ and single top quark processes			
Process	Generator	$\sigma\times$ k-factor [pb]	integrated luminosity [fb^{-1}]
$t\bar{t}$ not all-hadronic	MC@NLO [28]	89.36	129.49
t-channel $e\nu$		7.12	24.95
t-channel $\mu\nu$		7.12	24.93
t-channel $\tau\nu$		7.10	24.97
s-channel $e\nu$		0.47	540.04
s-channel $\mu\nu$		0.47	539.50
s-channel $\tau\nu$		0.47	539.67
Wt		14.59	54.65

Table A.4: *Overview of the Z + jets and Zbb + jets MC simulated samples. σ denotes the cross section, while the k-factor is the factor applied to scale the cross section from leading order to next-to-next-to-leading order. The integrated luminosities given correspond to the total statistics of the samples. NpX ($X = 0 \ldots 5$) in the name of the process refers to the number of additional partons in the final state.*

Z + jets and Zbb + jets processes				
Process		Generator	$\sigma \times$ k-factor [pb]	integrated luminosity [fb^{-1}]
Z	ee + Np0	ALPGEN [32]	835.4	7.9
	ee + Np1		168.0	7.9
	ee + Np2		50.7	8.0
	ee + Np3		14.0	7.9
	ee + Np4		3.6	8.3
	ee + Np5		1.0	8.7
	$\mu\mu$ + Np0		835.9	7.9
	$\mu\mu$ + Np1		167.7	8.0
	$\mu\mu$ + Np2		50.4	8.0
	$\mu\mu$ + Np3		14.0	7.9
	$\mu\mu$ + Np4		3.4	8.7
	$\mu\mu$ + Np5		1.0	10.4
	$\tau\tau$ + Np0		835.5	7.9
	$\tau\tau$ + Np1		168.5	7.9
	$\tau\tau$ + Np2		50.5	8.0
	$\tau\tau$ + Np3		14.1	7.8
	$\tau\tau$ + Np4		3.5	8.6
	$\tau\tau$ + Np5		1.0	10.4
Zbb	ee + Np0	ALPGEN	11.5	13.0
	ee + Np1		4.3	23.0
	ee + Np2		1.5	25.0
	ee + Np3		0.7	14.6
	$\mu\mu$ + Np0		11.5	13.1
	$\mu\mu$ + Np1		4.3	23.1
	$\mu\mu$ + Np2		1.5	25.7
	$\mu\mu$ + Np3		0.7	14.6
	$\tau\tau$ + Np0		11.5	13.0
	$\tau\tau$ + Np1		4.3	22.9
	$\tau\tau$ + Np2		1.5	25.7
	$\tau\tau$ + Np3		0.7	13.2

Table A.5: *Overview of the W + jets, Wc + jets, Wcc + jets and Wbb + jets MC simulated samples. σ denotes the cross section, while the k-factor is the factor applied to scale the cross section from leading order to next-to-next-to-leading order. The integrated luminosities given correspond to the total statistics of the samples. NpX ($X = 0 \dots 5$) in the name of the process refers to the number of additional partons in the final state.*

W + jets, Wc + jets, Wcc + jets and Wbb + jets processes				
Process		Generator	$\sigma \times$ k-factor [pb]	integrated luminosity [fb^{-1}]
W	$e\nu$ + Np0	ALPGEN	8305.9	0.4
	$e\nu$ + Np1		1565.2	0.4
	$e\nu$ + Np2		454.0	8.3
	$e\nu$ + Np3		121.7	8.3
	$e\nu$ + Np4		31.0	8.1
	$e\nu$ + Np5		8.4	8.3
	$\mu\nu$ + Np0		8303.5	0.4
	$\mu\nu$ + Np1		1565.0	0.4
	$\mu\nu$ + Np2		453.4	8.3
	$\mu\nu$ + Np3		122.3	8.3
	$\mu\nu$ + Np4		30.9	8.3
	$\mu\nu$ + Np5		8.3	8.4
	$\tau\nu$ + Np0		8302.3	0.4
	$\tau\nu$ + Np1		1563.8	0.4
	$\tau\nu$ + Np2		453.8	8.3
	$\tau\nu$ + Np3		121.8	8.3
	$\tau\nu$ + Np4		30.8	8.1
	$\tau\nu$ + Np5		8.5	7.5
Wc	Np0	ALPGEN	518	1.6
	Np1		192	1.7
	Np2		51	1.7
	Np3		12	1.7
Wcc	Np0	ALPGEN	153	1.7
	Np1		124	1.6
	Np2		62	1.7
	Np3		20	1.7
Wbb	Np0	ALPGEN	4.0	1.6
	Np1		3.2	1.7
	Np2		1.7	1.8
	Np3		0.8	1.9

***Table A.6:** Overview of the Drell-Yan MC simulated samples. σ denotes the cross section, while the k-factor is the factor applied to scale the cross section from leading order to next-to-next-to-leading order. The integrated luminosities given correspond to the total statistics of the samples. NpX ($X = 0 \ldots 5$) in the name of the process refers to the number of additional partons in the final state.*

Drell-Yan processes				
Process		Generator	$\sigma \times$ k-factor [pb]	integrated luminosity [fb^{-1}]
DrellYan	ee + Np0	ALPGEN	3819.0	0.3
	ee + Np1		106.2	2.8
	ee + Np2		51.8	9.7
	ee + Np3		10.5	14.3
	ee + Np4		2.3	17.3
	ee + Np5		0.6	17.4
	$\mu\mu$ + Np0		3818.6	0.3
	$\mu\mu$ + Np1		106.1	2.8
	$\mu\mu$ + Np2		51.8	9.7
	$\mu\mu$ + Np3		10.5	14.3
	$\mu\mu$ + Np4		2.3	17.3
	$\mu\mu$ + Np5		0.6	17.4
	$\tau\tau$ + Np0		3818.9	0.3
	$\tau\tau$ + Np1		106.2	2.8
	$\tau\tau$ + Np2		51.8	9.6
	$\tau\tau$ + Np3		10.5	14.4
	$\tau\tau$ + Np4		2.3	17.3
	$\tau\tau$ + Np5		0.6	17.4

***Table A.7:** Overview of the $b\bar{b}$ MC simulated samples. σ denotes the cross section at leading order. The integrated luminosities given correspond to the total statistics of the samples.*

$b\bar{b}$ processes			
Process	Generator	σ [pb]	integrated luminosity [fb^{-1}]
$b\bar{b}$ ($\mu\mu$X, $p_{\mathrm{T}}^{\mu} > 10\,\mathrm{GeV}$)	PYTHIA [29]	2150	0.2
$b\bar{b}$ (μeX, $p_{\mathrm{T}}^{\mu,e} > 10\,\mathrm{GeV}$)		3820	0.2
$b\bar{b}$ (eeX, $p_{\mathrm{T}}^{e} > 10\,\mathrm{GeV}$)		1086	0.2

A.2 Additional Plots

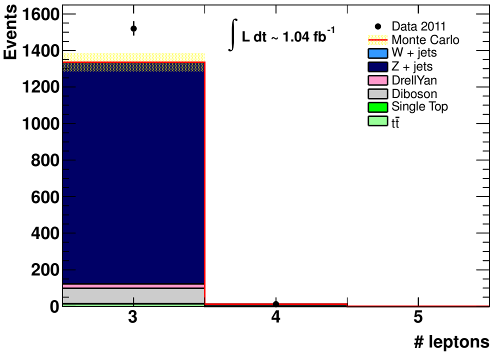

Figure A.1: *Number of leptons in the control region CR1. The red line represents the sum of all SM background processes. The yellow area around the red line represents the uncertainty. All uncertainties are statistical only.*

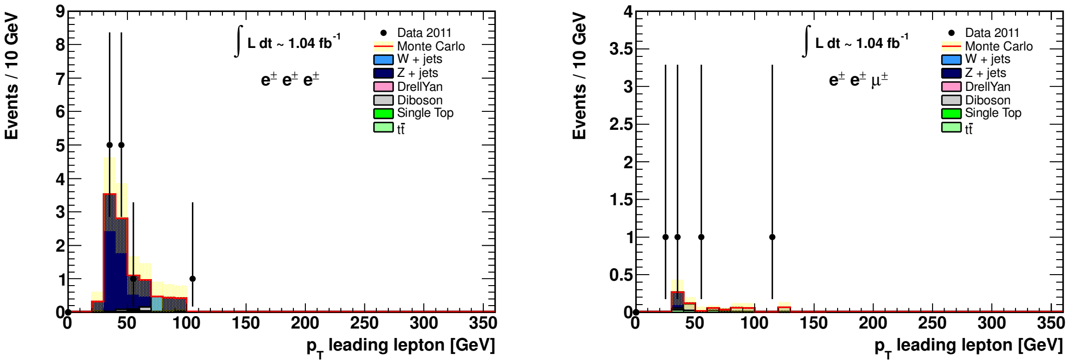

(a) $e^{\pm}e^{\pm}e^{\pm}$ (b) $e^{\pm}e^{\pm}\mu^{\pm}$

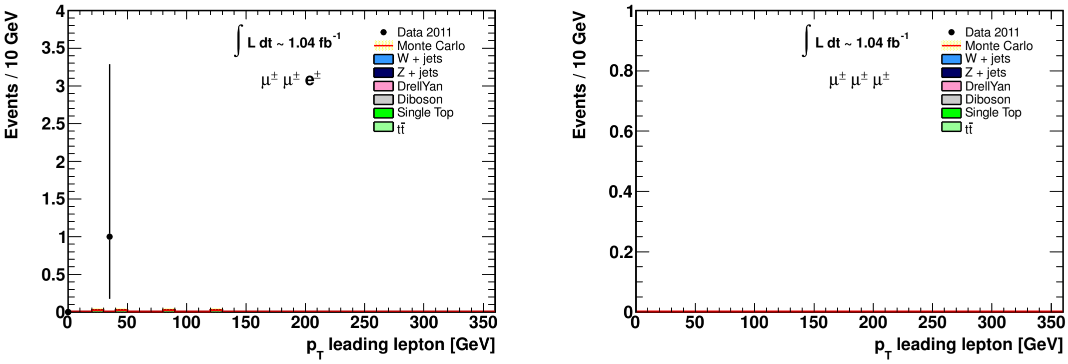

(c) $\mu^{\pm}\mu^{\pm}e^{\pm}$ (d) $\mu^{\pm}\mu^{\pm}\mu^{\pm}$

Figure A.2: *Transverse momentum of the leading lepton in channels with same sign leptons in the control region CR1. The red line represents the sum of all SM background processes. The yellow area around the red line represents the uncertainty. All uncertainties are statistical only.*

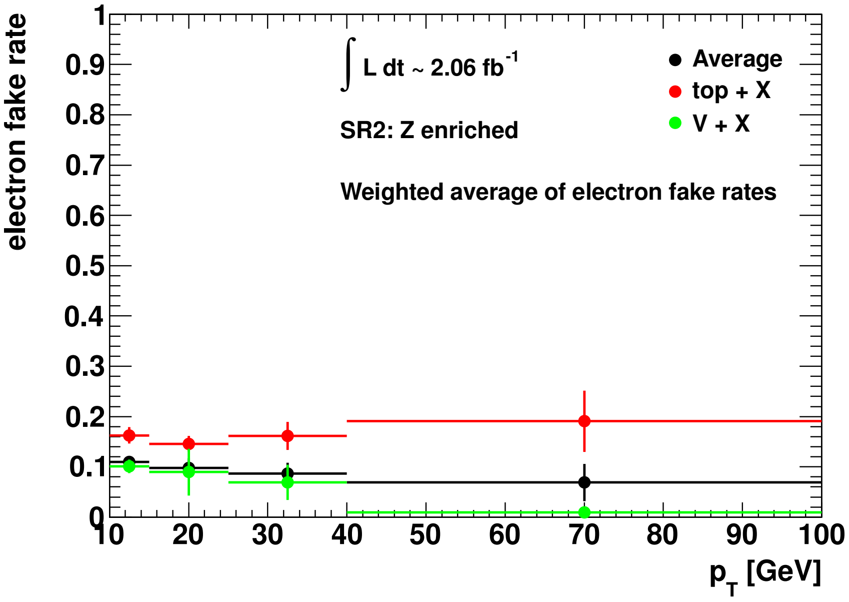

(a) Final electron fake rate

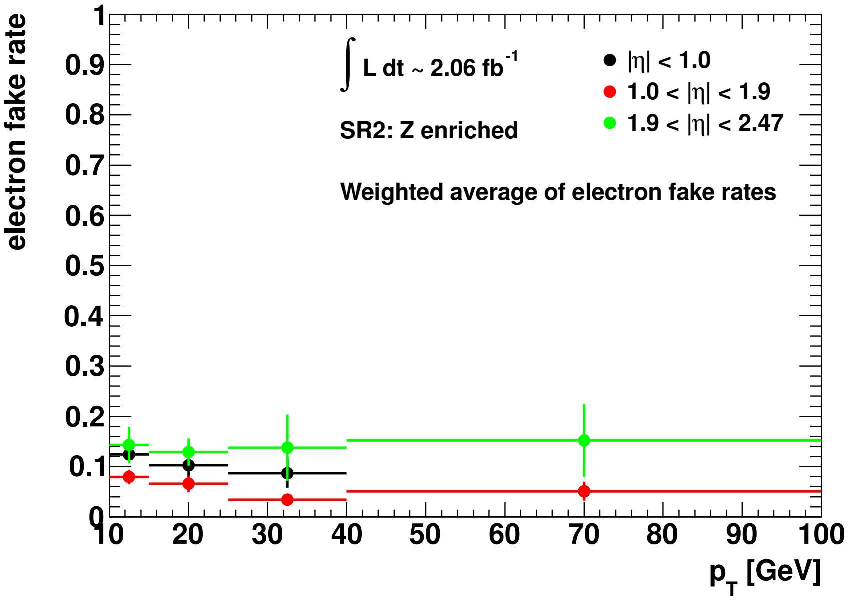

(b) Final electron fake rate in three bins of pseudorapidity

Figure A.3: *Final fake rates of electrons in SR2. Both the final average and individual fake rates for the two processes are shown in (a).*

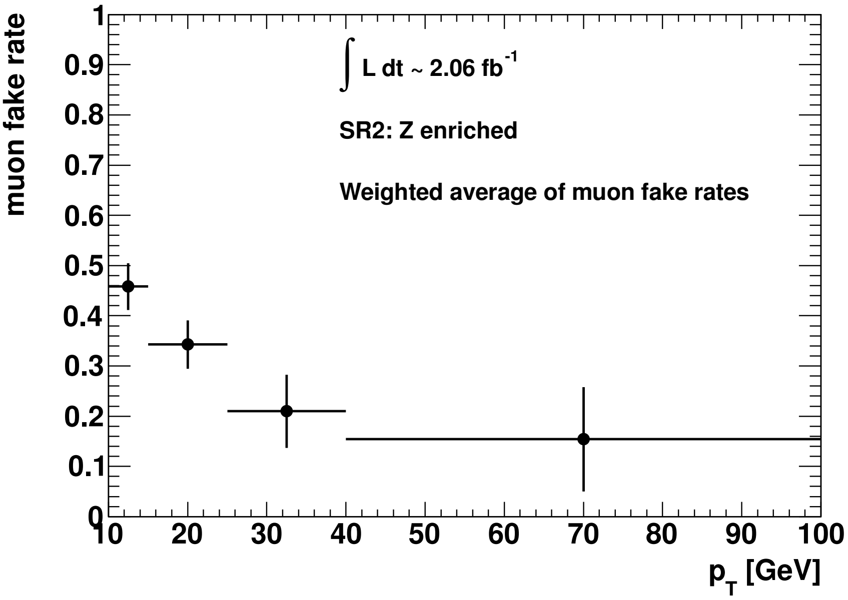

Figure A.4: *Final fake rates of muons in SR2.*

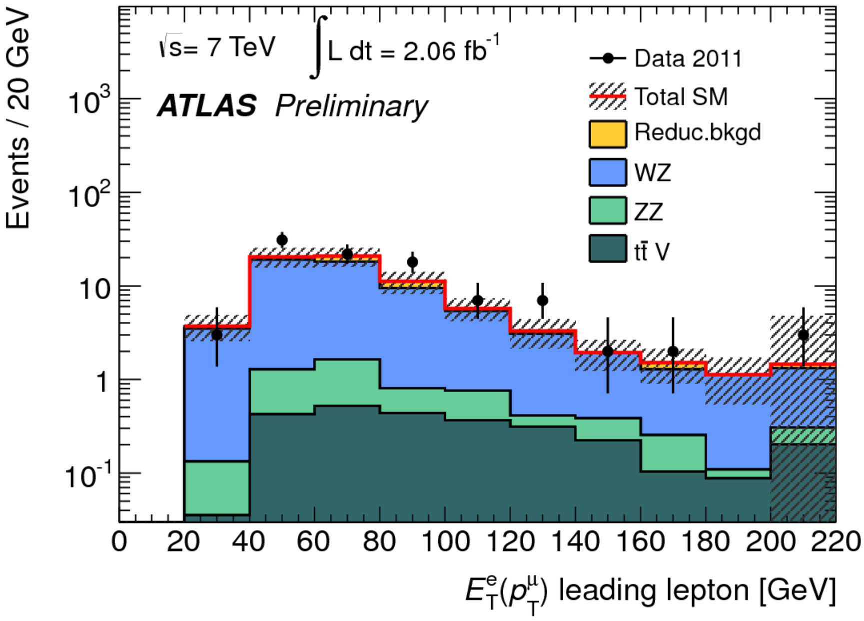

Figure A.5: *Distribution of the transverse momentum of the leading lepton in signal region SR2 for the data and the SM prediction [45].*

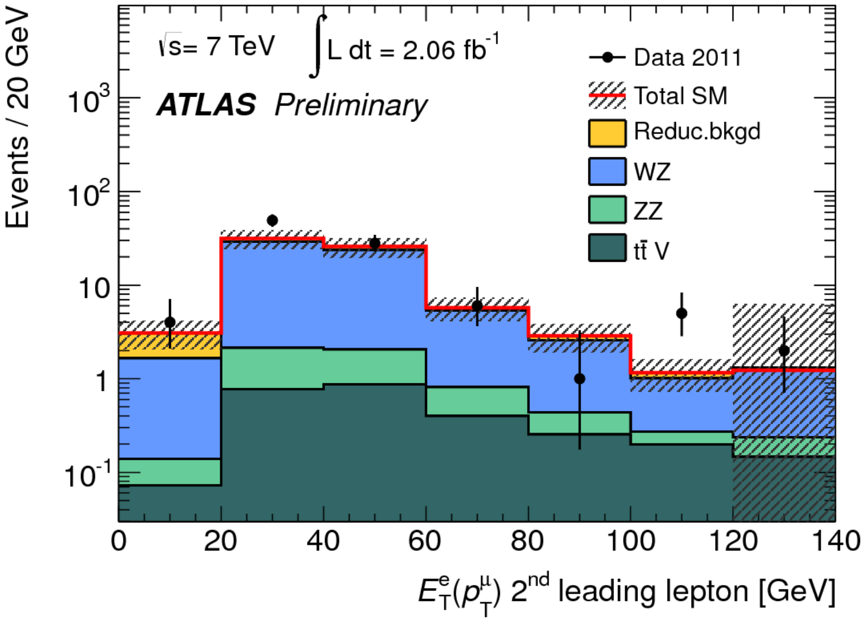

Figure A.6: *Distribution of the transverse momentum of the second leading lepton in signal region SR2 for the data and the SM prediction [45].*

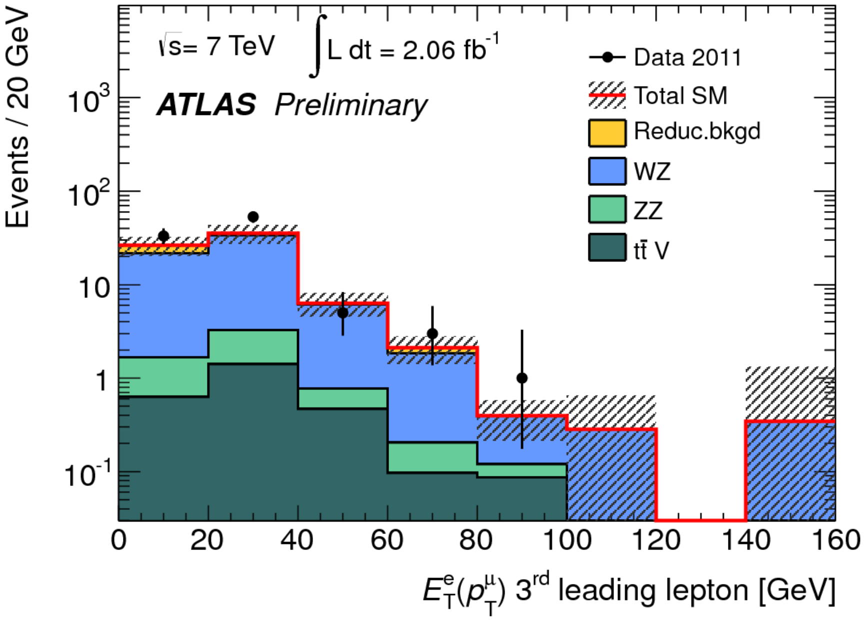

Figure A.7: *Distribution of the transverse momentum of the third leading lepton in signal region SR2 for the data and the SM prediction [45].*

Bibliography

[1] B. Povh, K. Rith, C. Scholz, and F. Zetsche. *Particles and Nuclei*. Springer-Verlag, 1995.

[2] Donald H. Perkins. *Introduction to High Energy Physics*. Addison Wesley, 1987.

[3] Michael E. Peskin and Daniel V. Schroeder. *An Introduction to Quantum Field Theory*. Addison-Wesley, 1987.

[4] K. Nakamura et al. (Particle Data Group) Particle Physics Booklet. *J. Phys. G*, 37(075021), 2010.

[5] ATLAS Collaboration. Combined search for the Standard Model Higgs boson using up to $4.9\,\mathrm{fb}^{-1}$ of pp collision data at $\sqrt{s} = 7\,\mathrm{TeV}$ with the ATLAS detector at the LHC. *Phys. Lett. B*, 710:49–66, 2012.

[6] CMS Collaboration. Combined results of searches for the standard model Higgs boson in pp collisions at $\sqrt{s} = 7\,\mathrm{TeV}$. *Phys. Lett. B*, 710:26–48, 2012.

[7] D. N. Spergel et al. First Year Wilkinson Microwave Anisotropy Probe (WMAP) Observations: Determination of Cosmological Parameters. *Astrophys. J. Suppl.*, 148(1):175–194, 2003.

[8] D. I. Kazakov. Beyond the Standard Model (In Search of Supersymmetry), hep-ph/0012288, 2000.

[9] S. P. Martin. A Supersymmetry Primer, hep-ph/9709356, 2011.

[10] Manuel Drees, Rohini M. Godbole, and Probir Roy. *Theory and Phenomenology of Sparticles*. World Scientific, 2005.

[11] W. Beenakker, R. Hopker, M. Spira, and P.M. Zerwas. Squark and gluino production at hadron colliders. *Nucl. Phys. B*, 492:51–103, 1997.

[12] A. Djouadi, J.L. Kneur, and G. Moultaka. SuSpect: a Fortran Code for the Supersymmetric and Higgs Particle Spectrum in the MSSM. *Comput. Phys. Commun.*, 176(426), 2007.

[13] D0 Collaboration. Search for associated production of charginos and neutralinos in the trilepton final state using $2.3\,\mathrm{fb}^{-1}$ of data. *Phys.Lett.B*, 680:34–43, 2009.

[14] LEP2 SUSY Working Group. `http://lepsusy.web.cern.ch/lepsusy/www/inos_moriond01/charginos_pub.html`, URL last visited: March 2012.

[15] ATLAS Collaboration. Search for squarks and gluinos using final states with jets and missing transverse momentum with the ATLAS detector in $\sqrt{s} = 7\,\mathrm{TeV}$ proton-proton collisions, ATLAS-CONF-2012-033, 2012.

[16] ATLAS Collaboration. Searches for supersymmetry with the ATLAS detector using final states with two leptons and missing transverse momentum in $\sqrt{s} = 7\,\mathrm{TeV}$ proton-proton collisions. *Phys. Lett. B*, 709:137–157, 2012.

[17] Lyndon Evans and Philip Bryant. LHC Machine. *JINST*, 3(S08001), 2008.

[18] CERN. `http://www.cern.ch`, URL last visited: March 2012.

[19] ATLAS Collaboration. ATLAS detector and physics performance : Technical Design Report, 1. ATLAS-TDR-014 ; CERN-LHCC-99-014, 1999.

[20] ATLAS Collaboration. The ATLAS Experiment at the CERN Large Hadron Collider. *JINST*, 3(S08003), 2008.

[21] Martin Lamprecht. Studien zu Effizienz und Akzeptanz des ATLAS-Myontriggers mit simulierten Messdaten. Diploma thesis, Ludwig-Maximilians-Universität München, 2007.

[22] M. Elsing and T. Schoerner-Sadenius. Configuration of the ATLAS Trigger System, physics/0306046, 2003.

[23] Worldwide LHC Computing Grid. `http://lcg.web.cern.ch/lcg/`, URL last visited: April 2012.

[24] The Gaudi Project. `http://proj-gaudi.web.cern.ch`, URL last visited: March 2012.

[25] S. Agostinelli et al. Geant4 - a simulation toolkit. *Nucl. Instrum. Meth. A*, 506(3):250–303, 2003.

[26] ATLAS Experiment Public Results. `https://twiki.cern.ch/twiki/bin/view/AtlasPublic/LuminosityPublicResults`, URL last visited: March 2012.

[27] G. Corcella et al. HERWIG 6.5: an event generator for Hadron Emission Reactions With Interfering Gluons (including supersymmetric processes). *JHEP*, 0101(010), 2001.

[28] S. Frixione and B.R. Webber. The MC@NLO 3.2 event generator, hep-ph/0601192, 2006.

[29] T. Sjöstrand, S. Mrenna, and P. Skands. PYTHIA 6.4 physics and manual. *JHEP*, 05(026), 2005.

[30] M. Bahr et al. Herwig++ Physics and Manual. *Eur. Phys. J. C*, 58(4):639–707, 2008.

[31] Johan Alwall, Michel Herquet, Fabio Maltoni, Olivier Mattelaer, and Tim Stelzer. MadGraph 5 : Going Beyond. *JHEP*, 1106(128), 2011.

[32] M.L. Mangano et al. ALPGEN, a generator for hard multiparton processes in hadronic collisions. *JHEP*, 0307(001), 2003.

[33] ATLAS Collaboration. Electron performance measurements with the ATLAS detector using the 2010 LHC proton-proton collision data. *Eur. Phys. J. C*, 72(3):1909, 2012.

[34] ATLAS Collaboration. Expected electron performance in the ATLAS experiment, ATL-PHYS-PUB-2011-006, 2011.

[35] ATLAS Collaboration. Expected Performance of the ATLAS Experiment - Detector, Trigger and Physics, arXiv:0901.0512v4, 2009.

[36] ATLAS Collaboration. Muon Momentum Resolution in First Pass Reconstruction of pp Collision Data Recorded by ATLAS in 2010, ATLAS-CONF-2011-046, 2011.

[37] M. Cacciari, G.P. Salam, and G. Soyez. The anti-kt jet clustering algorithm. *JHEP*, 04:063, 2008.

[38] ATLAS Collaboration. Properties of Jets and Inputs to Jet Reconstruction and Calibration with the ATLAS Detector Using Proton-Proton Collisions at $\sqrt{s} = 7\,\mathrm{TeV}$, ATLAS-CONF-2010-053, 2010.

[39] ATLAS Collaboration. Jet energy measurement with the ATLAS detector in proton-proton collisions at $\sqrt{s} = 7\,\mathrm{TeV}$. submitted to Eur. Phys. J. C, arXiv:1112.6426, 2011.

[40] ATLAS Collaboration. Commissioning of the ATLAS high-performance b-tagging algorithms in the 7 TeV collision data, ATLAS-CONF-2011-102, 2011.

[41] W. Lampl. Calorimeter Clustering Algorithms : Description and Performance, ATL-LARG-PUB-2008-002 ; ATL-COM-LARG-2008-003, 2008.

[42] ATLAS Collaboration. Performance of the Missing Transverse Energy Reconstruction and Calibration in Proton-Proton Collisions at a Center-of-Mass Energy of 7 TeV with the ATLAS Detector, ATLAS-CONF-2010-057, 2010.

[43] ATLAS Collaboration. Measurement of the top quark-pair production cross section with ATLAS in pp collisions at $\sqrt{s} = 7\,\text{TeV}$. *Eur. Phys. J. C*, 71(3):1577, 2011.

[44] J. J. Goodson. Private communication.

[45] ATLAS Collaboration. Search for supersymmetry in events with three leptons and missing transverse momentum in $\sqrt{s} = 7\,\text{TeV}$ pp collisions with the ATLAS detector, ATLAS-CONF-2012-023, 2012.

[46] ATLAS Collaboration. Luminosity Determination in pp Collisions at $\sqrt{s} = 7\,\text{TeV}$ using the ATLAS Detector in 2011, ATLAS-CONF-2011-116, 2011.

[47] A. L. Read. Presentation of search results: the CLs technique. *J. Phys. G*, 28, 2002.

List of Tables

List of Figures

Danksagungen

An erster Stelle möchte ich Prof. Dorothee Schaile danken, sowohl für die freundliche Aufnahme an ihrem Lehrstuhl als auch für die Betreuung meiner Arbeit. Auch für ihre große Geduld auf meinem nicht immer geraden Weg zum Ziel bin ich sehr dankbar.

Weiterhin gilt mein Dank Prof. Wolfgang Dünnweber für die Erstellung des Zweitgutachtens.

Prof. Raimund Ströhmer und Dr. Marie-Hélène Genest, die zu verschiedenen Zeitpunkten meiner Arbeit durch Anregungen und kritische Fragen wesentlich zu ihrem Gelingen beigetragen haben, möchte ich ganz besonders danken. Dr. Federica Legger danke ich für die zahlreichen Kommentare und Diskussionen während des Verfassens der Arbeit.

Für das Korrekturlesen meiner Arbeit danke ich Dr. Federica Legger, meinem Vater und David Magerl.

Außerdem möchte ich allen ehemaligen und aktiven Mitgliedern des Lehrstuhls, mit denen ich das Vergnügen zusammenzuarbeiten hatte, für die angenehme Arbeitsatmosphäre und die Hilfe in Fragen der Analyse oder des Computings danken. Besonders erwähnen möchte ich in diesem Zusammenhang meine Bürokollegen Sebastian Becker, Dr. Christian Kummer, Dr. Cédric Serfon und Josephine Wittkowski. Weiterhin danke ich der Lehrstuhlsekretärin Frau Hertha Franz für die unkomplizierte und schnelle Lösung sämtlicher Verwaltungsvorgänge.

Besonderer Dank für inspirierende Gespräche über QCD und verwandte Themen gilt Sebastian Becker, Dr. Christian Kummer, Dr. Markus Lichtnecker und Dr. Thomas Müller.

Schließlich danke ich meinen Eltern für ihre Unterstützung während meiner Promotion und die andauernden Fragen, wann ich endlich fertig werde.